

ILMENAU UNIVERSITY OF TECHNOLOGY
Faculty of Mathematics and Natural Sciences

FRAUNHOFER INSTITUTE FOR
DIGITAL MEDIA TECHNOLOGY IDMT

Measuring the Voice Coil Temperature of Electrodynamic Speakers with the HF Method according to Anazawa

BACHELOR THESIS

Course of Study: Technical Physics (B.Sc.)

Johannes Christof Martin Fried

Supervising University Lecturer: Prof. Dr. Stefan Krischok
Supervisor: Tobias Fritsch, M.Sc.

Submission Date: 31 December 2020

DOI: 10.22032/dbt.49008

URN: urn:nbn:de:gbv:ilm1-2021200105

Created as part of research at Fraunhofer IDMT

Abstract

Modern loudspeakers are expected to be small and light yet deliver high quality and loud sound. High levels can cause thermal failure of the speaker, necessitating the use of a thermal limiter. To minimize the thermal safety margin of the limiter and maximize sound level, the voice coil temperature needs to be measured during playback. Voice coil temperature can be measured through the well known relationship between temperature and direct current (DC) resistance. The high frequency (HF) method introduced by Gautama and Anazawa instead uses the relationship between temperature and impedance at an ultrasonic frequency. This enables lower noise and higher bandwidth compared to the DC method, which is verified through theory and experiment in this thesis.

Besides voice coil temperature, the HF impedance depends on excursion and surface temperature of the pole plates. These dependencies are measured on a sample microspeaker and modelled. Finally, DC and HF method are compared with different audio signals and shown to agree well. The requirements for voice coil temperature measurement can be fulfilled by both DC and HF method. The HF method may integrate better with active excursion offset stabilization but is more complex than the DC method. Additionally, the HF method allows measuring the surface temperature of the pole plates. Although pole plate surface temperature is affected by high frequency audio signals through induction heating, pole plate temperature could be used for better initialization of predictive thermal models. In the future, the combination of predictive thermal models and temperature measurement is expected to reduce the risk of thermal failure while increasing maximum sound pressure level.

Zusammenfassung

Von modernen Lautsprechern wird erwartet, dass sie klein und leicht sind und dennoch hohe Klangqualität und Pegel liefern. Hohe Pegel können zu einem thermischen Versagen des Lautsprechers führen, was die Verwendung eines thermischen Limiters erforderlich macht. Um den thermischen Sicherheitsspielraum des Limiters zu minimieren und den Schallpegel zu maximieren, muss die Schwingspulentemperatur während der Wiedergabe gemessen werden. Die Schwingspulentemperatur kann durch die Beziehung zwischen Temperatur und Gleichstromwiderstand gemessen werden (etablierte DC-Methode). Die von Gautama und Anazawa eingeführte Hochfrequenz-Methode (HF-Methode) verwendet stattdessen die Beziehung zwischen Temperatur und Impedanz bei einer Ultraschallfrequenz. Dies ermöglicht ein geringeres Rauschen und eine höhere Bandbreite im Vergleich zur DC-Methode, was in dieser Arbeit durch Theorie und Experiment verifiziert wird.

Neben der Schwingspulentemperatur hängt die HF-Impedanz von der Auslenkung und der Oberflächentemperatur der Polplatten ab. Diese Abhängigkeiten werden an einem Mikrolautsprecher gemessen und modelliert. Schließlich werden DC- und HF-Methode mit verschiedenen Audiosignalen verglichen und eine gute Übereinstimmung festgestellt. Die Anforderungen an die Messung der Schwingspulentemperatur können sowohl mit der DC- als auch mit der HF-Methode erfüllt werden. Die HF-Methode lässt sich möglicherweise besser mit einer aktiven Auslenkungs-Stabilisierung verbinden, ist jedoch komplexer als die DC-Methode. Zusätzlich ermöglicht die HF-Methode die Oberflächentemperatur der Polplatten zu messen. Obwohl die Oberflächentemperatur der Polplatten durch hochfrequente Audiosignale mittels Induktionserwärmung beeinflusst wird, könnte die Polplatten-Temperatur zur besseren Initialisierung prädiktiver Wärmemodelle verwendet werden. In Zukunft dürfte die Kombination von prädiktiven Wärmemodellen und Temperaturmessung das Risiko eines thermischen Versagens verringern und gleichzeitig den maximalen Schalldruckpegel erhöhen.

Contents

| | | |
|----------|---|-----------|
| 1 | Introduction | 6 |
| 1.1 | The Electrodynamical Moving Coil Speaker | 7 |
| 1.2 | Failure of Moving Coil Speakers | 7 |
| 1.3 | Why Measure Temperature? | 8 |
| 1.4 | Outline | 10 |
| 2 | Review of Voice Coil Temperature Measurement | 11 |
| 2.1 | Radiation-based | 11 |
| 2.2 | Sensor-based | 11 |
| 2.3 | Resistance-based | 12 |
| 2.3.1 | DC Method | 12 |
| 2.3.2 | LF Method | 12 |
| 2.3.3 | Audio-Band Method | 13 |
| 2.3.4 | HF Method | 13 |
| 3 | Theory | 15 |
| 3.1 | Requirements for Measuring Voice Coil Temperature | 15 |
| 3.1.1 | Temperature Range | 15 |
| 3.1.2 | Temperature Tolerance | 15 |
| 3.1.3 | Bandwidth | 16 |
| 3.1.4 | Economic, Practical and Other Considerations | 17 |
| 3.2 | Linearity of Resistance-Temperature Relationship | 18 |
| 3.3 | Impedance Measurement Error | 20 |
| 3.3.1 | Out-Of-Band Error | 20 |
| 3.3.2 | Smoothing Error | 23 |
| 3.3.3 | Application to Temperature Measurement Methods | 25 |
| 3.4 | Dependencies of the HF Impedance | 25 |
| 3.5 | Z_e -Model | 27 |
| 4 | Experiment 1: Climate Chamber | 32 |
| 4.1 | Test Signals | 32 |
| 4.1.1 | Impedance Monitoring Signal | 32 |
| 4.1.2 | Sweep Signal | 33 |
| 4.1.3 | Pulse Signal | 33 |
| 4.2 | Experimental Setup | 34 |
| 4.2.1 | Speaker Sample | 34 |
| 4.2.2 | Voltage- and Current-Monitoring | 34 |
| 4.2.3 | Measurement Interface | 37 |
| 4.2.4 | Amplifier | 38 |
| 4.2.5 | Speaker Setup in Climate Chamber | 38 |

| | | |
|----------|---|-----------|
| 4.2.6 | Measurement Procedure | 38 |
| 4.3 | Analysis Methodology | 41 |
| 4.3.1 | Click Removal in Sweeps | 41 |
| 4.3.2 | Sweep Analysis | 41 |
| 4.3.3 | Pulse Analysis | 41 |
| 4.3.4 | Z_e -Model Fit | 43 |
| 4.4 | Error Estimation | 44 |
| 4.4.1 | Temperature | 45 |
| 4.4.2 | Statistical Noise | 45 |
| 4.4.3 | Calibration Offset Error | 47 |
| 4.4.4 | Calibration Gain Error | 47 |
| 4.4.5 | Parasitics | 49 |
| 4.4.6 | Crosstalk | 50 |
| 4.4.7 | Further Ignored Errors | 50 |
| 4.4.8 | Error Summary | 51 |
| 4.5 | Results | 51 |
| 4.5.1 | Impedance Sweep | 51 |
| 4.5.2 | Temperature Calibrations | 53 |
| 4.5.3 | Z_e -Model Fit | 56 |
| 4.5.4 | Eddy Temperature Correction | 58 |
| 4.6 | Discussion | 60 |
| 5 | Experiment 2: Different Audio Signals | 61 |
| 5.1 | Test Signals | 61 |
| 5.2 | Experimental Setup and Procedure | 62 |
| 5.3 | Analysis Methodology | 63 |
| 5.4 | Results | 64 |
| 5.4.1 | Eddy Temperature | 64 |
| 5.4.2 | DC Temperature | 70 |
| 5.4.3 | HF Temperature | 70 |
| 5.4.4 | Comparison of HF and DC Temperature | 71 |
| 5.4.5 | Crosstalk Error | 73 |
| 5.4.6 | Influence of DC Offset | 74 |
| 5.5 | Discussion | 75 |
| 6 | Conclusion | 76 |
| 6.1 | Evaluation against Requirements | 76 |
| 6.2 | Summary | 79 |
| 6.3 | Outlook | 80 |
| | Bibliography | 81 |
| | List of Figures | 87 |
| | List of Tables | 89 |

1 Introduction

Humans love music [1]. That is why we want to capture it, save it and play it back anywhere and anytime we want. Small devices like smartphones are great for that, but the sound quality and volume of their speakers often leave a lot to be desired. On the other end of the size spectrum, concert sound systems are loud and sound great, but they are big and heavy. Since they need to be moved for every single concert, any reduction in size or weight is welcome to reduce the logistical effort. One of the goals of modern loudspeaker research is to improve this tradeoff between sound quality, sound volume and loudspeaker size.

To achieve higher output from a given speaker, it needs to be driven closer to its limits. Due to non-linear distortion, this reduces sound quality. Also, the speaker might fail due to mechanical or thermal overload. A promising approach to overcome these problems is to use digital signal processing to invert non-linear behavior and protect the driver [2]. Current day thermal protection often does not consider the actual speaker temperature. For example, RMS-limiters limit the root mean square (RMS) of the applied voltage instead of temperature. Because different signals can heat the speaker differently, this leaves a significant safety margin unused. This safety margin can be reduced if the speaker temperature is known during playback.

To measure the speaker temperature, little has been published on the high frequency HF method. In this thesis, the HF method will be shown to be a viable method for temperature measurement and compared to the established DC method.

1.1 The Electrodynamic Moving Coil Speaker

While there are lots of ways to convert electric into acoustic energy, this thesis only covers the most popular [3, 4, 5, p. 5] type: the electrodynamic moving coil speaker. It consists of a voice coil, wound from copper or aluminium wire, that is flexibly suspended in a magnetic field (see fig. 1.1). Currents through the voice coil result in a Lorentz force that moves the voice coil. Attached to the voice coil is a membrane that couples this movement to the air and produces sound. The magnetic circuit is closed with the pole plates, made from magnetically soft iron. The suspension, made from rubber, doped fabric or other flexible materials, keeps the voice coil centered in the small air gap between the magnetized iron pieces.

Lots of different variants of the moving coil principle exist. Please see the literature on the topic, such as [6].

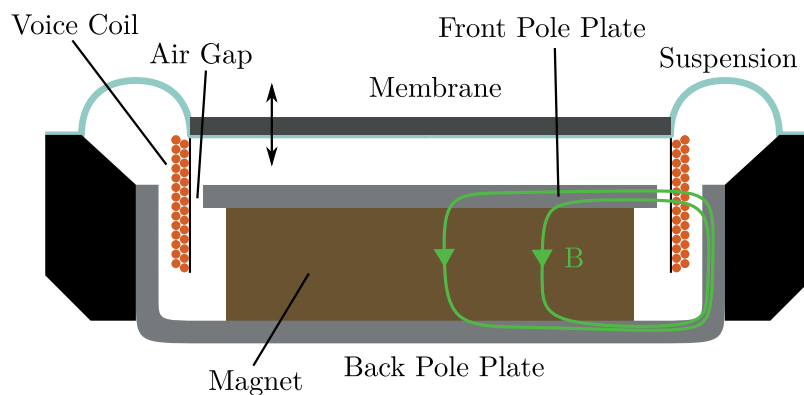


Figure 1.1: Schematic cross-section of a typical moving coil microspeaker (B-Field in green only for visualization, not physically accurate).

1.2 Failure of Moving Coil Speakers

The failure modes of moving coil speakers can be divided into thermal and mechanical failure [7]. Mechanical failure designates a family of failures related to integrity and alignment of the various parts. Alignment of the voice coil in the air gap is provided by the suspension. It must keep the voice coil centered and moving only along one axis. Otherwise the voice coil will rub on the pole plate, which creates rubbing noise, can compromise the isolation or tear the voice coil apart. The stress on all moving parts is especially big at high excursions, which can lead to material fatigue or ripping of suspension or membrane. Other mechanical failures include particles in the air gap, magnet parts going out of alignment or connecting wires losing contact [8].

Thermal failure is related to high temperature. Heat is created via ohmic losses in the voice coil and via induction heating in the iron pieces [9, p. 19]. Induction heating



Figure 1.2: Thermal failure of a speaker with 1-inch voice coil. Copper-colored voice coil on the left is mangled.

increases with frequency but music contains most power in the lower frequencies [10], so ohmic losses in the voice coil are usually dominant. Also, the voice coil will heat up faster than the iron parts due to lower thermal mass. High temperatures of the voice coil will soften the glue that holds the voice coil together, making it fall apart and rub on the pole plates. The isolation of the voice coil wire can also burn off, leading to shorting of the voice coil. Other glues and plastics in the construction may also be weakened by heat. The magnet can lose some of its magnetization due to heat every time it gets too hot, leading to less efficiency over the years [7].

An example of thermal failure can be seen in fig. 1.2. It shows a speaker with a 1-inch diameter voice coil that was destroyed by applying too much DC current. Failure was apparent from smoking. After letting the speaker cool down, the membrane could not be moved anymore. Prying the plastic membrane assembly from the metal magnet assembly reveals that the voice coil glue melted and the voice coil fell apart. The DC-resistance appeared normal afterwards, indicating that the isolation is still intact.

1.3 Why Measure Temperature?

During speaker development, measuring the voice coil temperature allows evaluating the effectiveness of cooling measures. Also, it can be used to generate training data

for thermal models. These thermal models try to predict the voice coil temperature from input power. Considerable research focused on such models [11–14], including non-linear compensations for voice coil movement [9].

During audio playback, knowing the temperature allows limiting the delivered power to avoid thermal failure. Also, the sound characteristics of the speaker depend on temperature, which can be compensated if the temperature is known. It has been suggested to use thermal models to predict the temperature during playback [2]. But these models can only predict how much the temperature rises and falls. To get absolute temperatures, they need to be initialized [15]. Initialization requires temperature measurement in the production environment. Once such a measurement is available, a sophisticated thermal model may not even be needed anymore because one can just use the measured temperature. Only to predict temperature into the future may a simple thermal model be needed.

For a numeric example, let's compare a model-based limiter with and without temperature initialization. The example speaker system is typically operated at ambient temperature T_{typ} , but also needs to work without failure at maximum ambient temperature T_{max} . Then, the model-based limiter needs to be adjusted such that at ambient temperature T_{max} the maximum voice coil temperature $T_{\text{VC, max}}$ is just barely reached. At T_{typ} , the same input power results in a voice coil temperature of only $T_{\text{VC, typ}} = T_{\text{VC, max}} - (T_{\text{max}} - T_{\text{typ}})$. Therefore, in the typical case the highest voice coil temperature above ambient is

$$\tau_{\text{VC, typ}} = T_{\text{VC, typ}} - T_{\text{typ}} = T_{\text{VC, max}} - T_{\text{max}} \quad (1.1)$$

The temperature above ambient τ can be assumed proportional to the applied power P [13, Eqn 1]. In the typical case we only apply $P_{\text{typ}} \propto \tau_{\text{VC, typ}}$ when we could theoretically apply $P_{\text{theo, typ}} \propto \tau_{\text{VC, theo, typ}} = T_{\text{VC, max}} - T_{\text{typ}}$. Therefore, we could apply ϵ more power where

$$\epsilon = \frac{P_{\text{theo, typ}}}{P_{\text{typ}}} = \frac{\tau_{\text{VC, theo, typ}}}{\tau_{\text{VC, typ}}} = \frac{T_{\text{VC, max}} - T_{\text{typ}}}{T_{\text{VC, max}} - T_{\text{max}}} \quad (1.2)$$

For example, let's assume $T_{\text{typ}} = 20^\circ\text{C}$, $T_{\text{max}} = 60^\circ\text{C}$ and $T_{\text{VC, max}} = 150^\circ\text{C}$ [16]. Then, by measuring the temperature during playback, the applied power in the typical case could be increased by $\epsilon = 1.4$ or 1.6 dB. Assuming the signal is similar to uniform excitation noise, this corresponds to a perceptual loudness increase of 9% [17, fig. 8.4]. These last percents can only be unlocked with temperature measurement in the production environment.

1.4 Outline

Different methods to measure the voice coil temperature will be categorized and reviewed in chapter 2. The HF method is introduced as the main topic of this thesis.

Chapter 3 will provide some theoretical foundations on performing and judging the HF method. Requirements for voice coil temperature measurements are established, possible errors for resistance-based methods are derived, influential dependencies of the HF impedance reviewed and a model for the HF impedance is presented.

A calibration for the HF method is performed in chapter 4. The expected dependencies of the HF impedance are measured and the model validated.

The calibration is applied to a real temperature measurement in chapter 5. The HF method is performed simultaneously with the established DC method and both are compared.

In chapter 6, differences between the established DC method and the new HF method are discussed. Suggestions for future research are given.

2 Review of Voice Coil Temperature Measurement

The literature review revealed three approaches to voice coil temperature measurement that will be discussed in the following.

2.1 Radiation-based

Matter emits infrared radiation whose spectrum changes with temperature. This allows a temperature measurement, known as infrared thermometry. While I could not find any scientific publications on its use in loudspeakers, there is a discontinued commercial product [18] from the car audio sector.

Radiation-based temperature measurement promises contact free measurement, so the acoustic impact is low. The time resolution can be high and the spatial resolution could be used to detect hotspots¹. On the other hand, complexity can be high as the emissivity of the surface needs to be considered and sight-line access to the voice coil is difficult, especially in small speakers.

Further research is needed to determine if or when radiation-based methods are useful for voice coil temperature measurement.

2.2 Sensor-based

A straightforward method is to glue or wind a temperature sensor into or onto the voice coil [11, 13, 19, 20].

This method is simple, cheap and well established. However, it requires changes to voice coil manufacturing or delicate modifications where the space for a temperature sensor may not be available in small speakers. Also, the temperature sensors need to work accurately in strong magnetic fields. Finally, there is no spatial resolution and the temperature sensor has itself a thermal mass that creates a lowpass-effect on the measured temperature.

¹It is reasonable to assume parts of the voice coil that are close to the pole plate cool faster than parts in the air, leading to spatially differing temperatures over the surface of the voice coil.

2.3 Resistance-based

An elegant method to measure the voice coil temperature is to use the metal in the voice coil as a resistance thermometer. The DC resistance R_{DC} of metals tends to increase relatively linear with temperature T . This allows a linear development around T_0 :

$$R_{DC}(T) = R_{DC,T_0}(1 + \alpha_{T_0}(T - T_0)) \quad (2.1)$$

where R_{DC,T_0} is the DC resistance at the development temperature T_0 and α_{T_0} is the temperature coefficient [21, p. 72].

Whereas the other temperature measurement methods measure only the surface temperature or the temperature of an attached sensor, resistance-based methods allow measuring the bulk temperature of the voice coil material itself without requiring any modifications of the speaker. Also, “smart amplifiers” with current and voltage monitoring are becoming more common [2, 22], enabling resistance measurement without additional hardware or cost. On the other hand, the resistance measurements need to be of high accuracy² and only the spatial average of the voice coil temperature can be measured.

The convenience and low cost of resistance-based temperature measurement made it the focus of this thesis. The DC resistance can be measured with different test signals, leading to the different methods described in the following.

2.3.1 DC Method

The conventional resistance-based temperature measurement method is the direct current (DC) method. It relies on measuring the resistance of the voice coil with a constant current or voltage.

2.3.2 LF Method

As alternative to the DC method, Klippel [9] has suggested using a low frequency (LF) tone, for example 1 Hz. He claims this is more convenient because the signal can be supplied with a normal AC-coupled amplifier and there is no DC-offset of the voice coil.

However the impedance at such low frequencies can still be affected by factors other than the DC resistance, for example suspension creep [23] that in itself is likely to show temperature dependence.

²Copper only changes its resistance by 0.4 % per Kelvin.

2.3.3 Audio-Band Method

Behler [24] has shown that the temperature can be measured with the audio signal as measurement signal. Current and voltage are monitored and the impedance calculated from both signals by deconvolution. The local impedance minimum above the resonance frequency is assumed to equal the DC resistance, yielding the temperature.

The advantage is that no additional test signal is needed. On the other hand, if there is no audio signal, the temperature cannot be measured. Also, the local impedance minimum is not only affected by DC resistance, but also by suspension stiffness, suspension damping, Eddy currents, etc. which themselves are temperature dependent. These factors should be closely examined in future research to get trustworthy results.

2.3.4 HF Method

The HF method measures the impedance of a high frequency (HF) tone above the audio spectrum and uses this impedance to derive the DC resistance. To my knowledge, it first appeared in an NXP patent by Gautama [25]. He asserts that the impact of the main resonance is negligible at HF and that the real part of the HF impedance closely approximates the DC resistance of the voice coil. He mentions three advantages of the HF method:

- Due to the inertia of the moving mass, the excursion at such high frequencies is nearly zero. In contrast to the DC and LF method, no excursion headroom is needed.
- There is lower amplifier noise at higher frequencies.
- HF tones have a shorter period and allow for finer temporal resolution, i.e. higher bandwidth.

The second appearance of the HF method is in a paper by Anazawa [26]. In contrast to Gautama he realized that at high frequencies the real part of the impedance is not identical to the DC resistance but includes resistance due to Eddy currents. He assumes that the Eddy current impedance is constant over time. He then continues with a temperature measurement survey on some microspeakers, comparing the HF and LF method. Unfortunately he uses the full range of audio frequencies for the LF method even though his impedance model does not account for motional impedance. This creates dramatic looking errors around the resonance frequency that are irrelevant for the result. The LF method at 40 Hz and his HF method are seen to agree to within around ± 2 K. He concludes the HF method is an accurate alternative to the LF- and DC method.

Anazawa published another paper [27], dealing with the effect of excursion on high frequency impedance. In his example, the HF method shows lower temperatures than

the LF method (40 Hz). This deviation rises with the amplitude of the signal used to heat the speaker which is why he claims it must be caused by excursion. However, the deviation is about the same size at excitation frequencies of 40 Hz and 5 kHz, but much more excursion must occur at 40 Hz than at 5 kHz. This makes it unlikely Anazawa's error is actually caused by excursion.

The compensation Anazawa gives for his error is based on the assumption that the relative changes in the real and imaginary part of the Eddy impedance are of the same size but opposite polarity. In the symbols of this thesis, Anazawa's assumption can be written as

$$\frac{\operatorname{Re}(Z_e) - \operatorname{Re}(Z_{e,0})}{\operatorname{Re}(Z_{e,0})} \approx -\frac{\operatorname{Im}(Z_e) - \operatorname{Im}(Z_{e,0})}{\operatorname{Im}(Z_{e,0})} \quad (2.2)$$

where the extra impedance without DC resistance Z_e is developed around $Z_{e,0}$. As source for this assumption Anazawa cites [28], though that paper never gives a singular answer to the dependence of impedance on excursion. Rather, measurements from different speakers with different behaviors are shown.

The promise of low noise, high bandwidth and no excursion overhead combined with little published research made the HF method an interesting research topic for this thesis.

3 Theory

To evaluate the HF method, this chapter will present some theoretical thoughts on requirements, the resistance-temperature relationship, inherent errors in all resistance-based temperature measurements and how parasitic variables affect the HF impedance.

3.1 Requirements for Measuring Voice Coil Temperature

To judge whether a voice coil temperature measurement method is suitable, requirements need to be established.

3.1.1 Temperature Range

The lower limit of the temperature range is given by the lower limit of the device operating range. This is $-20\text{ }^{\circ}\text{C}$ for typical industrial applications and $-55\text{ }^{\circ}\text{C}$ for military use [29].

The upper temperature limit is given by the thermal failure temperature of the voice coil. This depends on the used adhesives. Some adhesives can withstand up to $350\text{ }^{\circ}\text{C}$ for short periods of time [30].

3.1.2 Temperature Tolerance

The required temperature tolerance is assumed to be described by the symmetric measurement uncertainty $\pm\Delta T$. Then a thermal limiter needs to be adjusted such that it fully activates when the upper bound of the error band reaches the maximum temperature of the voice coil. In reality however, the voice coil temperature could still be $2\Delta T$ lower, leaving thermal headroom unused. Since input power P and temperature above ambient τ can be assumed to be proportionally related [13, Eqn 1], the power handling is reduced by

$$\zeta = \frac{P_{\max}}{P_{\max, \text{theo}}} = \frac{\tau_{\max} - 2\Delta T}{\tau_{\max}} = 1 - \frac{2\Delta T}{\tau_{\max}} \quad (3.1)$$

where P_{\max} is the maximum power that can be applied, $P_{\max, \text{theo}}$ is the maximum power that could be applied with an exactly known temperature and τ_{\max} is the maximum voice coil temperature above ambient. Solving for ΔT yields

$$\Delta T = \frac{\tau_{\max}}{2}(1 - \zeta) \quad (3.2)$$

The temperature measurement is accurate enough if a listener is unable to tell the difference to a perfect temperature measurement with slightly higher maximum power handling. The minimally audible change in level is roughly 0.5 dB [17, Fig. 7.7], corresponding to $\zeta \approx 0.89$. This means the temperature above ambient doesn't have to be known with a higher relative error than $\Delta T/\tau_{\max} \approx 5.5\%$. Assuming $\tau_{\max} = 150^\circ\text{C} - 20^\circ\text{C} = 130\text{K}$, this corresponds to $\Delta T \approx 7\text{K}$.

In practice, reductions in the output level greater than 0.5 dB could be considered acceptable, allowing an even less accurate temperature measurement to be sufficient. However, other error factors, such as different maximum temperatures for different batches of voice coils, must also be factored into the error band derived above, reducing the allowable error for the temperature measurement.

3.1.3 Bandwidth

The Bandwidth is a measure of the temporal resolution of the measurement. Thermal models show that the voice coil temperature is a lowpassed version of the power delivered to the speaker [13]. The upper cutoff frequency of this lowpass gives an estimate for the (single-sided) bandwidth required to accurately record the voice coil temperature.

For the sake of this estimation, a cutoff-amplitude of -40 dB or 1% was chosen. This seems sensible given the $\pm 5.5\%$ tolerance in subsection 3.1.2. As lowpass the model from Zucatti [12] was selected. Zucatti gives the model parameters for a “real loudspeaker of 130-mm diameter”. Chapman gives values for a 19mm-Tweeter¹ [13, second value table, page 3] and the frequency response [13, Eqn 1] of the Zucatti model. The frequency responses for both examples were normalized to 0 dB at 0 Hz and plotted (fig. 3.1). The -40 dB cutoff frequencies were determined with a non-linear solver. The cutoff frequency for Chapman's 19 mm tweeter was 4.0 Hz and for Zucatti's 130 mm speaker it was 2.6 Hz. As expected, the bigger speaker is thermally slower.

These findings can be extrapolated to differently sized voice coils by assuming the cutoff frequency is proportional to the ratio of heat dissipation to heat capacity. The heat capacity scales with mass $m \propto d^3$, where d is the voice coil diameter², and the ability to dissipate heat scales with area $A \propto d^2$. Therefore, the cutoff frequency can be assumed to roughly scale with $d^2/d^3 = 1/d$. Using the cutoff frequency of

¹It is most likely a dome tweeter where its size is given as the diameter of the voice coil.

²or another linear size parameter

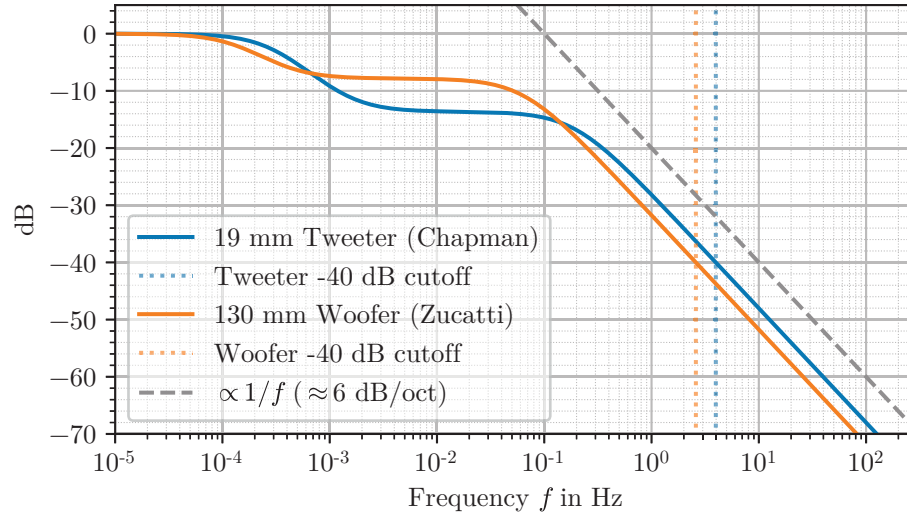


Figure 3.1: Magnitude response of the Zucatti thermal model vs. frequency. Two example speakers. Normalized at 0 Hz.

Chapman’s tweeter with a voice coil diameter of 19 mm, we can extrapolate to other voice coil diameters d with the following approximation formula for the (one-sided) bandwidth B :

$$B \approx \frac{76}{d} \text{ Hz mm} \quad (3.3)$$

This formula has not been validated and should be viewed as a very rough estimation. Assuming the full range of voice coil diameters goes from about 6 mm to 150 mm, the formula gives bandwidths from 13 Hz to 0.5 Hz. Applying a factor of 2 to account for different designs, we can conclude most speakers’ voice coil temperature signal will have a (one-sided) -40 dB bandwidth of 0.2 Hz to 26 Hz.

3.1.4 Economic, Practical and Other Considerations

Other requirements depend strongly on the specific application. The following list shows some desirable properties for voice coil temperature measurement:

- simple to understand and implement \rightarrow low development cost
- should work during audio playback without affecting sound quality or other negative effects
- simple calibration
 - low sample-sample-variation
 - stable over time or automatically correctable in production environment
- applicable to different types of speakers, for example differing in:

- size (small speakers may not offer much space for sensors or access to the voice coil)
- magnet type
- pole piece material
- demodulation rings
- voice coil material
- voice coil former material

3.2 Linearity of Resistance-Temperature Relationship

All resistance-based methods depend on the relationship between temperature and DC resistance. Authors are divided on whether this relationship can be modelled with a linear function [9] or a quadratic function [14] is required for speakers. Therefore, tabulated data on the resistivity of copper at different temperatures was used to check for sufficiency of a linear fit.

The resistivity of copper at different temperatures was extracted from a paper by Matula [31, Table 2, page 1116]. The chosen temperature range from 225 K to 700 K or approx. $-48\text{ }^{\circ}\text{C}$ to $427\text{ }^{\circ}\text{C}$ covers almost the complete range specified in section 3.1.1. The total resistivity from Matula is corrected for thermal expansion, but when measuring the resistance of a voice coil, no correction for expansion would be applied. Matula calls such uncorrected resistivity measurements *nominal*. The expansion correction was removed with [31, equation 11]:

$$\rho_{\text{nominal}}(T) = \rho(T) \left(1 + \frac{l(T) - l(293\text{K})}{l(293\text{K})} \right)^{-1} \quad (3.4)$$

where ρ is the resistivity and l is the length of a piece of copper. The expression $\frac{l(T) - l(293\text{K})}{l(293\text{K})}$ can be read as $\Delta L/L$ from [32, page 77] at specific temperatures, between which a second order spline was used to interpolate. Matula used the same source for thermal expansion correction. The relative size of the expansion correction was only $\pm 4 \cdot 10^{-3}$ over the chosen temperature range of $-48\text{ }^{\circ}\text{C}$ to $427\text{ }^{\circ}\text{C}$.

A linear function was fit through the resulting nominal total resistivities (fig. 3.2) using least square resistivity error. The resulting relative residuals were approximately $\pm 0.5\%$ and show clear curvature. Even though the uncertainty of the root data is 1% [31, page 1160], the clear curvature of the residuals indicates that a non-linear model for the resistance should be considered when measuring the temperature of high-temperature voice coils.

However, if we consider the operating range of the sample microspeaker in this thesis, which is -25 to $60\text{ }^{\circ}\text{C}$, and that it probably does not use a high temperature voice

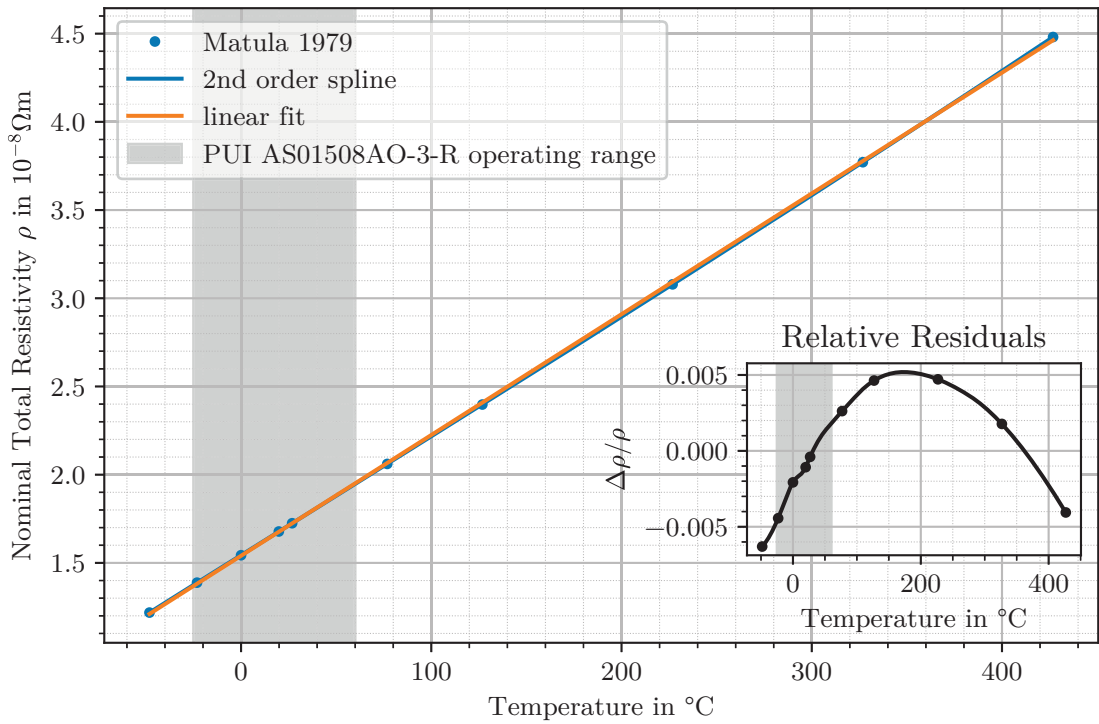


Figure 3.2: Linear fit of copper resistivity vs. temperature.

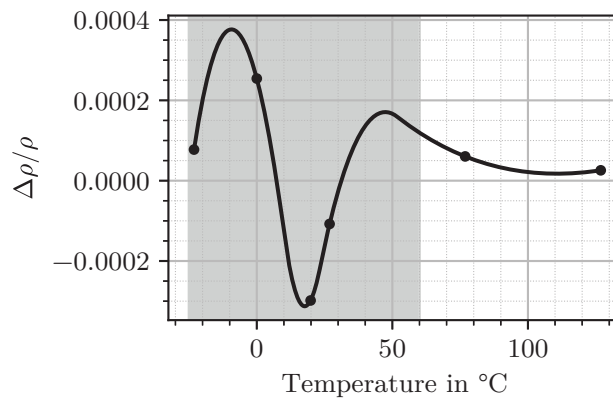


Figure 3.3: Relative residuals of linear fit of copper resistivity vs. a smaller temperature range.

coil, the relevant temperature range is much smaller. When the linear function is fit to the data points from approx. -23 to 127 °C, the relative residuals (fig. 3.3) are smaller than $\pm 4 \cdot 10^{-4}$ (25 times smaller than the uncertainty of the root data) and show no clear curvature. Therefore, a linear resistance-temperature relationship will be assumed for the rest of this thesis.

The linear fit over the small temperature range gives a reference value for the resistance thermal coefficient at 20 °C of $\alpha_{20} = 4.01 \cdot 10^{-3} \text{ K}^{-1}$. It must be noted however that this value applies only to annealed 99.999% pure or purer bulk copper.

According to Matthiessen's rule, impurities or crystal defects will scatter electrons in a non-temperature-dependent manner [31, chapter 2.1]. This means impurities, defects or deformations will lower the resistance thermal coefficient. For example in a study by Dellinger [21], α_{20} of copper wire varied from $3.71 \cdot 10^{-3} \text{ K}^{-1}$ to $3.95 \cdot 10^{-3} \text{ K}^{-1}$ (a range of ± 3.1 %). This means that the resistance thermal coefficient of the voice coil cannot be based on table values if accuracy better than a few percent is desired.

3.3 Impedance Measurement Error

The HF method promises lower noise and higher bandwidth than other resistance-based measurement methods. To support these claims, two kinds of error are derived that inherently limit noise and bandwidth performance due to time-frequency-uncertainty. Applying signals other than the measurement frequency f_0 , e.g. the audio signal, causes an out-of-band error, discussed in section 3.3.1. It cannot be reduced indefinitely due to the smoothing error, which will be discussed in section 3.3.2.

3.3.1 Out-Of-Band Error

Let's assume the impedance $Z(f)$ of a system is constant over time. This makes the system linear time invariant and therefore describable in the frequency domain. The voltage signal $u(t)$ and the current signal $i(t)$ over time t can be transformed to the frequency domain using a Fourier Transform, denoted by the operator

$$\mathcal{F} : y(t) \mapsto \int_{-\infty}^{+\infty} y(t) e^{-j2\pi ft} dt \quad (3.5)$$

where j is the imaginary unit and f is the frequency. The inverse Fourier Transform is denoted by

$$\mathcal{F}^{-1} : Y(f) \mapsto \int_{-\infty}^{+\infty} Y(f) e^{j2\pi ft} df \quad (3.6)$$

Transforming the current and voltage signals to the frequency domain yields

$$I(f) = \mathcal{F}i(t) \quad (3.7)$$

$$U(f) = \mathcal{F}u(t) = Z(f)I(f) \quad (3.8)$$

where the relationship between current and voltage in the frequency domain is given by the impedance $Z(f)$. Then, the signals need to be demodulated, i.e. shifted to the baseband such that the measurement frequency f_0 becomes zero frequency. This is easily implemented in the time domain by multiplying with an exponential function of the form $e^{-j2\pi f_0 t}$. Then, a lowpass with frequency response $L(f)$ is applied to reject all signals outside a passband around f_0 . This yields

$$\bar{I}(f) = L(f)I(f + f_0) \quad (3.9)$$

$$\bar{U}(f) = L(f)U(f + f_0) \quad (3.10)$$

Inserting eq. (3.8) and eq. (3.9) into eq. (3.10) results in

$$\bar{U}(f) = L(f)Z(f + f_0)I(f + f_0) = Z(f + f_0)\bar{I}(f) \quad (3.11)$$

Then the impedance at f_0 over time can be calculated by transforming back to the time domain and dividing:

$$\bar{z}(t) = \frac{\bar{u}(t)}{\bar{i}(t)} = \frac{\mathcal{F}^{-1}\bar{U}(f)}{\mathcal{F}^{-1}\bar{I}(f)} \quad (3.12)$$

Since we assumed $Z(f)$ to be constant over time, $\bar{z}(t)$ would ideally be constant at $Z(f_0)$. The residual error of the measurement therefore is

$$\mathcal{E}(t) = \bar{z}(t) - Z(f_0) = \frac{\bar{u}(t)}{\bar{i}(t)} - Z(f_0) = \frac{1}{\bar{i}(t)} [\bar{u}(t) - Z(f_0)\bar{i}(t)] \quad (3.13)$$

where eq. (3.12) was inserted. Assuming the residual error is square integrable, its power is given by integrating over the square of the absolute value:

$$P_{\mathcal{E}} = \int_{-\infty}^{+\infty} |\mathcal{E}(t)|^2 dt = \int_{-\infty}^{+\infty} \left| \frac{1}{\bar{i}(t)} [\bar{u}(t) - Z(f_0)\bar{i}(t)] \right|^2 dt \quad (3.14)$$

Even if the error signal would not be square integrable, the formula would reveal proportionalities, which is all we require at this point. The power can be calculated in

the frequency domain by utilizing Plancherel's Theorem, the linearity of the Fourier transform and the convolution theorem:

$$P_{\mathcal{E}} = \int_{-\infty}^{+\infty} \left| \mathcal{F} \frac{1}{\bar{i}(t)} * [\bar{U}(f) - Z(f_0)\bar{I}(f)] \right|^2 df \quad (3.15)$$

where the star $*$ denotes convolution. Inserting eq. (3.9) and eq. (3.11) and grouping terms yields

$$P_{\mathcal{E}} = \int_{-\infty}^{+\infty} \left| \mathcal{F} \frac{1}{\bar{i}(t)} * L(f)I(f + f_0) [Z(f + f_0) - Z(f_0)] \right|^2 df \quad (3.16)$$

The term $\mathcal{F} \frac{1}{\bar{i}(t)}$ is not representable in the frequency domain because inversion is a non-linear operation. If for example $\bar{i}(t)$ contains zero-crossings, poles could be introduced in the time domain causing severe changes in the frequency spectrum. To get a more interpretable result, we will assume the current consists of a sinusoid at f_0 with amplitude I_0 and a small additive noise $n(t)$ of amplitude A :

$$i(t) = I_0 e^{j2\pi f_0 t} + An(t) \quad (3.17)$$

$$I(f) = \mathcal{F}i(t) = I_0 \delta(f - f_0) + AN(f) \quad (3.18)$$

where $N(f) = \mathcal{F}n(t)$. Demodulating eq. (3.17) by multiplying with $e^{-j2\pi f_0 t}$ and applying a lowpass yields

$$\bar{i}(t) = I_0 + An(t)e^{-j2\pi f_0 t} * l(t) \quad (3.19)$$

where $l(t) = \mathcal{F}^{-1}L(f)$ is the impulse response of the lowpass that is assumed to satisfy $L(0) = 1$. Since the noise is small compared to the sinusoid, $I_0 \gg A$. This allows us to apply a binomial approximation for the inversion:

$$\frac{1}{\bar{i}(t)} = \frac{1}{I_0} \left[1 + \frac{A}{I_0} n(t)e^{-j2\pi f_0 t} * l(t) \right]^{-1} \quad (3.20)$$

$$\approx \frac{1}{I_0} \left[1 - \frac{A}{I_0} n(t)e^{-j2\pi f_0 t} * l(t) \right] \quad (3.21)$$

Transforming back to the frequency domain yields

$$\mathcal{F}\frac{1}{i(t)} = \frac{1}{I_0} \left[\delta(f) - \frac{A}{I_0} N(f + f_0) L(f) \right] \quad (3.22)$$

Inserting eq. (3.22) and eq. (3.18) into eq. (3.16) yields

$$P_{\mathcal{E}} = \int_{-\infty}^{+\infty} \left| \frac{1}{I_0} \left[\delta(f) - \frac{A}{I_0} N(f + f_0) L(f) \right] * L(f) \left[I_0 \delta(f) + AN(f + f_0) \right] \left[Z(f + f_0) - Z(f_0) \right] \right|^2 df \quad (3.23)$$

Multiplying out on the right side of the convolution, one notices that

$$I_0 \delta(f) \left[Z(f + f_0) - Z(f_0) \right] = 0 \quad (3.24)$$

because the excitation directly at f_0 does not cause any error. Since $I_0 \gg A \implies \frac{A}{I_0} N(f + f_0) L(f) \approx 0$ on the left side of the convolution. The remaining convolution with a delta function is performed and the result re-arranged to give

$$P_{\mathcal{E}} \approx \left| \frac{A}{I_0} \right|^2 \int_{-\infty}^{+\infty} \left| L(f) N(f + f_0) \left[Z(f + f_0) - Z(f_0) \right] \right|^2 df \quad (3.25)$$

To interpret this formula for the out-of-band error, note that the integral becomes zero if one of the factors becomes zero. If the term $Z(f + f_0) - Z(f_0)$ is zero, i.e. the impedance is constant with frequency, the error goes to zero. At zero frequency, the term $Z(f + f_0) - Z(f_0)$ is zero and the other terms do not matter. If the term $L(f)$ or $N(f + f_0)$ are zero, the error is zero as well. The smaller the overlapping area of the lowpass, the shifted noise and the shifted change in impedance, the smaller the error. The term $\frac{A}{I_0}$ means that to reduce the out-of-band error, the amplitude of the noise should be small compared to the sinusoid.

The error formula can be applied to the special case of the DC method by setting $f_0 = 0$.

3.3.2 Smoothing Error

The out-of-band error in the previous section is easily reduced by applying a low-pass with zero bandwidth. Of course, this would not allow the impedance to change over time, thus making it useless for measuring the voice coil temperature. This error from the lowpass restricting changes of the impedance shall be called smoothing error.

To estimate the smoothing error, we will assume the current is purely sinusoidal:

$$i(t) = I_0 e^{j2\pi f_0 t} \quad (3.26)$$

Then the current is shifted to the baseband:

$$\hat{i}(t) = I_0 e^{j2\pi f_0 t} e^{-j2\pi f_0 t} = I_0 \quad (3.27)$$

and the relationship between current and voltage in the baseband is given by the impedance at f_0 over time $z_0(t)$:

$$\hat{u}(t) = z_0(t) \hat{i}(t) = I_0 z_0(t) \quad (3.28)$$

Then, application of the lowpass $l(t)$ required to reject out-of-band signals results in

$$\bar{i}(t) = l(t) * \hat{i}(t) = I_0 \quad (3.29)$$

$$\bar{u}(t) = l(t) * \hat{u}(t) = I_0 l(t) * z_0(t) \quad (3.30)$$

because $L(0) = 1$. Then the impedance over time is given by

$$\bar{z}(t) = \frac{\bar{u}(t)}{\bar{i}(t)} = l(t) * z_0(t) \quad (3.31)$$

In the ideal case, $\bar{z}(t) = z_0(t)$. Therefore, the smoothing error signal is given by

$$\mathcal{S}(t) = \bar{z}(t) - z_0(t) = l(t) * z_0(t) - z_0(t) \quad (3.32)$$

The power of the error signal is given by integrating over its absolute square:

$$P_S = \int_{-\infty}^{\infty} |l(t) * z_0(t) - z_0(t)|^2 dt \quad (3.33)$$

Applying Plancherel's theorem, the power can be calculated in the frequency domain as

$$P_S = \int_{-\infty}^{\infty} |L(f)Z_0(f) - Z_0(f)|^2 df \quad (3.34)$$

$$= \int_{-\infty}^{\infty} |[L(f) - 1] Z_0(f)|^2 df \quad (3.35)$$

where $Z_0(f) = \mathcal{F}z_0(t)$. Since $L(0) = 1$, no smoothing error occurs when the impedance $z_0(t)$ is constant. Generally, every change in the impedance that is filtered out by the lowpass results in smoothing error.

If instead of a constant current a constant voltage is assumed, the above formula can also be derived for the smoothing error of the admittance over time $\bar{z}^{-1}(t)$. However, with a constant voltage the smoothing error for the impedance $\bar{z}(t) = 1/(\bar{z}^{-1}(t))$ is not linear and may exceed eq. (3.35).

3.3.3 Application to Temperature Measurement Methods

The lowpass must be chosen to achieve a compromise between out-of-band error and smoothing error. If the bandwidth of the lowpass is increased, the smoothing error goes down but the out-of-band error goes up. Since the DC resistance is linearly related to temperature, the temperature bandwidth derived in section 3.1.3 may be a good starting point for the lowpass bandwidth.

Of the presented methods, the LF method will have the biggest problems in achieving a good compromise between out-of-band error and smoothing error. Since all real signals will show symmetry in the frequency domain around zero frequency, a real sinusoidal at f_0 will have one component at f_0 and one component at $-f_0$ in the frequency domain. After shifting to the baseband, the other peak will cause out-of-band error. This causes the biggest problems for the LF method because the distance between both peaks is small. For the DC method, the peak at negative and positive frequencies coincide, removing this issue. For the HF method, the difference between the peaks is so large that any lowpass can easily filter out the other peak.

When using the DC or LF method, a highpass should be applied to the audio signal to reduce out-of-band error.

The HF method provides theoretically improved out-of-band error over the DC method in three ways: First, amplifier noise is lower at HF than around DC. Second, the audio signal can be expected to rapidly drop above 20 kHz and the frequency for the HF method can easily be spaced far above the audio signal. Third, the change in impedance per Hz is usually smaller at higher than lower frequencies due to the strong effect of the main resonance at low frequencies. Therefore, the claims of Gautama [25] that the HF method has higher bandwidth and lower noise than other methods seem warranted.

3.4 Dependencies of the HF Impedance

While it is clear that the HF impedance must depend on voice coil temperature to be able to measure it, other unwanted dependencies must also be considered and calibrated out for an accurate measurement. To analyze these dependencies, we will follow Anazawa [26] and without loss of generality divide the impedance Z into the DC resistance R_{DC} in series to the “extra” impedance Z_e :

$$Z(f, \dots) = R_{DC}(\dots) + Z_e(f, \dots) \quad (3.36)$$

For a specific, non-faulty speaker sample, R_{DC} mainly depends on the voice coil temperature T_{VC} . Other influences on resistance include strain and light illumination [33]. Since the voice coil is freely suspended, the only reason for strain would be thermal. The only publication found on photoconductivity in bulk copper did not reveal any dependence of resistivity on light illumination [34].

The “extra” impedance Z_e includes effects of alternating currents and can therefore depend on many more factors than the DC resistance. For example, the movement of the voice coil causes an impedance peak at the resonance frequency of moving mass and suspension stiffness. At HF far above the resonance frequency, the influence of this peak is low. Therefore we will follow Anazawa in assuming a blocked impedance model, i.e. one that does not consider voice coil movement, is sufficient for the HF method. Please see section 4.5.3 for a discussion on the influence of the main resonance peak.

The Skin effect increases the resistance of the voice coil wire towards high frequencies because currents only flow on the outside of the conductor. The resistance increase can be calculated for a straight, round metal wire in vacuum with [35, A1-17]

$$\frac{R_{\text{skin}}}{R_{DC}} = \frac{kr}{2} \frac{M_0(kr)}{M_1(kr)} \sin\left(\theta_1(kr) - \theta_0(kr) - \frac{\pi}{4}\right) \quad (3.37)$$

where $k = \sqrt{\omega\sigma\mu}$ with circular frequency $\omega = 2\pi f$, conductivity $\sigma = 1/\rho$ and permeability $\mu = \mu_0\mu_r$ and the wire radius r . Further, $M_\nu(kr) = \left|J_\nu\left(j^{\frac{3}{2}}kr\right)\right|$ and $\theta_\nu(kr) = \arg\left(J_\nu\left(j^{\frac{3}{2}}kr\right)\right)$ where J_ν are Bessel functions of the first kind and order ν .

Voice coil wire can be expected to have a diameter of 0.03 mm to 1.3 mm [36, 37] and be made of copper, resulting in $\rho \approx 1.7 \cdot 10^{-8} \Omega\text{m}$ at 20 °C or $\rho \approx 2.5 \cdot 10^{-8} \Omega\text{m}$ at 140 °C (fig. 3.2). Also $\mu_r \approx 1$ because copper is not ferromagnetic. Under these conditions, the relative resistance increase, given by eq. (3.37) minus one, is plotted in fig. 3.4. Due to the fact that the voice coil has many wires next to each other, the Skin effect will be even stronger, but not by more than a factor of 2 [35, fig. 4]. In this thesis a microspeaker is used that likely uses wire on the thinner side. Assuming $d = 0.1$ mm the Skin effect at 34 kHz can be expected to increase the resistance on the order of 10^{-5} , which is negligible compared to other effects. Since the influence of the Skin effect is negligible, the temperature dependence of the Skin effect does not matter either. However, if a thick voice coil wire is used, the Skin effect may be higher than 10^{-2} and its temperature dependence will become important for temperature measurement. Because Z_e would then depend on the voice coil temperature, the calibration as shown in this thesis would not be applicable.

The last, and dominant effect on Z_e is the induced magnetic field, which creates an inductive behavior. It will also induce Eddy currents in all close conductive materials, creating some lossy behavior and rise in the real part of the impedance. The Eddy currents depend on material properties like permeability and resistivity which both are temperature dependent [38]. Therefore, Z_e will depend on the temperature of the Eddy current-carrying parts, mostly the pole plates. This temperature will be called Eddy temperature T_e .

The speaker impedance is known to depend on the position of the voice coil in the air gap [28] and so Z_e will also depend on the excursion x . No other additional

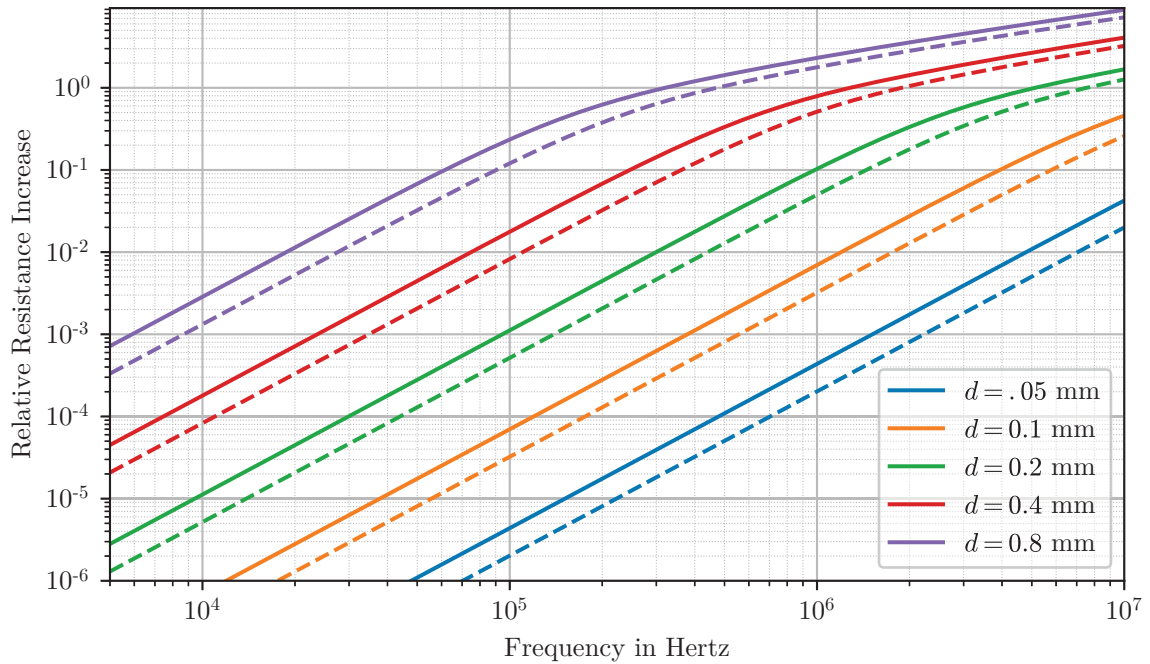


Figure 3.4: Relative resistance increase due to Skin effect vs. frequency, shown for different copper wire diameters used in speakers. Solid lines at 20 °C, dashed lines at 140 °C.

effects on high-frequency blocked impedance are cited in typical sources [39], indicating these effects are sufficient to understand the problem at hand. In summary, the following impedance model and its dependencies will be considered in this thesis:

$$Z_{HF} = R_{DC}(T_{VC}) + Z_e(f, x, T_e, \dots) \quad (3.38)$$

Further factors may influence Z_e , for example imagine bringing the speaker close to a metal surface. Then the stray magnetic field will induce Eddy currents in the metal and the Eddy current impedance will change. These factors are mostly ignored in this thesis, but represented by “...” in eq. (3.38).

3.5 Z_e -Model

To understand in detail how the previously derived dependencies affect Z_e , a numerical model for the influence of the magnetic field on the extra impedance Z_e is derived. While this can be modelled to great accuracy with Finite Element Methods [28, 40], to reach an intuitive understanding of the effects, a simple lumped model is more suited. In a lumped model, the geometry of the system is neglected and replaced

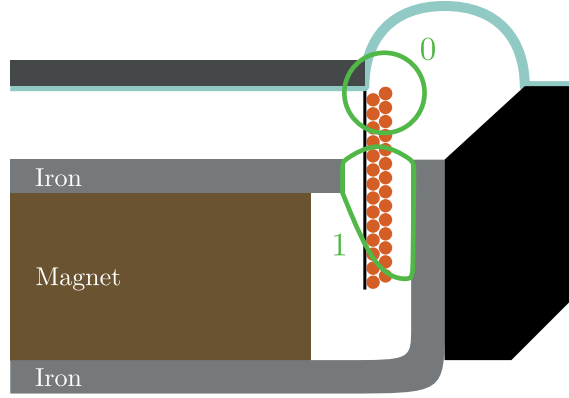


Figure 3.5: Visualization of B-Field induced by current through the voice coil on outer part (0) and inner part (1) in green. Not physically accurate.

by few scalar values, hence “lumping” all parts together. The most well known example of lumped models is the electrical circuit diagram. The same approach can be extended to the magnetic domain, for example with the Gyrator-Capacitor Approach [41].

Applying this approach to the moving coil speaker, we first divide the voice coil of N turns into an outer part with $G_0 = N\Gamma$ turns and an inner part with $G_1 = N(\Gamma - 1)$ turns where $\Gamma \in [0, 1]$. This will later allow us to model the effect of excursion. In the Gyrator-Capacitor Approach each of the two coils is now represented with a gyrator that transforms electrical voltage u into the time derivative of magnetic flux $\dot{\Phi}$ and electrical current i into the magnetic effort F . If the gyrator has N_g windings, the transformation is

$$u = N_g \dot{\Phi} \quad (3.39)$$

$$i = \frac{1}{N_g} F \quad (3.40)$$

In fig. 3.6, a gyrator is symbolized by the two half circles, similar to a transformer. The magnetic fields induced by the two coils are visualized in fig. 3.5. The magnetic field of the outer coil is assumed to only flow through air. The ability of the air to inhibit changes of the magnetic flux is represented by the permeance $\mathcal{P}_{air,0}$ on the right side of Gyrator G_0 . The permeance has the circuit symbol and impedance behavior of a capacitor, hence the name of the Gyrator-Capacitor Approach. The inner part of the voice coil induces a magnetic field that travels through iron and air, hence $\mathcal{P}_{air,1}$ and the magnetic impedance $Z_{iron,1}$ are placed in series on the right side of Gyrator G_1 .

Some magnetic field will also flow through the magnet and may induce some Eddy currents, depending on the magnet material. Since the permeability of magnets is small [39], the influence of Eddy currents in the magnet will be ignored in this thesis.

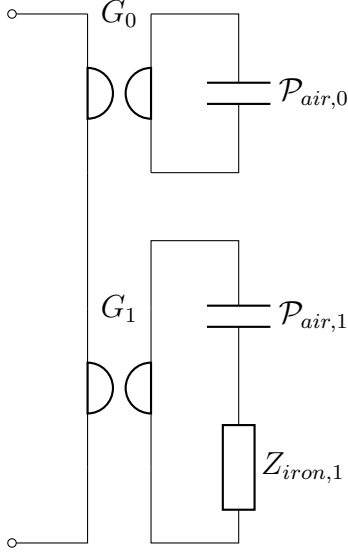


Figure 3.6: Equivalent circuit for Z_e in the Gyrator-Capacitor Approach.

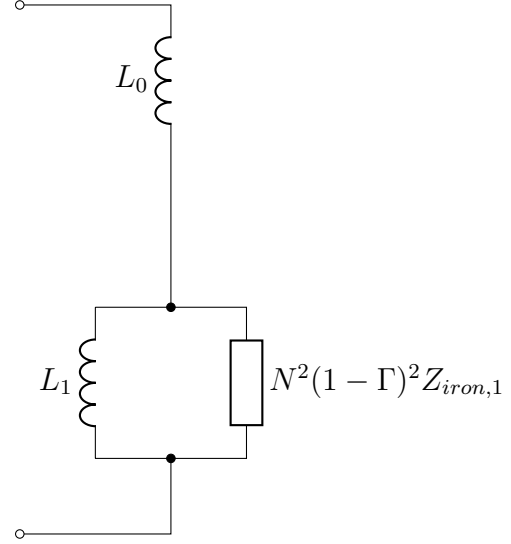


Figure 3.7: Equivalent circuit for Z_e , transformed from the magnetic to the electrical domain.

The magnetic circuits can be transformed to the electrical domain by transforming the impedance: When an impedance Z is connected to one side of a gyrator with N_g turns, an impedance of N_g^2/Z is seen on the other side. Therefore the electrical impedance of Gyrator 0 is

$$Z_0 = \frac{N^2\Gamma^2}{Z_{air,0}} = \frac{N^2\Gamma^2}{\frac{1}{j\omega\mathcal{P}_{air,0}}} = j\omega N^2\Gamma^2\mathcal{P}_{air,0} \quad (3.41)$$

which can be simplified to a simple inductance $L_0 = N^2\Gamma^2\mathcal{P}_{air,0}$. Similarly, the electrical impedance of Gyrator 1 is given by

$$Z_1 = N^2(1 - \Gamma)^2 \frac{1}{\frac{1}{j\omega\mathcal{P}_{air,1}} + \frac{1}{Z_{iron,1}}} \quad (3.42)$$

which is equivalent to the parallel connection of an inductance $L_{air,1} = N^2(1 - \Gamma)^2\mathcal{P}_{air,1}$ and the iron impedance $N^2(1 - \Gamma)^2 Z_{iron,1}$.

The behavior of the iron impedance was derived by Vanderkooy [42]. He solved the Maxwell equations for a simplified case of an infinitely long voice coil around an infinitely long cylindrical iron core. The resulting iron impedance is a simple inductance for very low frequencies and a semi-inductance for very high frequencies. The impedance of a semi-inductance K is given by

$$Z_K = K\sqrt{j\omega} \quad (3.43)$$

While a normal inductance has a phase angle of 90° and rises linearly with frequency, the semi-inductance has a phase angle of 45° and is proportional to the square root of the frequency.

The transition between the low and high frequency case occurs when the Skin depth $\delta = d/\sqrt{8}$ where d is the diameter of the iron core. The Skin depth δ is the depth at which the current has dropped to $1/e$ where e is the Euler number and can be estimated as [42]

$$\delta = \sqrt{\frac{2\rho}{\omega\mu}} \quad (3.44)$$

As a numeric example, iron at room temperature has a resistivity around $10^{-7} \Omega \text{ m}$ [43] and a relative permeability that varies wildly depending on composition, treatment, magnetic field and frequency, but for a rough estimation we will assume it to be in the range of $1 \cdot 10^2$ to $2 \cdot 10^5$ [44]. At 20 kHz this yields a Skin depth of $1.1 \cdot 10^{-3} \text{ m}$ to $2.5 \cdot 10^{-6} \text{ m}$. Since the pole plates in microspeakers could easily be less than a millimeter thick, and the magnetic saturation from the magnet will reduce the permeability of the iron parts compared to the table values, the high frequency approximation is not sufficient. However, Vanderkooy's result can be approximated with a semi-inductance in parallel to an inductance. While the transition of this approximation is more gradual than the actual behavior, both high and low frequency case is modelled accurately and the model is much simpler than the original. Replacing $N^2\Gamma^2 Z_{iron,1}$ with the parallel connection of a semi-inductance $K_1 = (1 - \Gamma)^2 \tilde{k}_1$ and an inductance $L_{iron,1} = (1 - \Gamma)^2 l_{iron,1}$, the parallel inductances can be combined to get $L_1 = 1/(1/L_{air,1} + 1/L_{iron,1}) = (1 - \Gamma)^2 l_1$. This yields the final impedance model shown in fig. 3.7 with the impedance

$$Z_e = Z_{L0} + (Z_{L1} \parallel Z_{K1}) \quad (3.45)$$

$$= j\omega L_0 + \frac{1}{\frac{1}{j\omega L_1} + \frac{1}{\sqrt{j\omega K_1}}} \quad (3.46)$$

The model is nearly identical to the one presented by Thorborg [40], but his model was not parametrized against temperature and excursion. The presented model can describe varying excursions with the excursion parameter Γ that divides the windings between the inner and outer part. To achieve the dependence on Eddy temperature, we will assume \tilde{k}_1 changes linearly around 0°C with the temperature coefficient α :

$$\tilde{k}_1 = k_1(1 + \alpha\vartheta) \quad (3.47)$$

where ϑ is the Eddy temperature in $^\circ \text{C}$. The influence of the temperature on $L_{iron,1}$ is neglected. The low permeability of air makes $L_{air,1}$ low and the high $L_{iron,1}$ in parallel is assumed to have a small influence.

Substituting $l_0 = N^2 \mathcal{P}_{air,0}$ yields the final equations describing the lumped elements:

$$L_0 = l_0 \Gamma^2 \quad (3.48)$$

$$L_1 = l_1 (1 - \Gamma)^2 \quad (3.49)$$

$$K_1 = k_1 (1 - \Gamma)^2 (1 + \alpha \vartheta) \quad (3.50)$$

Please note magnetic hysteresis losses were neglected in this model, but they may be included with a resistor parallel to L_1 and K_1 [45]. Thorborg [39] includes such a resistor but claims it models the losses in demodulation rings.

The presented model will be fit to measured data in the next chapter.

4 Experiment 1: Climate Chamber

The goal of the first experiment is to measure the dependencies of the HF impedance outlined in section 3.4 on a specific speaker sample. This will allow the verification of the assumptions made by previous authors and the assumptions made in deriving the Z_e model. Further, it will yield the calibration required to later demonstrate the HF method.

For this purpose, the DC resistance is measured at different voice coil temperatures and Z_e at different frequencies, excursions and Eddy temperatures. Different temperatures were achieved with the climate chamber of the Fraunhofer IDMT. No distinction can be made between voice coil and Eddy temperature but they affect R_{DC} and Z_e independently and thus do not need to be separated. Excursion was varied with an applied low-frequency pulse.

4.1 Test Signals

To measure the different impedances, different test signals were played through the speaker while voltage and current were recorded. In all measurements, the frequency for the HF method was chosen as 34 kHz, right in the middle between the upper audio frequency of 20 kHz and the Nyquist frequency of 48 kHz, giving maximum bandwidth up and down. In the following, the HF impedance always means the impedance at 34 kHz.

4.1.1 Impedance Monitoring Signal

When changing the temperature in the climate chamber, the speaker will take some time until all parts have converged on the new temperature. To assess when a new measurement could be taken, the DC resistance and HF impedance were monitored with a signal that was automatically played and analyzed every 10 s to 40 s. Once both resistance and impedance had converged, a new measurement could be taken.

The test signal was an HF tone. After 3 s a DC offset was added that continued for another 3 s. The DC offset was faded in and out over 0.2 s and the HF tone over 1 ms to avoid exciting the main resonance around 500 Hz. Both signals had a power of less than 1 mW and created no measurable change in voice coil temperature according to earlier measurements. Backing up this assumption, no continuous rise

in DC resistance was ever visible when just running the impedance monitoring signal regularly.

4.1.2 Sweep Signal

To measure the frequency dependence of the impedance, a logarithmic sweep [46] from 1 Hz to 48 kHz with a length of 15 s was used. The sweep was windowed at the beginning with a half-Hann window equal to the time till the first local maximum and a 1 ms half-Hann window at the end. The windowing prevents broadband excitation that could otherwise arise from quick changes in the signal. The amplitude was chosen such that no measurable heating would be expected. The power dissipated in the speaker was less than 2.4 mW and the impedance monitor never showed any significant differences in DC resistance before and after the sweep, supporting the assumption that the sweep did not significantly heat the speaker.

4.1.3 Pulse Signal

To measure the HF impedance at different excursions, the Pulse-signal was devised (fig. 4.1). It consists of a 3 s period with only an HF signal to measure the HF impedance at resting position. Then, the DC signal is turned on, giving another 3 s to measure the DC resistance and the HF impedance at a slightly different voice coil position. Then, a 1 s pulse is played to introduce a large excursion in both directions while monitoring the HF impedance. The pulse is the result of one 0.8 s period of a triangular waveform, convolved with a 0.2 s Hann window. The amplitude of this

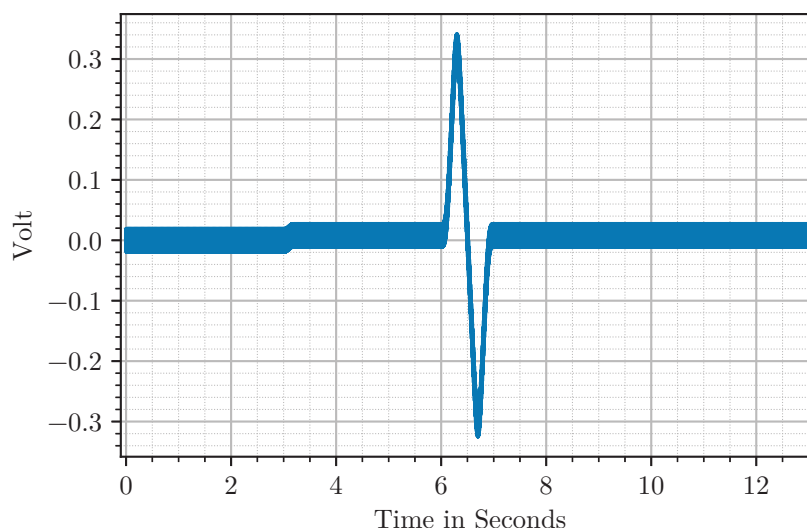


Figure 4.1: The pulse signal. Y-axis shows output voltage of the Datatranslation interface, the voltage applied to shunt and speaker is amplified by a factor of 10. The solid colored area is the result of the 34 kHz sine wave.

pulse was chosen as big as possible while not exceeding the maximum continuous power rating of the speaker during the extremes of the pulse. The length of the pulse at 1 s was a compromise between getting enough data and being fast enough not to significantly heat the pole plates and magnet. The pulse is then followed by 6 s of the DC and HF signal continuing, allowing to monitor the cooldown process after the pulse has heated the voice coil. This is followed by a fade-out, where DC- and HF-signal are faded out.

4.2 Experimental Setup

4.2.1 Speaker Sample

Only a single speaker sample is used in this thesis to keep the workload manageable. Thus the results are not directly transferrable to other speakers. The sample speaker was a PUI Audio AS01508AO-3-R (see fig. 4.2). Its dimensions are $(15 \times 11 \times 3)$ mm. It would typically be used in smartphones, tablets or other compact consumer electronics. It features an NdFeB magnet and a rated impedance¹ of 8Ω . The temperature operating range is -25°C to 60°C [48], which was fully utilized during this experiment. Its internal layout is likely similar to the typical microspeaker shown in fig. 1.1. Such a small speaker was chosen to minimize the time needed for warming and cooling the speaker.

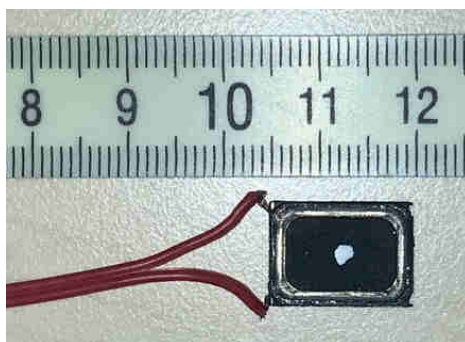


Figure 4.2: PUI speaker used in this thesis. The white paint dot improves reflectivity for laser vibrometry.

4.2.2 Voltage- and Current-Monitoring

To measure impedance, voltage and current signals need to be recorded.

The voltage over the speaker was taken with pick-off clamps from the stripped part of the wire, right next to the solder pads of the speaker. The current was supplied to the

¹The rated impedance is not necessarily related to the impedance of the speaker. According to DIN EN 60268-5 [47], the impedance should not fall more than 20% below the rated impedance, but this is not universally adhered to.

speaker through two soldered on wires, roughly 10 cm in length. The stripped ends of the wires were contacted with clamps. Separating the voltage sensing and current carrying contacts is known as 4-terminal sensing and mostly eliminates the effect of wire and contact resistance [49, page 50]. Wire and contact resistances can be in the magnitude of $10^{-1} \Omega$ (section 4.4.5) and contact resistances are different every time the contact is re-established. This makes 4-terminal sensing crucial when measuring impedances of just a few Ohms as in this thesis.

Monitoring the current was achieved by placing a shunt resistor in series with the speaker. The current $I(f)$ in the frequency domain is then given as

$$I(f) = \frac{U_s(f)}{Z_s(f)} \quad (4.1)$$

where $U_s(f)$ is the voltage over the shunt resistor and $Z_s(f)$ is the impedance of the shunt resistor. The transformation from and to the frequency domain can be achieved with the Fast Fourier Transform (FFT). The voltage over the shunt resistors was always measured with clamps as close to the resistor casings as possible. The current was provided by another set of clamps, slightly further from the casing. This again applies the 4-terminal sensing technique.

The shunt resistor was formed by two 1Ω resistors solidly soldered together in series. Each resistor was rated for 50 W and placed on aluminium heatsinks. It must be ensured the shunt resistors do not heat up and change their impedance during measurement, as noted by [19]. The possible heat-up can be estimated: If the speaker in series dissipates the maximum rated power of 0.7 W at a DC resistance of 7Ω , the current is 316 mA. Therefore, 0.1 W are dissipated in each of the 1Ω shunt resistors. This is 0.2 % of the rated power of the resistors. Assuming they would heat up 100 K at their rated power, their temperature during testing would only increase by 0.2 K.

The magnitude of resistance changes with temperature was further estimated with a Keysight E4990A Impedance Analyzer. The shunt impedances at 34 kHz and 20 Hz were monitored while the resistors were heated with a hot air gun. The resistors were hot enough so touching them was not comfortable anymore. At 20 Hz, no change beyond noise could be observed by heating the shunt resistors. At 34 kHz, the change in the real part was around 0.02 % ($0.4 \text{ m}\Omega$) and 0.7 % ($0.2 \text{ m}\Omega$) in the imaginary part. This indicates that the resistor is made from a material with very low temperature coefficient. Taking into account the very small estimated heat-up of the resistors, heating of the resistors can be excluded as source of substantial measurement error.

The frequency-dependent impedance of the shunt resistor was also measured with the Keysight E4990A Impedance Analyzer. While it would be capable of great precision, no official accessories for measuring the shunt resistors' impedance with 4-terminal sensing were available. Therefore, 4 standard BNC cables with clamps were used for

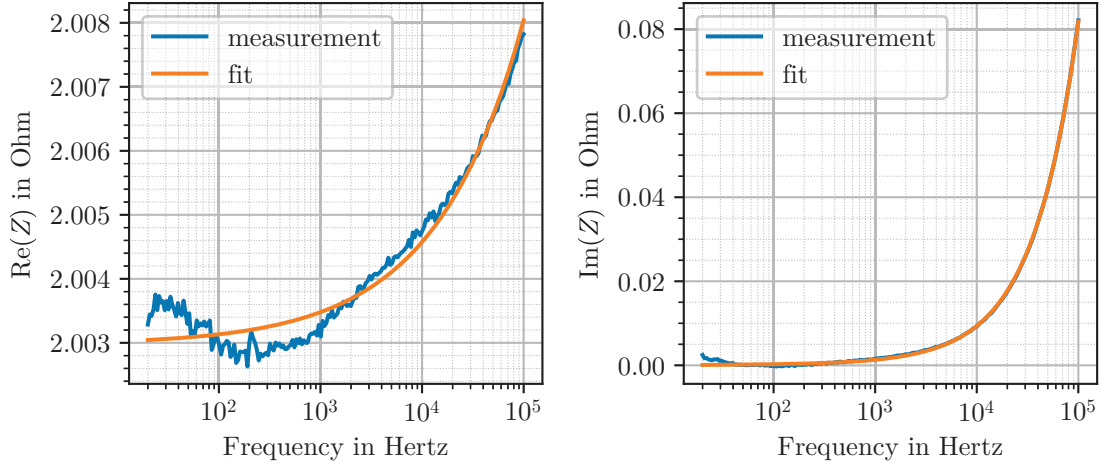


Figure 4.3: Measured impedance of shunt resistor, divided into real part on the left and imaginary part on the right. The fitted shunt model is shown in orange.

which no accuracy is guaranteed by the manufacturer. An open/short calibration was performed.

The impedance of the shunt resistor Z_s was fit with a model consisting of a resistance in series to an inductance and semi-inductance. Since the package used for this fit did not support complex fits, the real and imaginary part were fitted separately as

$$\operatorname{Re}(Z_s) = R_s + \sqrt{\pi f} K_{s,\text{real}} \quad (4.2)$$

$$\operatorname{Im}(Z_s) = 2\pi f L_s + \sqrt{\pi f} K_{s,\text{imag}} \quad (4.3)$$

The results of these fits were $R_s = (2.00297 \pm 0.00005) \Omega$, $K_{s,\text{real}} = (9.0 \pm 0.3) \cdot 10^{-6} \Omega \sqrt{\text{s}}$, $L_s = (1.21 \pm 0.01) \cdot 10^{-7} \text{ H}$ and $K_{s,\text{imag}} = (9.8 \pm 0.9) \cdot 10^{-6} \Omega \sqrt{\text{s}}$ (deviations at 95 % confidence). As can be seen in fig. 4.3, some anomalies at low frequencies were not well fit by the model. These anomalies could not be explained and may just be measurement error of the non-properly calibrated impedance analyzer.

All following analyses were carried out with the shunt resistor model instead of the measurement data directly to not introduce noise from the shunt resistor measurement into the main measurements. Any error in the impedance of the shunt resistor will proportionally affect the current measurement. But as long as the same resistor is used every time, false shunt resistor impedances will be calibrated out in the climate chamber measurement and will not affect the temperature measurement.

4.2.3 Measurement Interface

The voltages were recorded with a Datatranslation DT9837C [50]. This measurement interface provides 1 BNC output and 4 BNC inputs via a USB connection. The data was recorded on a Linux laptop via the provided Python API [51]. The sample rate for inputs and output was set to 96 kHz. Since no differential inputs were available, the voltages over the shunt and speaker were measured with 2 channels each and subtracted in the digital domain.

The Datatranslation interface has functions to calibrate gain and offset of the converters. However due to the high sensitivity of DC-measurements to the offset and drift of the calibration over time, it was decided to record calibration information before and after every measurement and correct the measurements in post-processing with the corresponding calibration data. The calibration procedure was automated with a script. It consisted of first shorting all 4 channels to ground and recording the value x_o for all channels averaged over 1 second. Then, a calibration voltage of approximately 9.375 V was connected to all channels, its exact voltage u_g read from a Fluke 8846A precision multimeter [52] and entered into the script. Next, the gain calibration voltage x_g was recorded and averaged for 1 s. The gain g is calculated as $g = (x_g - x_o)/u_g$ and the offset o as $o = x_o/g$. The gain and offset for each of the four channels are then written to a text file. The calibrated value x can later be calculated from the measured value x_{measured} as $x = x_{\text{measured}}/g - o$.

To ensure functioning equipment, the loopback frequency response of the Datatranslation interface was measured. The output was connected to the four inputs with BNC splitters. Then, a logarithmic sweep [46] from 1 Hz to 48 kHz with a length of 6 s and an amplitude of 2.8 V was played from the output while the inputs were recording. The output has a maximum amplitude of ± 3 V and the inputs of ± 10 V. The input signals and the output signal were deconvolved against each other to yield the loopback frequency response of each channel. The coherence deviated less than 10^{-3} from 1 with the exception of a few hundred Hz below Nyquist, indicating a very low noise measurement. The loopback frequency response showed a gentle lowpass-behavior with a -3 dB point of 42.5 kHz, getting significantly steeper above 44 kHz. At 34 kHz, the loopback response is about 2 dB down. The loopback response of all 4 channels agreed very well to within 0.003 dB. The loopback phase showed some slight rise around 35 kHz of about 10° . A measurement with an oscilloscope confirmed that the frequency response errors were not attributable to either just input or just output. While the linear frequency response errors of the inputs are a potential error source, we are mainly interested in the impedance, meaning the differences and ratios between the 4 channels. Since all 4 channels agree very well, the error from the lowpass behavior can be expected to be small. Also, the same interface is used for all measurements and errors will be calibrated out in the climate chamber and not influence the temperature measurement.

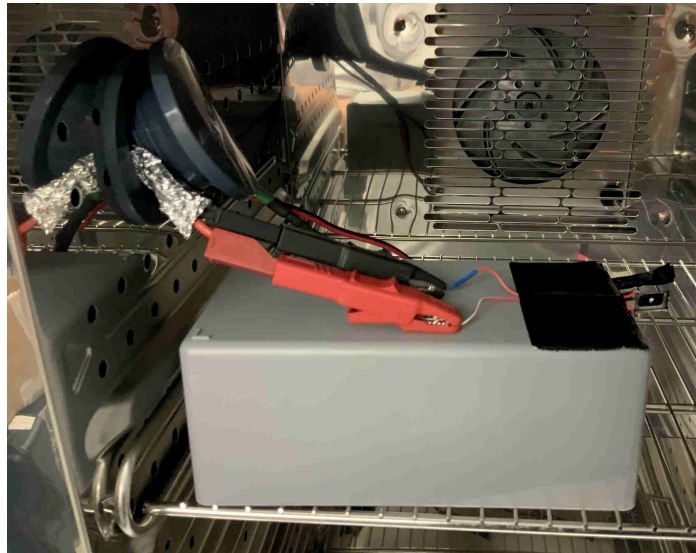


Figure 4.4: Speaker setup in the climate chamber. Left: Cable channel. Middle: Clamps used to carry current through the speaker. Right: Speaker taped to the gray box for stability.

4.2.4 Amplifier

The output of the Datatranslation interface was connected to a PiezoDrive PX200 amplifier with a voltage gain of 10 whose outputs were connected to shunt resistor and speaker. The amplifier's typical application is driving piezo speakers, but besides an unusual output impedance it works fine for moving coil speakers. Most importantly, it was the only amplifier at the institute capable of DC output.

4.2.5 Speaker Setup in Climate Chamber

The speaker was set up in the climate chamber, a Binder MKF 56 [53], hanging on its wires with the membrane roughly pointing upward (fig. 4.4). The amplifier, Datatranslation interface, shunt resistor and multimeter for calibration and monitoring were placed outside (fig. 4.5). To reduce crosstalk between the current-carrying wires and the voltage-sensing wires in the cable channel, the current carrying wires were twisted and wrapped in a grounded piece of aluminium foil.

4.2.6 Measurement Procedure

The speaker was cooled from room temperature to -25°C over night. On the next day, the Datatranslation was calibrated twice (both calibrations were very similar) and the calibration was loaded into the impedance monitoring script. A DC offset on the output of the Datatranslation interface was added in such a way that the multimeter showed a DC offset at the amplifier output of less than 1 mV.

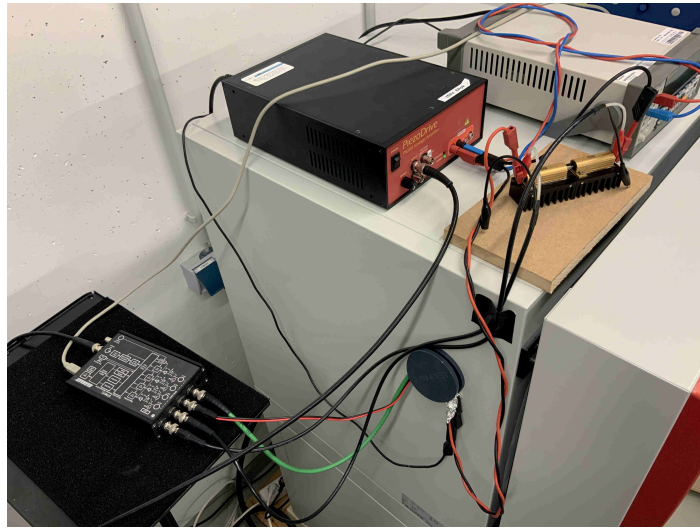


Figure 4.5: Measurement setup on top of the climate chamber. Left to right: Data-translation interface, amplifier (red faceplate), cable channel (dark gray), shunt resistors on wooden plate, multimeter (beige). Current-carrying wires are twisted where possible and shielded with grounded aluminium foil in the cable channel.

Then, the pulse and sweep signals were played and recorded. After the pulse signal, the monitored impedances showed a slight uptick. To avoid unnecessary heating the sweep was performed before the pulse test from $-15\text{ }^{\circ}\text{C}$ onwards (fig. 4.6). In quite a few cases, the used sweep measurement was still taken after the pulse measurement. This is because lots of sweep measurements showed clicking artifacts, likely due to some software or firmware issue. The sweep was then repeated up to two times, often after the pulse test and a short waiting period. Some measurements showed clicking in all three runs. It was attempted to fix these measurements in post-processing.

After performing the sweep and pulse measurements, the climate chamber temperature was increased by 5 K and the impedance and resistance were closely monitored. When they seemingly converged (after around 8 min to 14 min), the next sweep and pulse measurements were performed, the temperature increased, and so on.

After reaching the maximum operating temperature of the speaker ($60\text{ }^{\circ}\text{C}$) and the last measurements were taken, another two calibrations of the Datatranslation interface were performed which again agreed well with each other. Then, the chamber was opened and the speaker allowed to cool down.

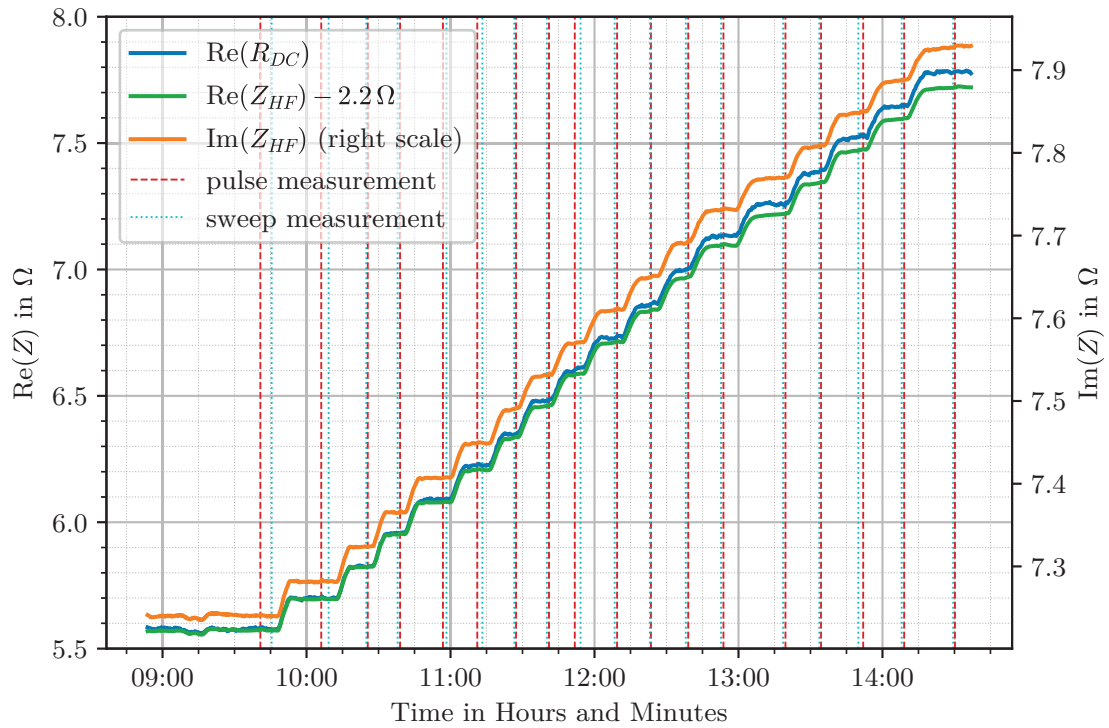


Figure 4.6: Monitored impedance during experiment 1. DC resistance and offset real part of HF impedance on left scale, imaginary part of HF impedance on the right scale. Vertical lines show the times of measurements that ended up being used, thrown away measurements are not shown.

4.3 Analysis Methodology

The analysis of the measurements was performed in the scientific programming language Julia [54] with some standard packages (including but not limited to [55–61]) in Jupyter Lab [62]. The analysis steps are described in the following.

4.3.1 Click Removal in Sweeps

Even with repeating the measurements multiple times, the sweeps at 0 °C, 20 °C and 25 °C contained clicks where seemingly some signal was skipped in the recording. The clicks occurred at the same time in all 4 channels. At the affected temperatures, the measurement with the lowest amplitude click was selected. For the 20 °C case, the click at 850 Hz was removed by delaying the signal by 14.5 samples and then cutting to the undelayed version around the click. For 0 °C and 25 °C, the signals were split at the click and the space between filled with the excitation sweep, matched in phase and amplitude before and after the click. At 25 °C, 576 samples were inserted around 5.3 kHz. At 0 °C, 650 samples were inserted around 32 Hz.

4.3.2 Sweep Analysis

The voltages from the corresponding temperature were read in and the mean calibration from all 4 calibration runs applied. The voltage over the speaker and shunt resistor were calculated as the difference of the signals at both respective terminals. The voltage over the shunt was transformed to the frequency domain with an FFT and divided by the impedance of the shunt resistor model at the respective frequencies to obtain the spectrum of the current signal. The current signal was then obtained by inverse FFT. The impedance was obtained from voltage and current signal by deconvolution [61]. The coherence from the lowest non-DC frequency to 47 kHz was checked to be above 0.99. Finally, the impedance curves were downsampled to a reasonable resolution using a Hann window as lowpass.

4.3.3 Pulse Analysis

As in the sweep analysis, the voltage over the speaker and current signal were calculated. Then the signals were divided into 70 ms blocks with Hann windows and a stride of one third the window length. For each block, the DC resistance was calculated as the ratio of the mean voltage and the mean current. The HF impedance for each block was calculated by multiplying voltage and current in the time domain with a complex 34 kHz tone of the form $e^{-j2\pi f_{\text{HF}}t}$, then taking the mean and dividing voltage by current. This represents a demodulation operation.

The signals were synchronized to the pulse by finding the peak of the voltage over the speaker. After starting the test signal, the system was given 1 s to settle before

averaging the HF impedance over 1.9 s. After turning the DC offset on, the system was given 1 s to settle and the DC resistance then averaged over 1.7 s.

The evolution of the HF impedance during the pulse is shown in the left plot of fig. 4.7. The back-and-forth movement of the voice coil does not lead to the same impedance in either direction because the pulse heats up the voice coil and increases the DC resistance during the test signal. To calculate Z_e , the DC resistance needs to be known at all times during the pulse. But since the pulse is a non-DC signal at low frequency, the out-of-band error does not allow an accurate DC resistance measurement during the pulse. This out-of-band error can be seen in the blue curve in fig. 4.8. Therefore, the DC resistance during the pulse was calculated with the discretized version of a simple thermal RC-model as in [11]. The power was calculated by multiplying the voltage and current signals. This power was then integrated at 96 kHz, but at each timestep a certain percentage of the energy was allowed to dissipate. The resulting energy signal is scaled and the starting DC resistance before the pulse added to yield the simulated DC resistance. This model is fit to the 500 ms after the pulse has ended (marked red in fig. 4.8). Since the RC-model cannot properly fit the long-term cooldown of the magnet and iron parts, a crossover point between model and measurement is chosen such as to minimize the jump between both.

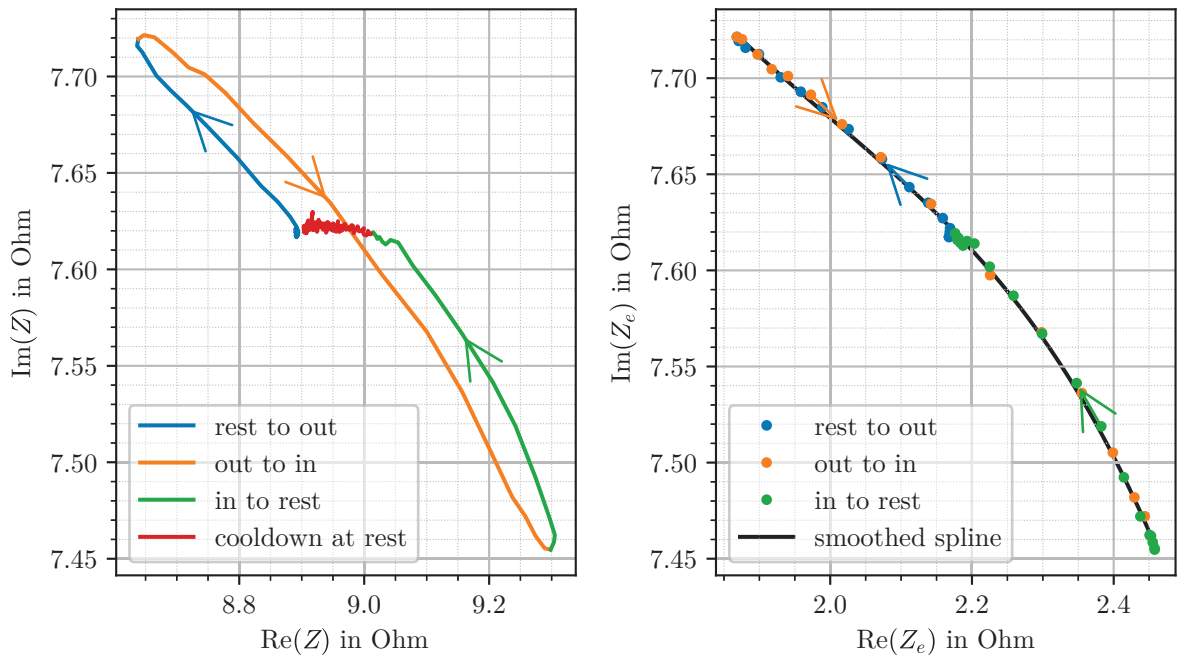


Figure 4.7: Left: Evolution of HF impedance Z on the complex plane while playing the pulse test signal. Right: The same for Z_e with subtracted DC resistance. In comparison to the left plot, Z_e is the same whether going out- or inward. This indicates the DC resistance calculated with a thermal RC model based on the power delivered to the speaker is accurate. Both measurements performed at 20 °C in the climate chamber.

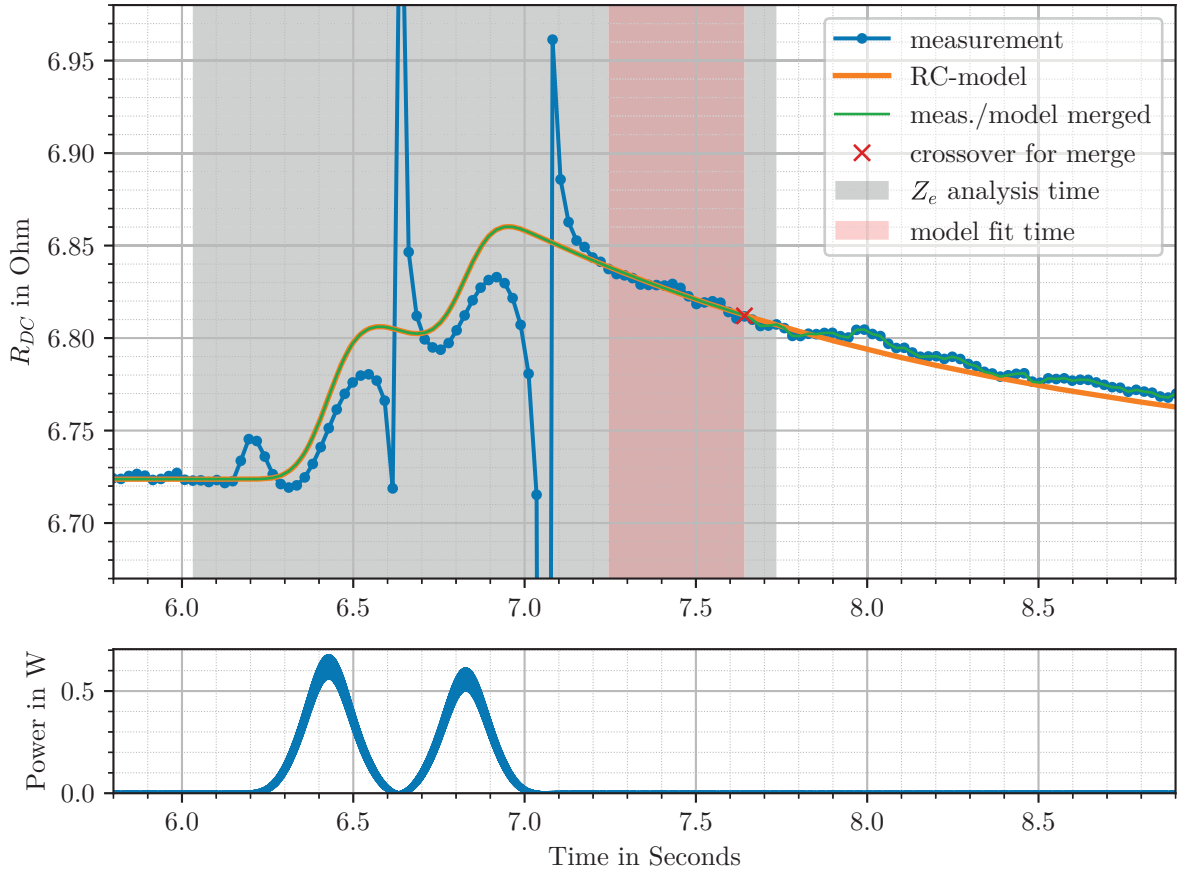


Figure 4.8: Top: DC resistance during pulse-measurement at 20 °C. The measurement shows significant out-of-band error while the model is smooth as expected. Bottom: Power over the speaker in the same measurement. Used to feed an RC model which yields the orange curve in the top plot.

Once R_{DC} during the pulse is estimated, Z_e can be calculated by subtracting R_{DC} from Z . The resulting excursion behavior shows good agreement between the back-and-forth movements of the voice coil (right subplot in fig. 4.7), validating the RC-model and confirming the pulse did not significantly heat the pole plates, only the voice coil. A smoothed spline was fit to Z_e -points, sampled at regular intervals on the real axis and used for later analyses to describe the shape of Z_e at different excursions.

4.3.4 Z_e -Model Fit

The sweep analysis, combined with the DC resistance at each temperature, yields data describing $Z_e(f, T)$ whereas the pulse analysis yields data describing $Z_e(x, T)$, allowing us to fit the Z_e model from section 3.5.

The model needs the excursion parameter $\Gamma \in [0, 1]$ to be defined for every data point.

To assign one to every data point, it was assumed the values from the smoothed spline describing Z_e at different excursions, sampled at regular intervals on the real axis, would have an excursion parameter linearly spaced between $\Gamma_{\min}(\vartheta)$ and $\Gamma_{\max}(\vartheta)$. It was further assumed these bounds would change linearly with temperature²:

$$\Gamma_{\max}(\vartheta) = \Gamma_0 + \Gamma_{\max,0}(1 + \beta\vartheta) \quad (4.4)$$

$$\Gamma_{\min}(\vartheta) = \Gamma_0 + \Gamma_{\min,0}(1 + \gamma\vartheta) \quad (4.5)$$

where ϑ is the temperature in °C. Unfortunately, this approach resulted in a curvature of the excursion dependence that did not match the measured data. Therefore, an empirical exponent η was introduced that replaced the quadratic relationship from section 3.5:

$$L_0 = l_0\Gamma^\eta \quad (4.6)$$

$$L_1 = l_1(1 - \Gamma)^\eta \quad (4.7)$$

$$K_1 = k_1(1 - \Gamma)^\eta(1 + \alpha\vartheta) \quad (4.8)$$

Overall, the fit parameters of l_0, l_1, k_1, α were extended with the fit parameters $\Gamma_0, \Gamma_{\max,0}, \beta, \Gamma_{\min,0}, \gamma, \eta$ yielding a total of 10 fit parameters.

The optimization goal for the fit was the sum of the squared distance on the complex plane between the fitted and measured values. The optimization proved quite sensitive to starting conditions, so a robust evolutionary optimizer³ was used. To make computation times bearable, the frequency data was downsampled to 56 points from 20 kHz to 45 kHz, a range chosen because the influence of the main resonance and the Nyquist frequency are small. The excursion data was downsampled to 13 points at each temperature. The resulting optimization took around 13s to reach the final optimum, though some more time was allotted to the algorithm to ensure convergence. Due to the usage of a derivative-free global optimizer, an estimation of the fit parameter uncertainty is not easily available and time did not permit a sensitivity analysis or similar. Therefore, the parameters will be given without statistical uncertainty.

4.4 Error Estimation

In this section the various error sources in the measurements are discussed and their influence on the final values estimated.

²Please note this way to determine Γ is highly flawed. For higher accuracy, it should be determined how close the measured curve is to the model curve for $\Gamma \in [0, 1]$ without actually assigning values of Γ to the measurement data points.

³adaptive_de_rand_1_bin_radiuslimited from [60]

4.4.1 Temperature

The Climate Chamber, a Binder MKF 56, is specified to deliver temporal temperature deviations of less than ± 0.5 K and spatial temperature deviations of less than ± 1.5 K around the target temperature [53].

A further temperature error is the convergence error: After increasing the target temperature, the waiting period may have been too short for the impedances to reach thermal equilibrium. This can be seen sometimes in the impedance monitoring over time (fig. 4.6). From looking at that plot, I put this error at about ± 0.5 K.

The overall temperature error is ± 2.5 K.

4.4.2 Statistical Noise

The statistical noise includes factors such as the Datatranslation interface noise, amplifier noise, the Johnson-Nyquist Noise of the involved resistors, induced noise from the environment or acoustical noise that is picked up by the speaker acting as a microphone. To estimate the statistical noise, the impedance monitor recording (fig. 4.6) was used. It was smoothed with a 3-sample moving average and subtracted from the unsmoothed values to obtain the residual noise. This residual noise only showed slight correlation with the original signal, for example being slightly lower when the unsmoothed values show positive curvature (fig. 4.9). These correlations were at least a factor 2 below the noise. Therefore their influence is small and they would tend to widen the error band, leading to over-estimation of the error. Normal Distributions were fit to the residual noise of the DC resistance and the real and imaginary part of the HF impedance respectively (fig. 4.10). The standard deviations of these fits are reported in table 4.1. The double standard deviations $2\sigma_s$ correspond to a confidence interval of 95 %.

Table 4.1: Standard deviations σ_s of normal distributions fit to the residual noise of the monitored impedances.

| | $2\sigma_s$ in $\text{m}\Omega$ |
|----------------|---------------------------------|
| R_{DC} | 3.6 |
| $\text{Re}(Z)$ | 1.3 |
| $\text{Im}(Z)$ | 0.7 |

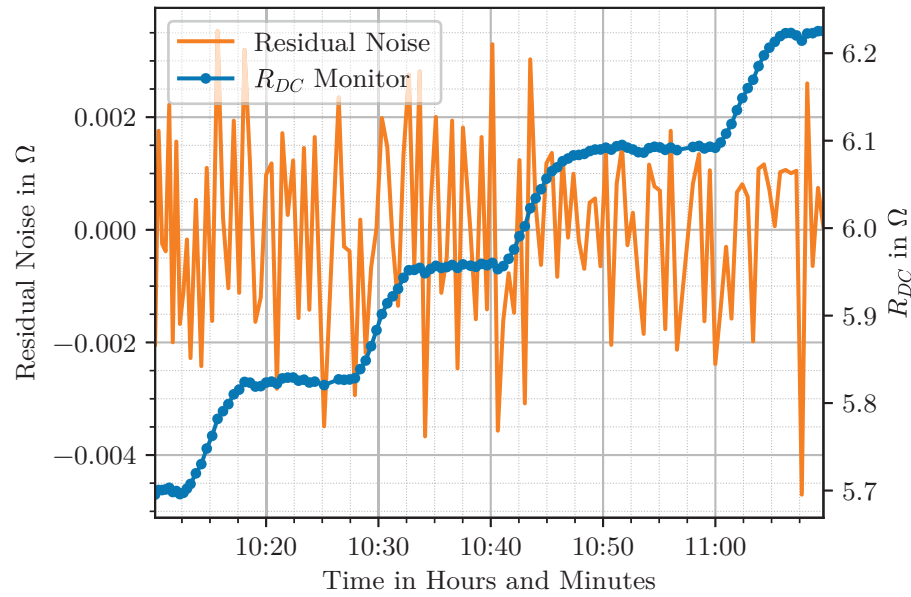


Figure 4.9: Residual noise after subtracting 3-sample moving average from monitored DC resistance signal. Short excerpt from full timeline.

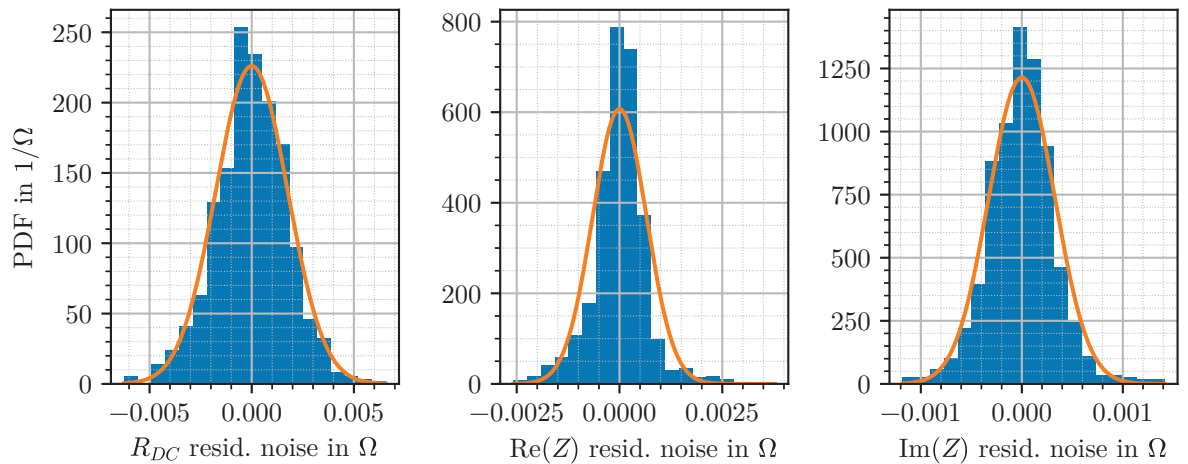


Figure 4.10: Probability density functions (PDFs) for residual noise after subtracting 3-sample moving average from monitored impedances. Data in blue histogram, fit normal distribution in orange.

4.4.3 Calibration Offset Error

The DC resistance measurement is directly affected by the offset of the interface calibration. This offset varied between runs and drifted during the measurement period, apparent from comparing the calibration before and after the measurements (see table 4.2).

Table 4.2: Calibration offset error where σ_s is the standard deviation.

| | Calibration Offsets in 10^{-4} V | | | |
|----------------|------------------------------------|-----------|-----------|-----------|
| | channel 1 | channel 2 | channel 3 | channel 4 |
| 1st run before | 3.1 | 3.4 | 2.4 | 5.3 |
| 2nd run before | 3.6 | 3.2 | 2.5 | 4.7 |
| 1st run after | 3.9 | 4.0 | 2.8 | 3.4 |
| 2nd run after | 4.5 | 3.6 | 3.1 | 4.3 |
| $2\sigma_s$ | 1.1 | 0.6 | 0.7 | 1.6 |

Please note the calculation of the standard deviation from only 4 values is prone to statistical errors in itself. We will also assume the offsets of each channel drift independently which is unlikely to happen in practice but allows the application of linear error propagation and results in an overestimation of the error.

To get the voltage over the speaker, channel 3 and 4 were subtracted. To propagate their errors, they are added to give $\pm 2.3 \cdot 10^{-4}$ V. The DC test signal at the 20 °C pulse measurement was 51 mV over the speaker, giving a relative error of $\pm 0.45\%$.

Channel 1 and 2 were subtracted to get the voltage over the shunt resistor. Their errors are added to give $\pm 1.7 \cdot 10^{-4}$ V. The DC test signal at the 20 °C pulse measurement was 15 mV over the shunt resistor, giving a relative error of $\pm 1.1\%$. The voltage over the shunt resistor is converted to the current signal through FFT, frequency-dependent multiplication and inverse FFT (IFFT). Since these are all linear operations, relative error stays unaffected according to linear error propagation.

The voltage over the speaker and the current are then divided to get resistance. The error can be estimated through linear error propagation by adding the relative errors. This gives a relative error of $\pm 1.6\%$ for the resulting DC resistance. At 50 °C the DC resistance was 7Ω , giving an absolute error of $\pm 0.12\Omega$.

4.4.4 Calibration Gain Error

As the gain is calibrated at much higher amplitude than the offset, it shows significantly less relative noise. However, there is also relative error to consider from the multimeter used for the reference voltage of around 9.375 V. The Fluke 8846A [52] was calibrated about a year before the measurement, putting it at a relative uncertainty of $2.4 \cdot 10^{-5}$

and an absolute deviation of $50\ \mu\text{V}$ in the $10\ \text{V}$ range. Adding both together at a voltage of $9.375\ \text{V}$ gives a relative error of $2.9 \cdot 10^{-5}$, that was added to the statistical error in table 4.3 to get the relative error Δ_{rel} . Adding relative errors assumes non-correlated error sources which is not quite right here as noise in the multimeter would also show up as noise in the calibrations, but leads to an overestimation of the error which is not as problematic as underestimating an error.

Table 4.3: Calibration gain error. \bar{g} is the arithmetic mean of the 4 gains for each channel and σ_s is the standard deviation.

| | Calibration Gains | | | |
|--|-------------------|-----------|-----------|-----------|
| | channel 1 | channel 2 | channel 3 | channel 4 |
| 1st run before | 1.02232 | 1.02245 | 1.02213 | 1.02217 |
| 2nd run before | 1.02232 | 1.02245 | 1.02214 | 1.02217 |
| 1st run after | 1.02229 | 1.02244 | 1.02215 | 1.02216 |
| 2nd run after | 1.02229 | 1.02244 | 1.02215 | 1.02217 |
| $2\sigma_s/\bar{g}$ | 0.00004 | 0.00001 | 0.00001 | 0.00001 |
| Δ_{rel} incl. multimeter | 0.00007 | 0.00004 | 0.00004 | 0.00004 |

To propagate this error according to linear error propagation, the DC and HF component will be treated separately in table 4.4 and table 4.5 respectively. In both tables, the relative error is first converted to absolute error Δ with typical values from the $20\ ^\circ\text{C}$ measurement. Then, the absolute errors of the subtracted channels are summed and again converted to relative errors to be summed between voltage and current signal as they are divided to give the impedance.

Table 4.4: Calibration gain linear error propagation for DC, going from the 4 channels to their differences to the final ratio.

| | channel 1 | channel 2 | channel 3 | channel 4 |
|-----------------------|---------------------|---------------------|---------------------|-------------------|
| Δ_{rel} | $7 \cdot 10^{-5}$ | $4 \cdot 10^{-5}$ | $4 \cdot 10^{-5}$ | $4 \cdot 10^{-5}$ |
| typ. DC voltage | 66 mV | 51 mV | 51 mV | 0 mV |
| Δ | 4.6 μV | 2.0 μV | 2.0 μV | 0 μV |
| Δ | 6.7 μV | | 2.0 μV | |
| typ. DC voltage | 15 mV | | 51 mV | |
| Δ_{rel} | $4.5 \cdot 10^{-4}$ | | $3.9 \cdot 10^{-5}$ | |
| Δ_{rel} | | $4.9 \cdot 10^{-4}$ | | |

The relative error of the DC resistance due to gain calibration errors is estimated at $4.9 \cdot 10^{-4}$ (table 4.4). This can be safely ignored as it is almost two magnitudes lower than the error due to offset calibration errors.

The relative error of the HF impedance due to gain calibration errors is estimated at $9.2 \cdot 10^{-4}$ (table 4.5). At $50\ ^\circ\text{C}$ the HF impedance was around $(9.7 + 7.8i)\ \Omega$, resulting

Table 4.5: Calibration gain linear error propagation for HF, going from the 4 channels to their differences to the final ratio.

| | channel 1 | channel 2 | channel 3 | channel 4 |
|-----------------------|---------------------|---------------------|---------------------|-------------------|
| Δ_{rel} | $7 \cdot 10^{-5}$ | $4 \cdot 10^{-5}$ | $4 \cdot 10^{-5}$ | $4 \cdot 10^{-5}$ |
| typ. HF amplitude | 134 mV | 118 mV | 117 mV | 1 mV |
| Δ | 9.4 μ V | 4.7 μ V | 4.7 μ V | 0 μ V |
| Δ | 14.1 μ V | | 4.7 μ V | |
| typ. HF amplitude | 16 mV | | 116 mV | |
| Δ_{rel} | $8.8 \cdot 10^{-4}$ | | $4.1 \cdot 10^{-5}$ | |
| Δ_{rel} | | $9.2 \cdot 10^{-4}$ | | |

in an absolute error of $\pm 8.9 \text{ m}\Omega$ for the real part and $\pm 7.2 \text{ m}\Omega$ for the imaginary part.

4.4.5 Parasitics

The cables from the shunt resistor and the speaker to the Datatranslation interface may incur a measurement error because they are not perfect conductors. Rather, they have some resistance and inductance in series to the cable. Between each two cables, there is only a finite isolation resistance and a small capacitance. These unwanted effects in the cables are called parasitics.

To roughly estimate their size, let's assume a solid copper wire of $l = 1 \text{ m}$ and a small cross section of $A = 0.1 \text{ mm}^2$. Assuming a copper resistivity of $\rho = 1.7 \cdot 10^{-8} \Omega \text{ m}$ (see fig. 3.2 on page 19), the parasitic resistance can be calculated as $R_p = \rho l / A = 0.17 \Omega$. Some non-systematic experimentation with the used clamps and a multimeter showed that contact resistances are on the same order of magnitude but tend to be different every time a contact is established.

The parasitic inductance of the wire with radius $r = \sqrt{A/\pi}$ can be estimated as $L_p = 2 \cdot 10^{-7} \text{ H} \cdot l \left(\ln \frac{2l}{r} - \frac{3}{4} \right) = 1.7 \cdot 10^{-6} \text{ H}$ [63, Formula 10] when straight wires in vacuum are assumed where their distance is much larger than their radius. At 34 kHz the resulting impedance is $j(0.4 \Omega)$.

Both parasitic resistance and parasitic inductance are about 7 orders of magnitude below the $1 \text{ M}\Omega$ input resistance of the Datatranslation interface. Therefore, almost no voltage is dropped over them and their influence is minimal. It should be noted though that some cables in the climate chamber were close to iron parts that may increase the parasitic inductance considerably, but probably not more than 4 orders of magnitude, making the resulting error still at least 3 orders of magnitude below the signal.

The isolation resistance of the cable is not infinite, but typical cables should have an insulation resistance of at least $1 \text{ M}\Omega$ [64, page 37]. The parasitic capacitance of two

cables separated by distance $D = 5$ mm can be estimated as $C = \frac{\pi\epsilon_0 l}{\ln \frac{D}{r}} = 8 \cdot 10^{-12}$ F [65, p. 52]. At 34 kHz the resulting impedance is $-j(6 \cdot 10^5 \Omega)$. Dielectric materials and different geometries can increase the parasitic capacitance. The Datatranslation interface itself has an input resistance of $1 \text{ M}\Omega$ and a capacitance of 20 pF . The input capacitance results in an impedance of $-j(2 \cdot 10^5 \Omega)$ at 34 kHz.

While both isolation resistance and parasitic capacitance have no effect on the measured voltage, they let current flow around the circuit rather than through it. Since the impedance in the circuit is on the order of 10Ω and the parasitics are 4 orders of magnitude larger, the effect is small.

Overall, errors due to parasitics are unlikely to affect DC measurements significantly, but at HF some conditions could lead to rising influence of especially the parasitic inductance up to around 10^{-3} . At 50°C the HF impedance was around $(9.7 + 7.8i) \Omega$, resulting in an absolute parasitic error of $\pm 9.7 \text{ m}\Omega$ for the real part and $\pm 7.8 \text{ m}\Omega$ for the imaginary part.

4.4.6 Crosstalk

Alternating currents in the cabling and the voice coil will induce magnetic fields which can induce voltages in other cables. Due to the highly geometric nature of this error, it is hard to estimate. Experiment 2 contains measurements with different cable layouts (section 5.4.5). There, by increasing the crosstalk, the real part of the HF impedance reduced by up to $130 \text{ m}\Omega$ (1.5 %) and the imaginary part increased by up to $180 \text{ m}\Omega$ (2 %). Due to the qualitative nature of that result, crosstalk will not be included in the error estimation for this experiment.

4.4.7 Further Ignored Errors

Any electrical, mechanical or acoustic resonance in the measurement setup or the speaker itself could influence the HF impedance a lot. As later seen in the impedance sweep results, the closest resonance to the 34 kHz HF tone is a resonance starting from 29 kHz at -25°C and going down in frequency and amplitude as temperature rises (fig. 4.15). It may be the source of the strange behavior of Z_e around -10°C (fig. 4.18). Considering it is likely for this to be a resonance in the speaker itself, it however is unlikely to be a measurement error in our exploratory survey and rather an error source of the HF method in general.

The integral non-linearity error of the Datatranslation interface is given at $\pm 6 \cdot 10^{-6}$ [50, user manual]. This non-linearity is likely small compared to any non-linearity the speaker shows (for example due to magnetic saturation) and is therefore ignored.

Any impact of measurement errors on the impedance sweep are not discussed as the broad frequency range and the deconvolution operation make this more complicated than for DC- or HF-signals. However, errors at high or low frequencies could be

considered similar to the ones for DC- and HF-signals and the in-between frequencies should be interpreted with care.

4.4.8 Error Summary

The reported temperatures are accurate to within ± 2.5 K. The error for the DC resistance is $\pm 0.12 \Omega$. For the HF impedance, statistical noise, calibration gain error and parasitics error are added to give ± 20 m Ω for the real part and ± 16 m Ω for the imaginary part. For Z_e , the errors of the HF impedance and DC resistance are added to give an error of $\pm 0.14 \Omega$ for the real part and ± 16 m Ω for the imaginary part.

4.5 Results

The results of the analysis are presented and interpreted in the following section.

4.5.1 Impedance Sweep

The magnitude of the impedance (fig. 4.11) shows a typical trend for a moving coil speaker: At low frequencies, the impedance converges to the DC-resistance that is seen to shift upwards with temperature. The impedance then rises to the main resonance that shifts from 1.3 kHz at -25°C to 350 Hz at 60°C . This is consistent with the expectation that the suspension becomes softer with higher temperature. Above the main resonance, there is a local minimum in the impedance before the impedance rises towards high frequencies due to inductance. Other small resonances around 100 Hz, 9 kHz, 12 kHz, 17 kHz and 28 kHz also show temperature dependent behavior, though less than the main resonance. A noisy part can be seen at 25°C around 5 kHz where a click was fixed by hand.

In the phase of the impedance (fig. 4.12) the main resonance shows up as a local rise and drop that shifts in frequency when the temperature changes. Towards high frequencies the influence of inductivity rises and the phase rises with it.

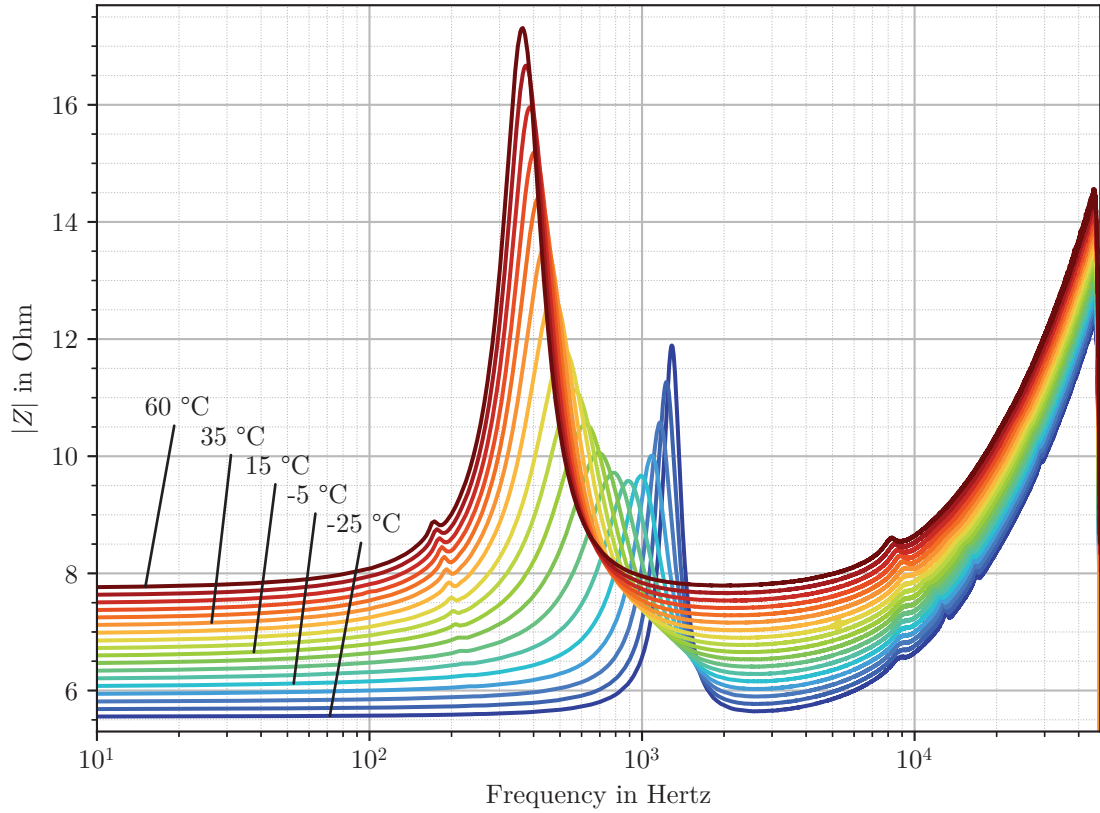


Figure 4.11: Impedance magnitude as measured by the sweep in 5 K steps.

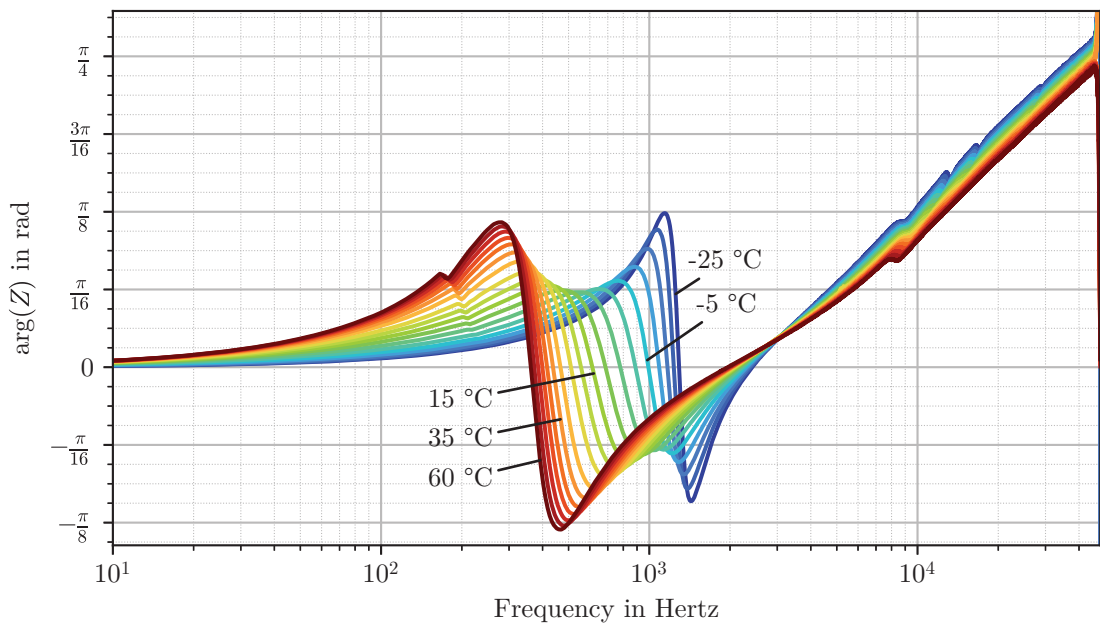


Figure 4.12: Impedance phase as measured by the sweep in 5 K steps.

4.5.2 Temperature Calibrations

The calibration of DC resistance vs. voice coil temperature is shown in fig. 4.13. The linear fit according to eq. (2.1) is developed around 20 °C. The fit parameters⁴ are $R_{DC,20} = (6.726 \pm 0.001) \Omega$ and $\alpha_{20} = (3.850 \pm 0.008) \cdot 10^{-3} \text{ K}^{-1}$. This value is in the expected range for copper wire (see page 20). The residuals do not indicate any remaining curvature.

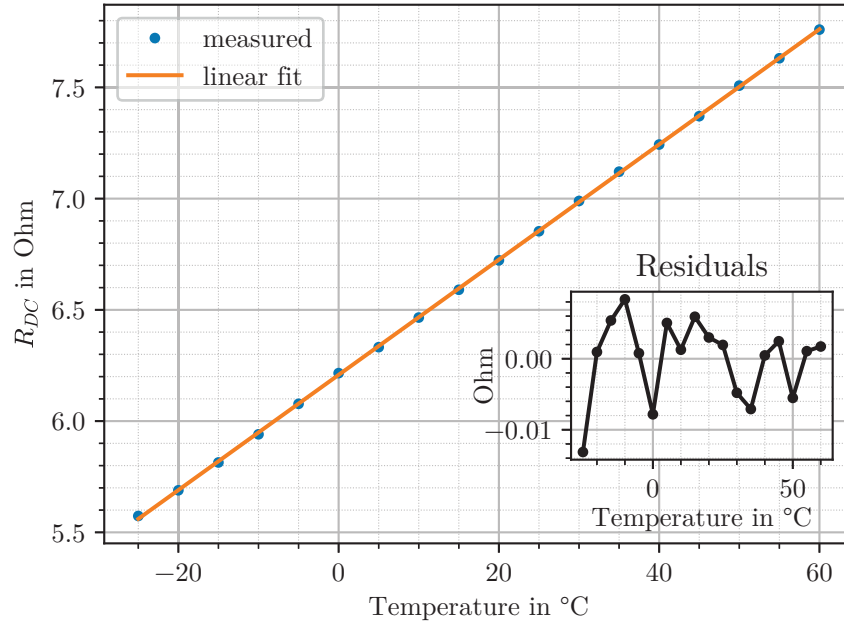


Figure 4.13: DC resistance vs. temperature. Linear calibration curve in orange.

The calibration of $\text{Im}(Z_e)$ vs. Eddy temperature is plotted in fig. 4.14. The data points show some curvature, so they were fit with a quadratic expansion around 20 °C:

$$\text{Im}(Z_e) \approx \text{Im}(Z_{e,20}) \left(1 + \alpha_{20}(\vartheta - 20^\circ\text{C}) + \beta_{20}(\vartheta - 20^\circ\text{C})^2 \right) \quad (4.9)$$

where ϑ is the temperature in °C. The parameters of the quadratic fit were $\text{Im}(Z_{e,20}) = (7.6101 \pm 0.0004) \Omega$, $\alpha_{20} = (1.058 \pm 0.001) \cdot 10^{-3} \text{ K}^{-1}$ and $\beta_{20} = (-5.2 \pm 0.5) \cdot 10^{-7} \text{ K}^{-2}$.

⁴All deviations are standard deviations unless otherwise noted.

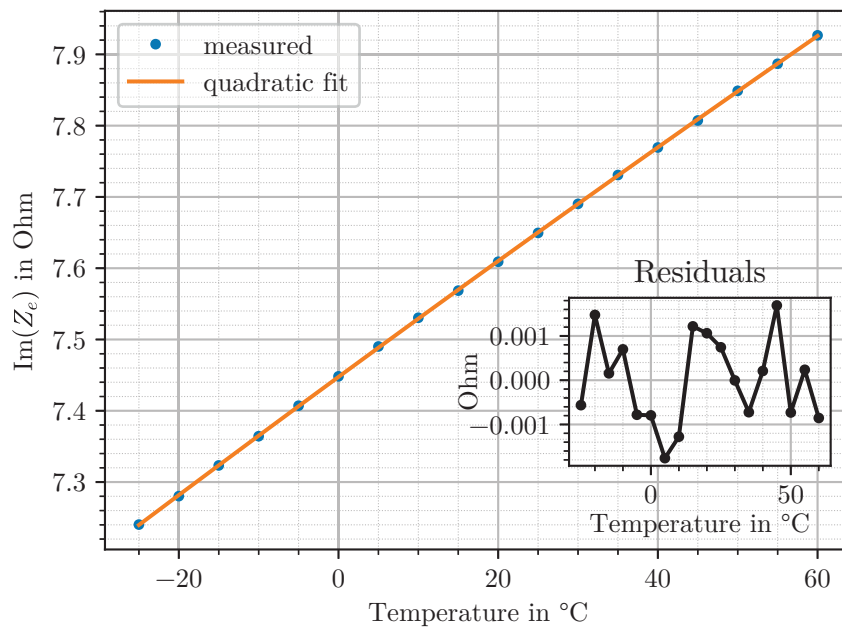


Figure 4.14: Imaginary part of Z_e at zero excursion vs. temperature. Quadratic calibration curve in orange.

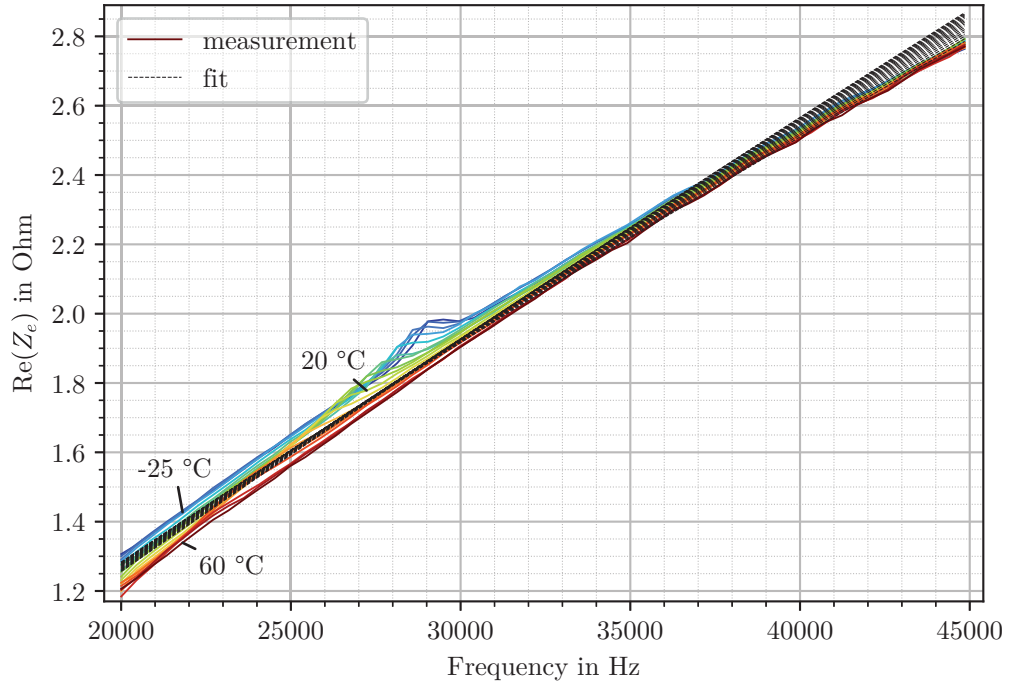


Figure 4.15: Real part of Z_e vs. frequency at different temperatures in 5 K steps. Fit of the Z_e model in black.

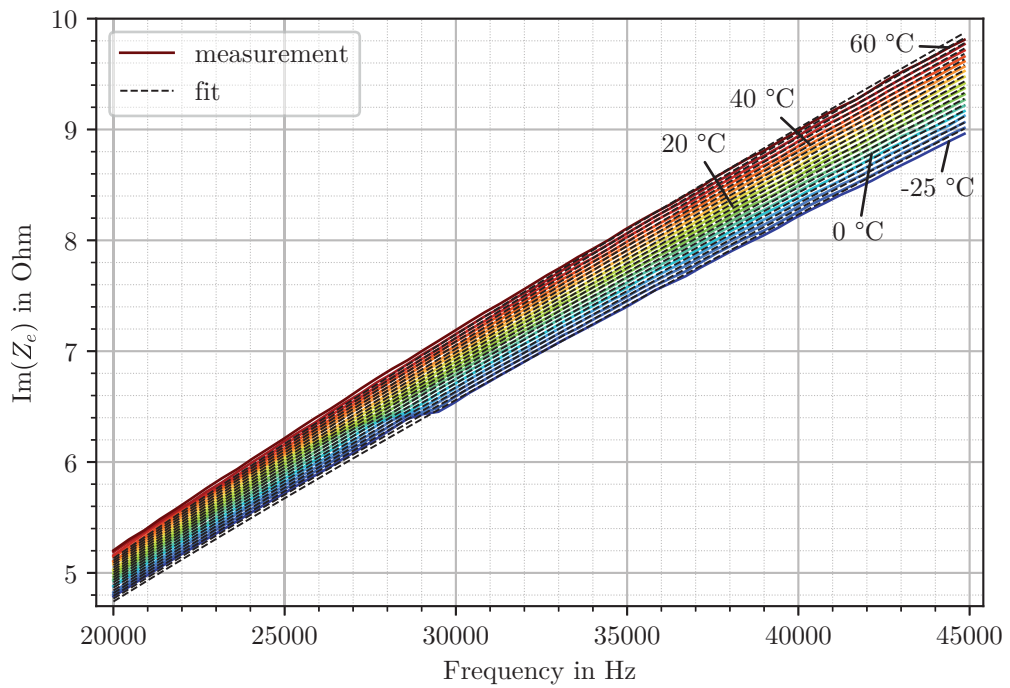


Figure 4.16: Imaginary part of Z_e vs. frequency at different temperatures in 5 K steps. Fit of the Z_e model in black.

4.5.3 Z_e -Model Fit

The fit of the Z_e -model described in section 3.5 and section 4.3.4 for different frequencies and temperatures can be seen in fig. 4.15 and fig. 4.16. The model matches the trend of the data, but it predicts the real part to change very little at lower ultrasonic frequencies when the temperature changes, which is not the case in the measurement data. Also, the curvature of the imaginary part with frequency is not quite adequately fit.

The parameters of the fit are seen in table 4.6. The parameter α describes the change of the semi-inductance with temperature. Vanderkooy [42] derived that this semi-inductance $K \propto \sqrt{\mu\rho}$. Both μ and ρ are expected to rise with temperature [31, 38] and therefore the positive sign of α meets expectations. The excursion parameter Γ at 0°C changes in the range from 23% to 39%. As expected the inside part of the voice coil is dominant as the iron attracts the magnetic field. The signs of β and γ are also positive, indicating that higher temperatures allow higher excursions, as would be expected since the suspension should become softer at higher temperatures. However some of this effect is also attributed to the impedance rising with temperature and therefore less voltage dropping over the shunt resistor, increasing voltage over the speaker and therefore excursion. The purely empirical excursion exponent η is slightly below 1 which does not agree with the model derived in section 3.5 where $\eta = 2$ was expected.

Table 4.6: Z_e model fit parameters.

| | |
|-------------------|--------------------------------------|
| l_0 | $3.508 \cdot 10^{-5}$ H |
| l_1 | $6.820 \cdot 10^{-5}$ H |
| k_1 | $2.757 \cdot 10^{-2} \Omega\sqrt{s}$ |
| α | $2.662 \cdot 10^{-3} \text{ K}^{-1}$ |
| Γ_0 | $3.041 \cdot 10^{-1}$ |
| $\Gamma_{\max,0}$ | $8.119 \cdot 10^{-2}$ |
| β | $1.855 \cdot 10^{-2} \text{ K}^{-1}$ |
| $\Gamma_{\min,0}$ | $-7.831 \cdot 10^{-2}$ |
| γ | $9.054 \cdot 10^{-3} \text{ K}^{-1}$ |
| η | $8.912 \cdot 10^{-1}$ |

Important for the HF method is the behavior of Z_e at the chosen frequency of 34 kHz. Its dependence on excursion and temperature is shown in fig. 4.17. Again, the model fits the trend of the measurement data. The measured value of Z_e at zero excursion has a slight tilt to the left as temperature rises whereas the model shows a slight tilt to the right (both shown in black). The resulting difference in the real part is less than 60 m Ω (about 2 K) and below the measurement error. This difference in tilt between data and model is likely explained by the influence of the main resonance peak. It causes the real impedance at high frequency to slightly go up. Since the main resonance goes down with temperature, the real part will be slightly decreased with rising temperature, which is exactly what is seen in the measured tilt of Z_e . This assumption was validated

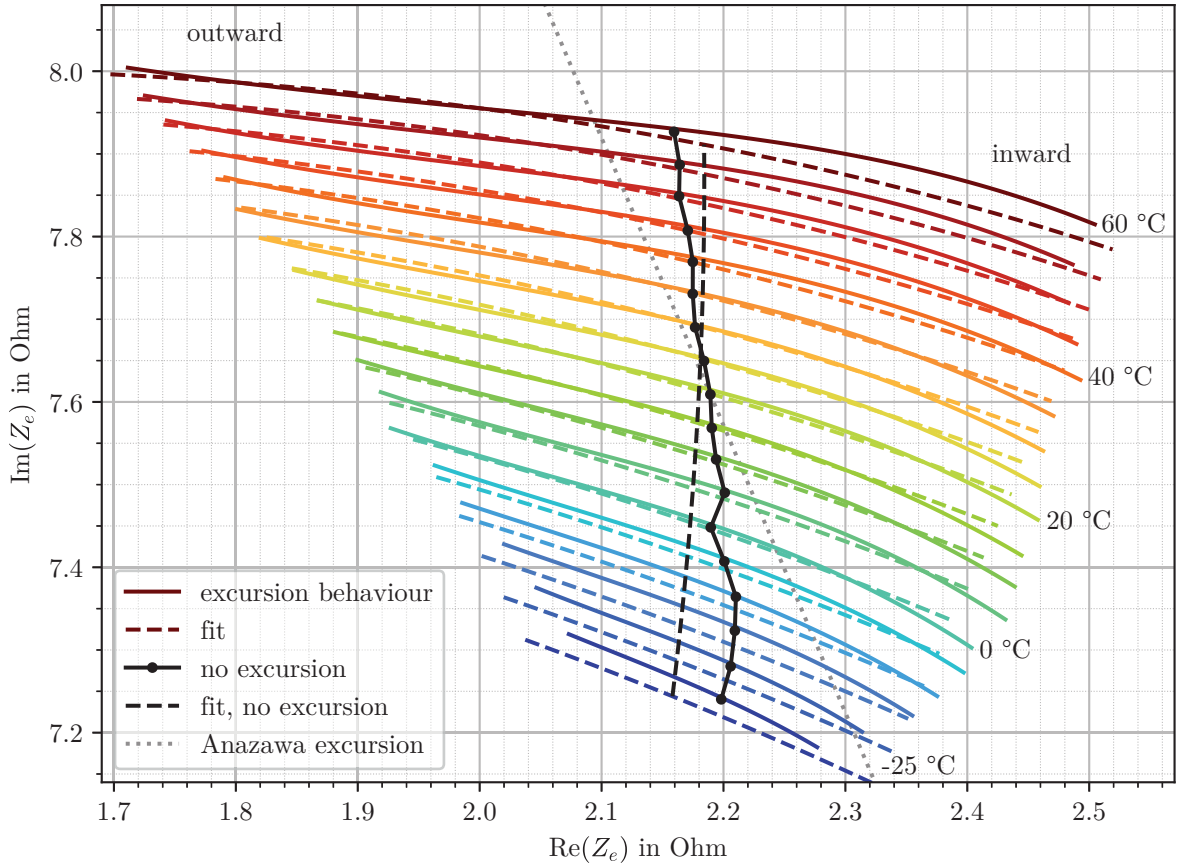


Figure 4.17: Extra impedance Z_e at 34 kHz on the complex plane. The behavior of Z_e for varying excursion is visualized by the colored curves. On the left side the voice coil moved outward, on the right side the voice coil moved inward. Each color represents a different temperature in 5 K steps. The black curve indicates the resting position with no excursion. The fit of the Z_e model is shown in dashed lines. Anazawa’s excursion correction [27] (eq. (2.2)) is developed around 20 °C and plotted as gray dotted line. It does not agree with the measured excursion behavior.

by extending the model with a temperature-dependent $R \parallel L \parallel C$ circuit in series to Z_e to model the temperature-dependent motional impedance. The modified model was fit over the whole audio range. Then the model was able to show the same tilt as the measurement data. Since audio-frequency impedance modelling is not part of this thesis and can get rather complicated, this model was not pursued further and the fit is not shown.

Earlier authors made various assumptions about the behavior of the HF impedance which can be evaluated with the measured data. Gautama [25] assumed that the real part of the HF impedance approximates the DC resistance. This would mean that the real part of Z_e is zero, which is clearly not the case. In fact, the real part of Z_e makes up one fourth of real impedance at 34 kHz (fig. 4.13 and fig. 4.17).

Anazawa in his first paper [26] assumed the real part of Z_e is constant. At 34 kHz, this is accurate to within $\pm 30 \text{ m}\Omega$ or $\pm 1 \text{ K}$. In his second paper [27], Anazawa assumed that excursion changes Z_e according to eq. (2.2) which is developed around 20°C and visualized in fig. 4.17 as a gray dotted line. For this specific speaker and frequency, it does not agree with the measured excursion behavior.

4.5.4 Eddy Temperature Correction

The slight influence of temperature on the real part of Z_e can be calibrated out by a regression between imaginary and real part of Z_e . For temperature measurement, the appropriate real part of Z_e is then calculated from the imaginary part. This Eddy temperature correction is shown in fig. 4.18. At zero excursion the linear fit has the form

$$\text{Re}(Z_e) \approx (-7.2 \pm 0.6) \cdot 10^{-2} \cdot \text{Im}(Z_e) + (2.73 \pm 0.04) \Omega \quad (4.10)$$

When DC and HF method are applied simultaneously in chapter 5 to compare their results, a different Eddy temperature correction is needed due to the excursion offset caused by the DC method. With such a DC offset of $(51 \pm 1) \text{ mV}$ at 20°C , the Eddy temperature correction becomes

$$\text{Re}(Z_{e,DC}) \approx (-9.8 \pm 0.6) \cdot 10^{-2} \cdot \text{Im}(Z_{e,DC}) + (2.91 \pm 0.05) \Omega \quad (4.11)$$

Also shown in fig. 4.18 is an approximation of the error due to high excursions. When the voice coil moves a lot, the lowpass on Z_e will average it over the whole excursion curve. To estimate the effect, the excursion curve was divided into an outward and inward part and the average of both parts was again averaged, yielding the curve shown in green in fig. 4.18. The changes in the imaginary part are small, but the real part might change up to $30 \text{ m}\Omega$ or 1 K when high excursion audio signals are played.

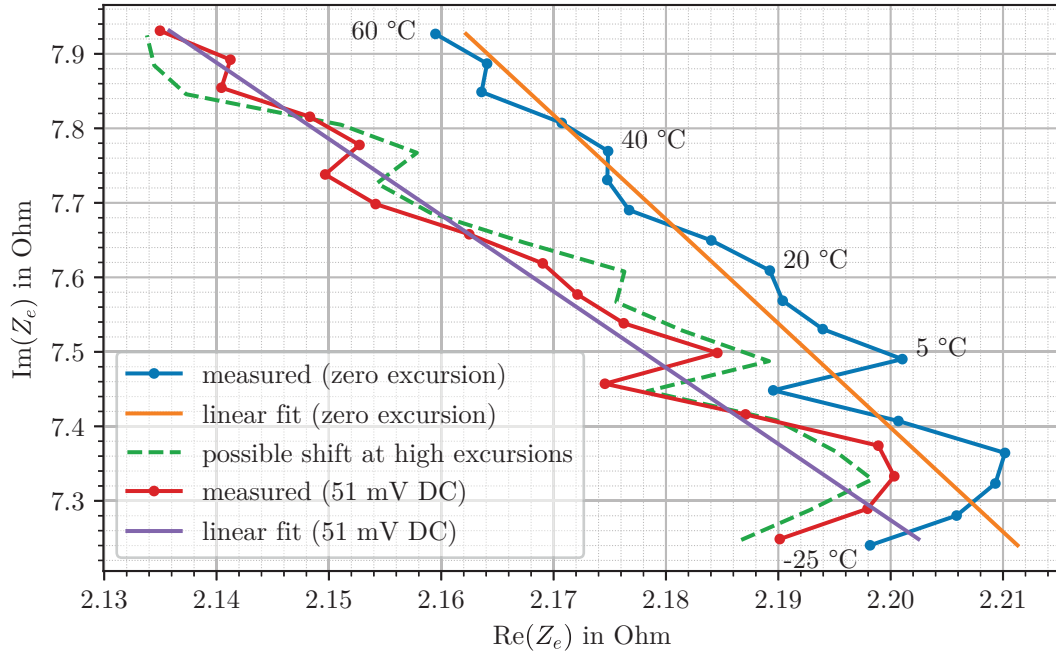


Figure 4.18: Extra impedance Z_e at 34 kHz on the complex plane. The curves visualize behavior with varying Eddy temperature. The blue curve is at the resting position without excursion. The red curve includes a DC offset of 51 mV. Linear calibration curves are fit through both data curves, forming the Eddy temperature correction. The green dashed line represents an attempt to represent what happens to the averaged Z_e while the speaker is driven to high excursions.

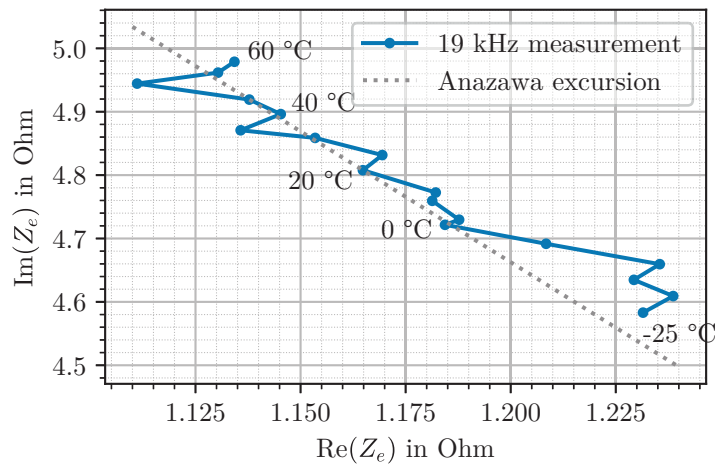


Figure 4.19: Extra impedance Z_e at 19 kHz on the complex plane. Zero excursion. Anazawa’s assumption on excursion [27] (eq. (2.2)) as gray dotted line, which is seen to roughly fit the data at varying temperatures.

4.6 Discussion

The HF method depends on knowing Z_e at all times to accurately calculate the DC resistance from the HF impedance. Z_e was shown to have a significant excursion dependence. The real part of the HF impedance can be modulated by the audio signal by about $\pm 0.3\Omega/6.7\Omega = \pm 4\%$. This must be filtered out with a lowpass. After filtering, an error of less than 1 K is expected to remain due to non-linearity of the excursion-dependence. This still is an advantage for the HF method compared to the DC method, where the main audio signal must be filtered out that has an amplitude which is easily 100 times larger than the DC signals, whereas the HF method must only filter out an audio signal modulation of 4%. This creates an advantage of factor 2200 for the HF method in terms of out-of-band error if no leakage of the audio signal to the HF region is assumed.

However, the excursion dependence might still be critical as the resting position tends to drift over time or change in response to large inputs. This could incur an error of 10 K or more. Adaptive offset stabilization could offer a solution for this problem [66].

In comparison to the DC method, the HF method can be used to not only measure the voice coil temperature, but also the surface temperature of the pole plates through Eddy currents and the imaginary part of the HF impedance. This relationship could be accurately fit with a quadratic function. Using Eddy currents to measure temperature is, of course, nothing new [67]. This opens up new possibilities for thermal models because they would not have to integrate the temperature of the structures surrounding the voice coil from the electrical power, they could just measure it.

Anazawa's second paper [27] claimed to offer a correction for the excursion dependence of Z_e . However this already seemed unlikely as his error was the same whether he used a 40 Hz or 5 kHz tone and the excursion error should have been minimal at high frequencies. Additionally, the speaker used in this thesis showed a rather different excursion behavior at 34 kHz. However, Anazawa did his measurements at 19 kHz and at that frequency his correction does work well as Eddy temperature correction (fig. 4.19). This supports the hypothesis that Anazawa's excursion correction is in fact a correction for Eddy temperature.

The Z_e model derived in section 3.5 was able to fit the trend of the measured impedance with regard to frequency and temperature with some small deviations. The excursion dependence did not work as expected and needed an empirical variable to fit the data. The motional impedance had a visible effect on the HF impedance but was within the margin of error.

Finally, measurements of DC resistance requires voltage measurement with precisely known DC offsets. Therefore, the DC offset calibration should have averaged the offset over significantly longer than 1 s to achieve lower error in the resistance measurement.

5 Experiment 2: Different Audio Signals

While experiment 1 was designed for explorative characterization and calibration, experiment 2 is intended to show the HF method temperature measurement in action. DC and HF method are applied simultaneously and compared while the speaker is heated with different audio signals for thermal excitation. If the previously performed calibration is sufficient and accurate, DC and HF method are expected to agree. Further, the Eddy temperature is expected to behave like the magnet/iron temperature. An additional measurement was done to judge the size of crosstalk error.

5.1 Test Signals

All test signals consisted of a constant DC offset and a constant HF tone, both of similar amplitude as in experiment 1 and unlikely to heat the speaker significantly. Overlaid on these measurement signals was a thermal excitation signal meant to heat the speaker.

The first group of thermal excitation signals were designed to provide heat with very little voice coil movement. They consisted of pink noise from 5 kHz to 20 kHz. It was created in the frequency domain by imposing an amplitude spectrum $\propto 1/\sqrt{f}$ in the given frequency range and a uniformly random phase. It was then transformed to the time domain with an IFFT and normalized to a target RMS. Finally, the signal was windowed with a Tukey window (2 ms fade time at beginning and end) and padded to the recording time of 60 s. The lengths of the pink noise were 0.2 s, 2 s and 20 s. The shortest excitation time is expected to only heat the voice coil, while the longer heat time should heat both voice coil and surrounding parts.

The medium length measurement of 2 s was repeated with a pink noise spectrum from 500 Hz to 20 kHz. Compared to the higher frequency spectrum, this should reveal the influence of voice coil movement on the temperature measurement.

The last signal was a 20 s logarithmic sweep [46] from 500 Hz to 20 kHz, used to differentiate between different frequencies. It was windowed and padded the same as the pink noise.

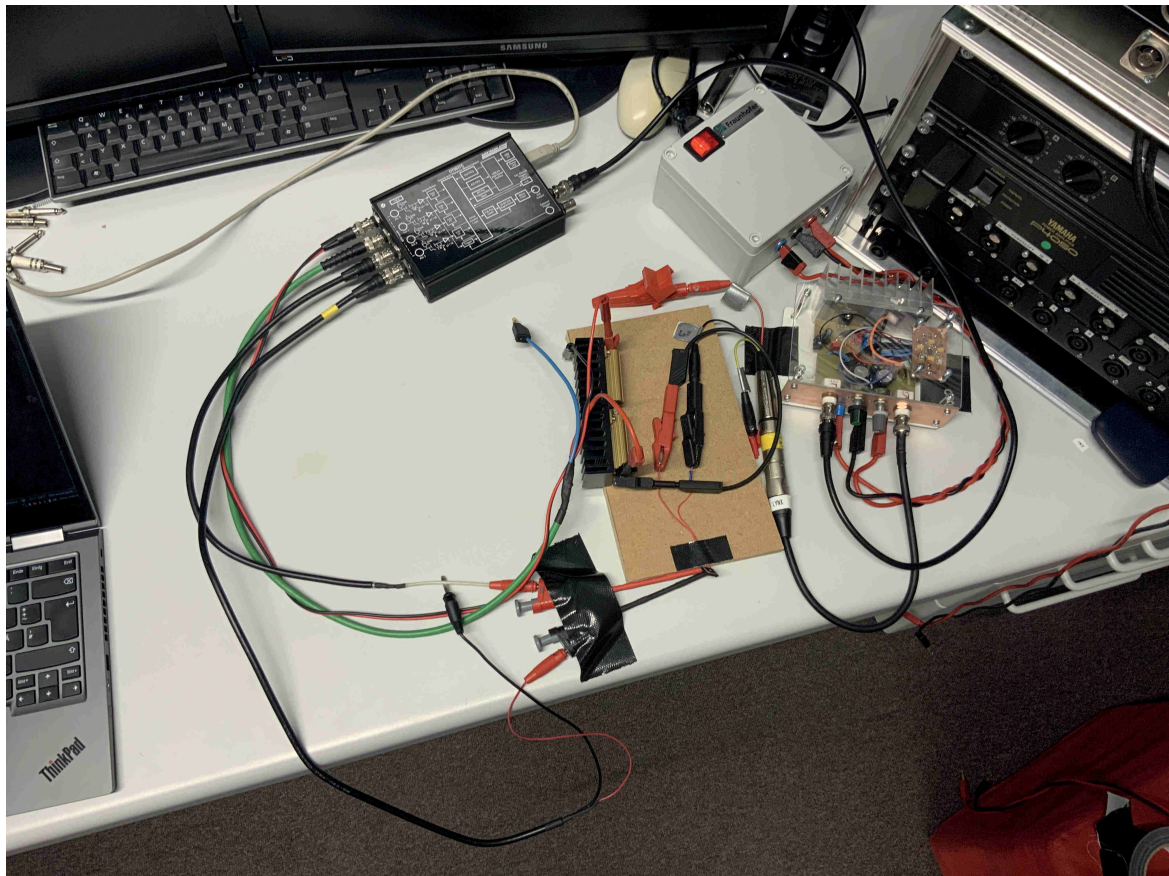


Figure 5.1: Experiment 2 setup. Amplifier on the right with copper faceplate and aluminium heatsink. Amplifier power supply behind in gray box. Speaker taped down on the front of the wooden board. Voltage sensing wires on the left side.

5.2 Experimental Setup and Procedure

The measurement setup was quite similar to experiment 1, but on a lab bench instead of the climate chamber (fig. 5.1). The amplifier from experiment 1 broke and was replaced with one that was swiftly put together by one of the team members at Fraunhofer IDMT. The new amplifier was based on an RFT A2030H [68] chip and offered an adjustable DC offset. This offset was adjusted to (51 ± 1) mV over the speaker, as in the climate chamber at 20°C . The gain of the amplifier was adjusted to yield an HF-tone amplitude of (116 ± 2) mV, as in the climate chamber at 20°C .

The Datatranslation interface was calibrated before and after all other measurements, twice each. The spread in calibration was comparable to the one in experiment 1.

During wiring of the experiment care was taken to twist differential wire pairs as much as possible and keep current-carrying wires away from voltage-sensing ones.

Then, the test signals were played while recording the voltages over the shunt and

Table 5.1: Thermal excitation signals with amplitude scales and pause times afterward.

| Thermal Excitation Signal | Scale | Pause | Notes |
|--------------------------------------|-------|--------|------------------------------|
| Pink noise, 5 kHz to 20 kHz, 0.2 s | 0.85 | 5 min | |
| Pink noise, 5 kHz to 20 kHz, 2.0 s | 0.75 | 8 min | Clipping once at about 5.5 s |
| Pink noise, 5 kHz to 20 kHz, 20 s | 0.70 | 19 min | |
| Pink noise, 0.5 kHz to 20 kHz, 2.0 s | 0.70 | 8 min | |
| Log sweep, 0.5 kHz to 20 kHz, 20 s | 0.70 | 15 min | |

speaker. The thermal excitation signals were all scaled to the same RMS power of approximately 700 mW, but this clipped the Datatranslation interface and the amplitude had to be scaled down (table 5.1) to not exceed 10 V. Care was taken to ensure the speaker had completely cooled down before running the next test. Test Signals without thermal excitation were played to check that the temperatures had stabilized. This led to the pause times noted in table 5.1.

After running all test signals successfully, one was repeated without the DC offset from the DC method to judge the effect of excursion offsets. To judge the effect of crosstalk, the same test signal was repeated with two more wiring setups.

5.3 Analysis Methodology

The recorded data was analyzed similarly to experiment 1 (section 4.3), yielding a signal of impedance or resistance over time. To calculate the voice coil temperature from DC resistance, the calibration from fig. 4.13 is used. To calculate the Eddy temperature from the imaginary part of the HF impedance, a calibration similar to fig. 4.14 is used, but with applied DC offset. The calibration with DC offset is slightly different as the imaginary part of the HF impedance changes slightly with temperature. To calculate the temperature with the HF method, first $\text{Re}(Z_e)$ is calculated from $\text{Im}(Z_e)$ with the calibration in fig. 4.18. Then, the DC resistance is calculated by $R_{DC} \approx \text{Re}(Z) - \text{Re}(Z_e)$ and converted to the temperature with the same calibration as for the DC method.

To visualize the signal applied to the speaker, a spectrogram of the voltage over the speaker is calculated with the same windowing as the impedances. The linear frequency axis of this spectrogram is resampled to a quadratic frequency axis with a linear interpolation/moving average algorithm. The quadratic frequency axis gives better resolution at lower frequencies like a log scale, but still allows visualization of the DC component.

5.4 Results

The main results can be seen in figs. 5.2 to 5.6. In all plots, the topmost plot is a spectrogram showing the voltage over the speaker. Please note the quadratic frequency axis and the moving average downsampling severely distort the Bandwidth and Size of the test tones at DC and 34 kHz. In reality, both are of about equal size and bandwidth. Also keep in mind the spectrogram values are in frequency bands of fixed bandwidth and a pink noise will fall off with 3 dB/oct. The middle plot shows the three measured temperatures via the DC method, HF method and the Eddy temperature from the imaginary part of the HF impedance. The third plot shows the difference between the DC and HF method on an enlarged scale.

At the beginning of all excitation signals there is a broadband noise above 20 kHz that suddenly ends after 0.5 s to 12 s. The source of this noise is unknown.

5.4.1 Eddy Temperature

In all plots the Eddy temperature is lowered by 8 K to match the other temperatures. It is unknown why the Eddy temperature was consistently measured 8 K too high during all measurement runs. This equals a difference of about 60 m Ω between experiment 2 and experiment 1 while the error for the imaginary part was estimated at only ± 20 m Ω . Therefore, there must be a systematic difference between experiment 1 and experiment 2 that significantly affects the imaginary part of the HF impedance. Possible sources are crosstalk error (discussed in the next section), influence of the metal in the climate chamber on Eddy currents, temperature convergence error or hysteresis-effects in the magnetic behavior due to the heating-cycle [38].

The next interesting aspect is that the Eddy temperature jumps up 3 K to 6 K whenever a signal is applied and immediately jumps down again when the signal ends. The comparison of fig. 5.2 and fig. 5.3 is especially interesting: if a high frequency noise is applied, the Eddy temperature jumps up 5 K once the signal starts and again jumps 5 K down when the signal ends. If a sweep from 0.5 kHz to 20 kHz is applied, the Eddy temperature does not jump up when the signal starts, it actually goes down a bit when the 500 Hz signal starts. Then, at the end of the sweep, the Eddy temperature drops strongly by 6 K. No jumps are visible in between with the Eddy temperature steadily rising. Clearly, the jump in the Eddy temperature rises smoothly with the frequency of the applied thermal excitation signal. The jump also seems to rise with the amplitude of the applied signal, as can be seen when comparing fig. 5.4 at 70 % amplitude to fig. 5.5, which has a stronger focus on higher frequencies and is played at 75 % amplitude. A plausible explanation for this phenomenon is induction heating: The Eddy temperature is measured on a thin layer on the surface of the pole plates (see page 30). But this thin layer is also where Eddy currents cause induction heating. Because the layer is so thin, its thermal mass is low and it can change its temperature quickly and strongly with comparatively little power needed. Once the signal stops, the heat in the Skin layer is quickly dissipated into the bulk of the material and the

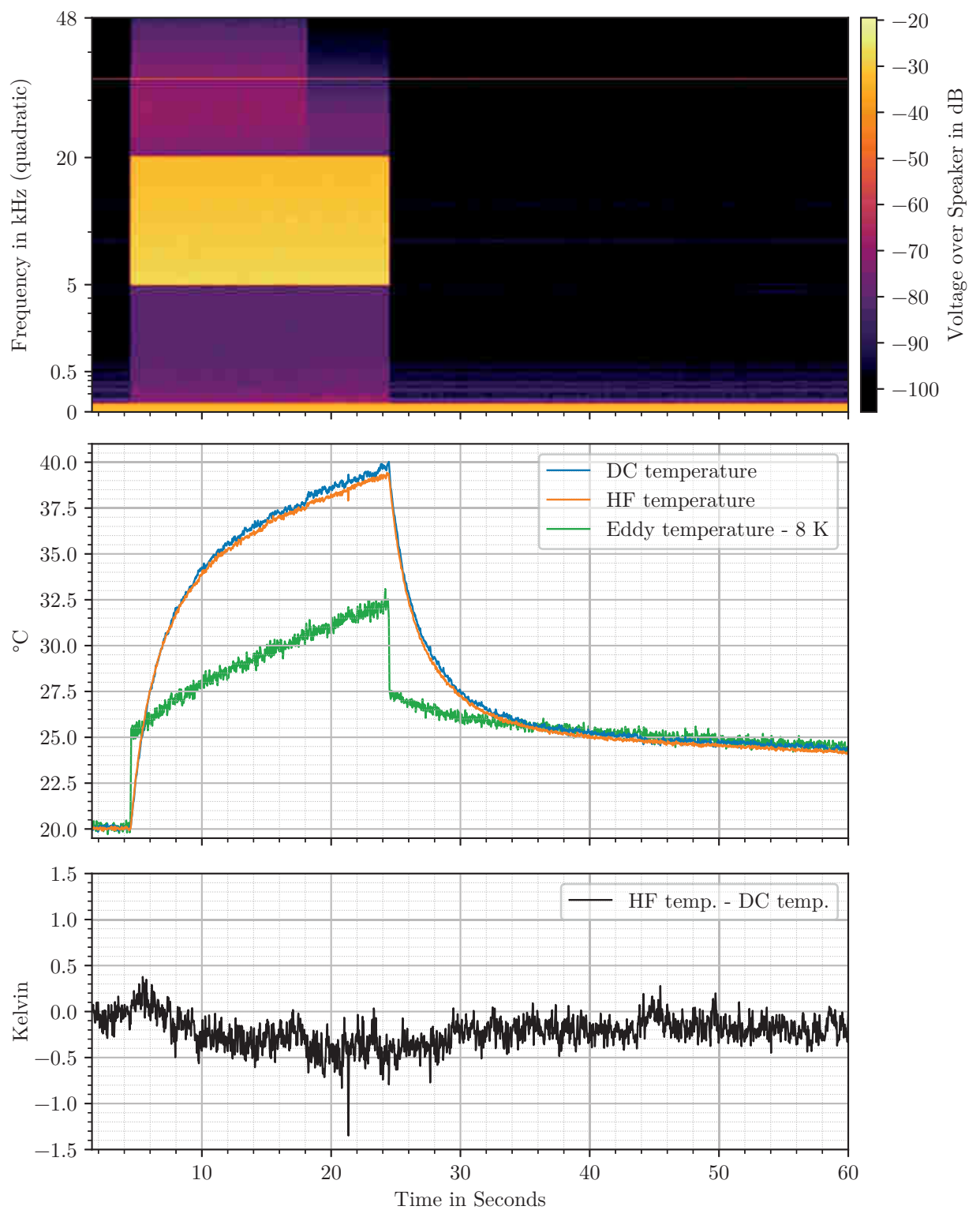


Figure 5.2: Temperature measurement with pink noise, high spectrum, long length.

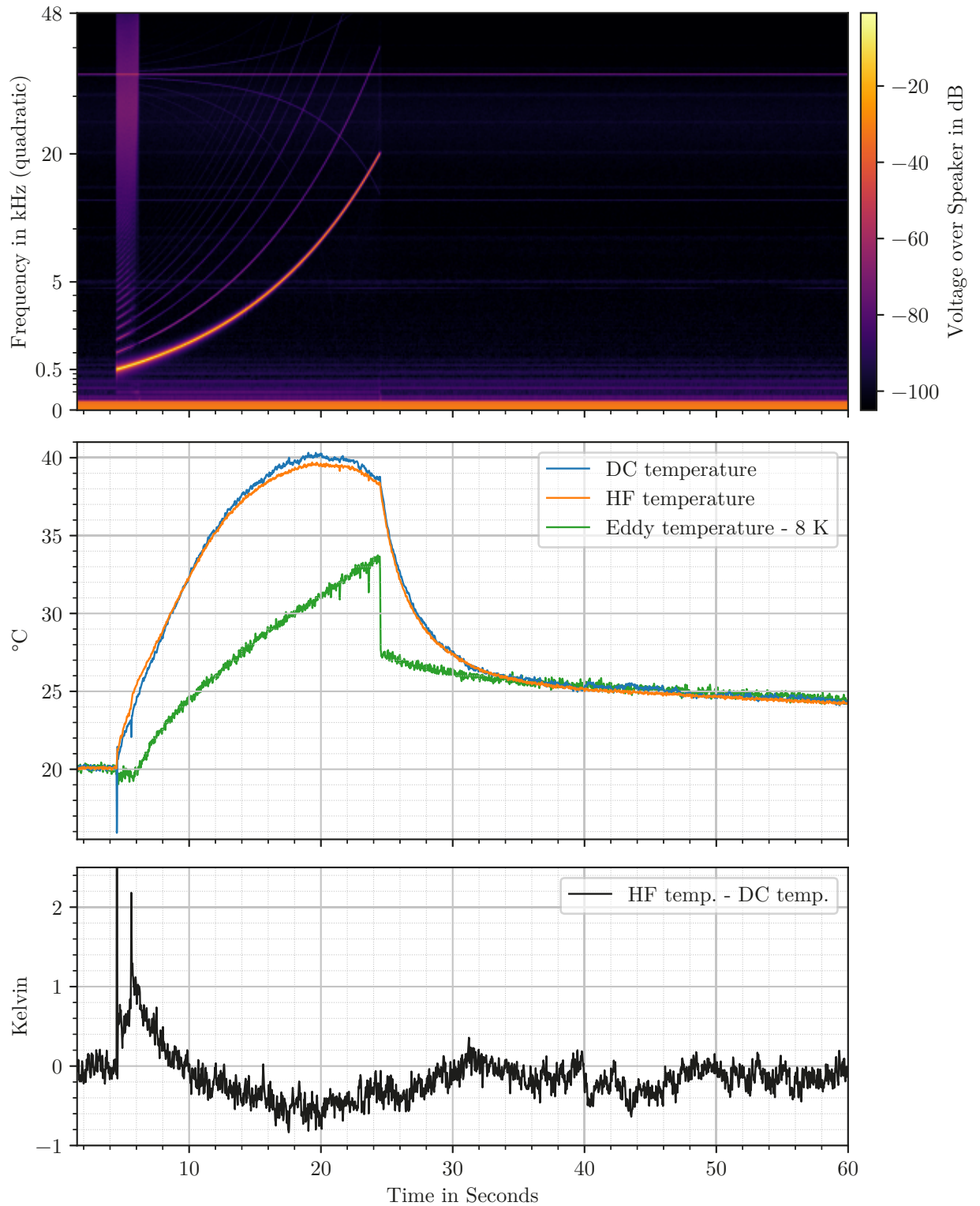


Figure 5.3: Temperature measurement with logarithmic sweep. Intermodulation distortion is clearly visible as the lines going out from the HF frequency as the sweep frequency goes up.

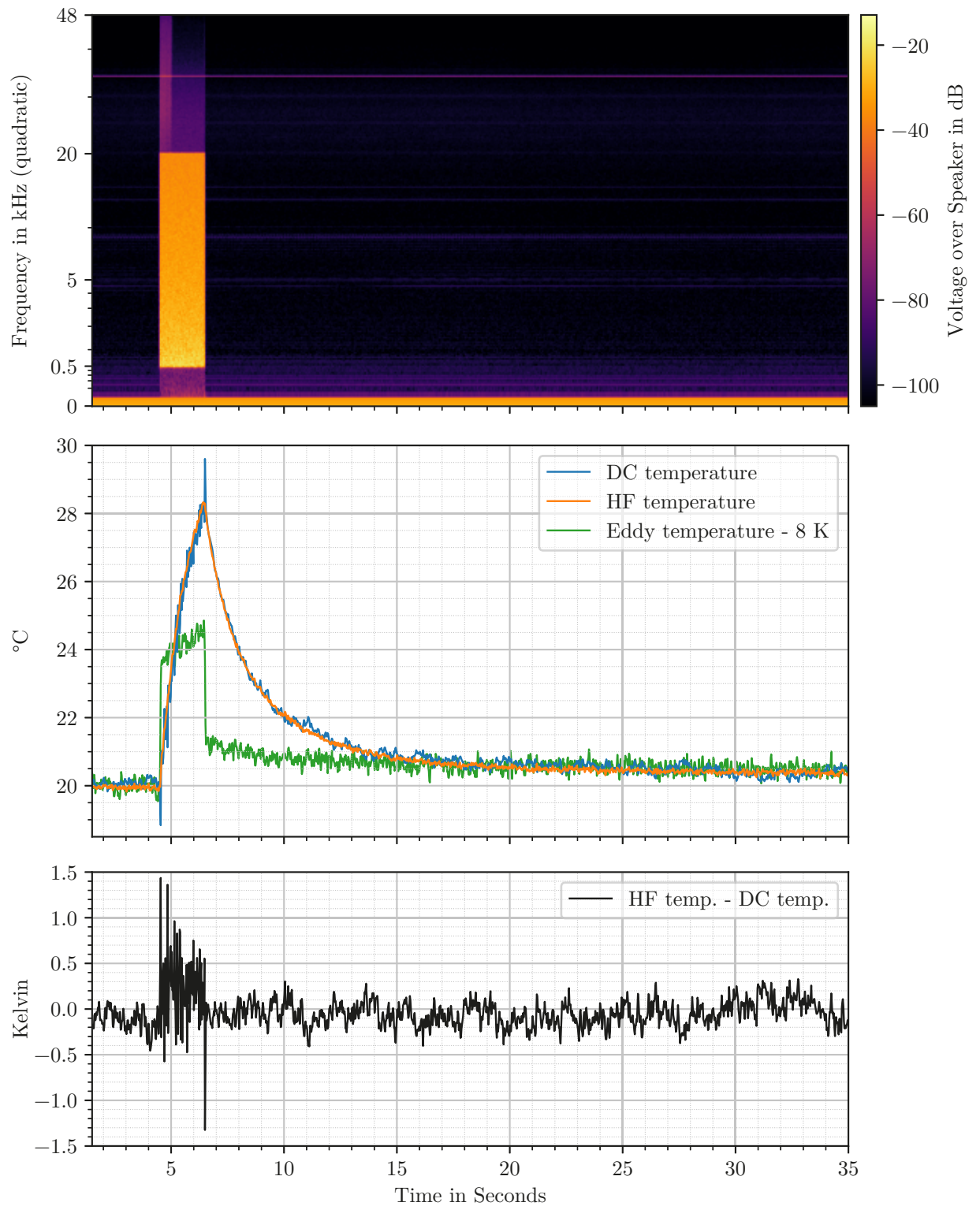


Figure 5.4: Temperature measurement with pink noise, low spectrum, medium length.

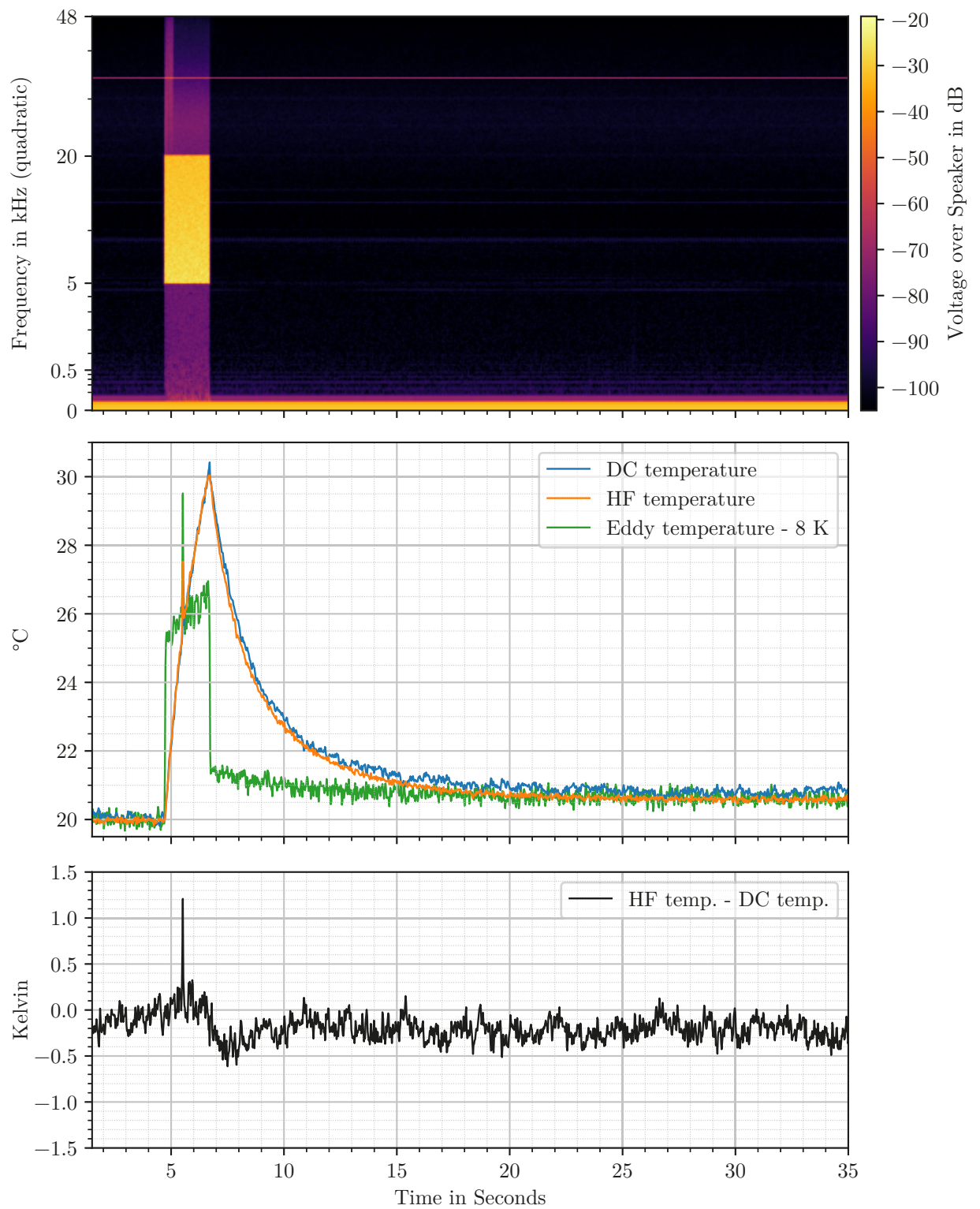


Figure 5.5: Temperature measurement with pink noise, high spectrum, medium length. Clipping at around 5.5s.

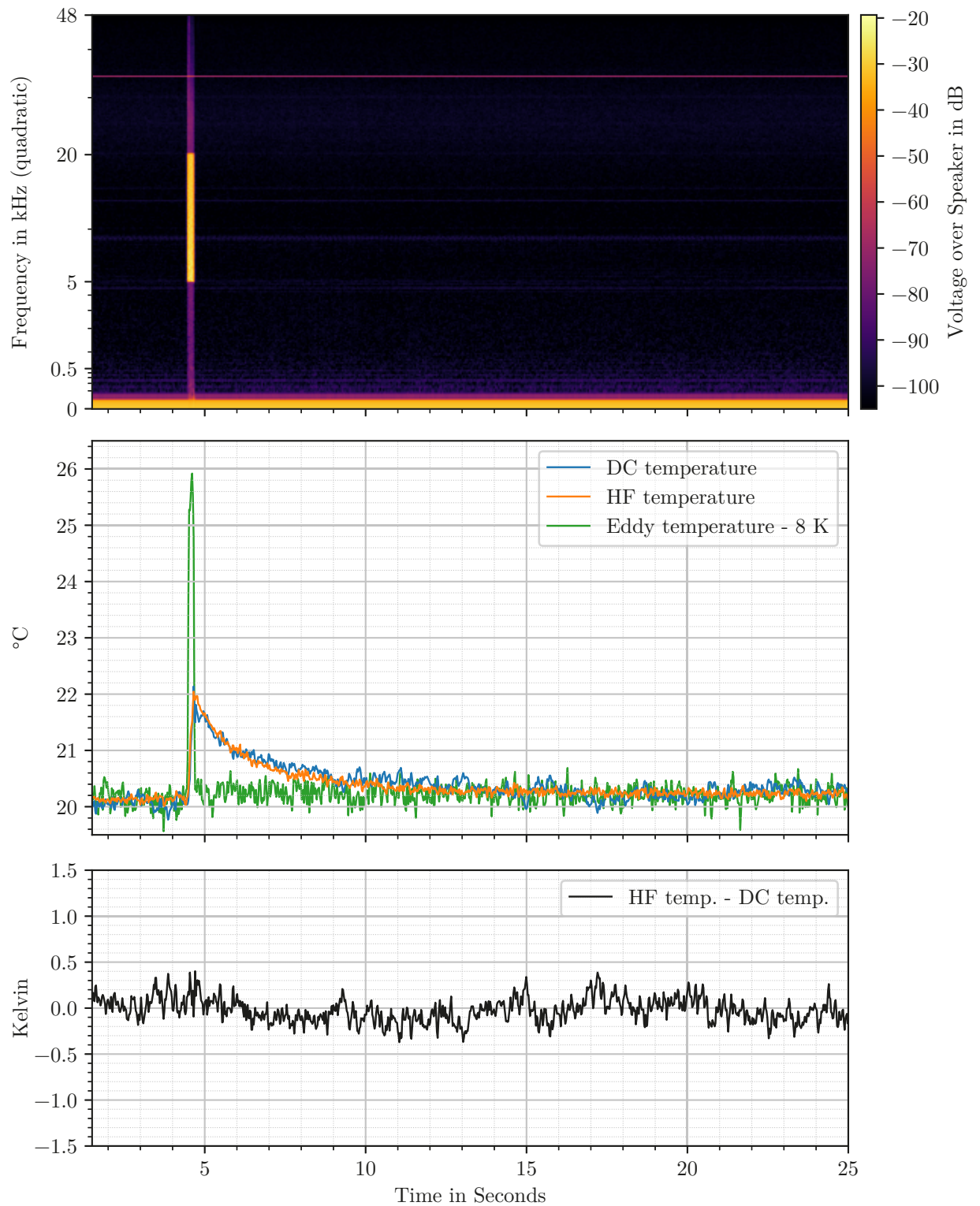


Figure 5.6: Temperature measurement with pink noise, high spectrum, short length.

Eddy temperature drops again. Since induction heating smoothly becomes stronger with rising frequency and is proportional to the power applied to the speaker, it fits the characteristics shown by the Eddy temperature jumps.

A central hypothesis of this paper is that the Eddy temperature is closely related to the temperature of the pole plates. Since the iron has a much larger thermal mass than the voice coil, its temperature is expected to rise and fall slower than the voice coil temperature. Also, one would expect the voice coil temperature not to fall below Eddy temperature. This can be seen in all measurements: With a short noise burst (fig. 5.6), the Eddy temperature does not significantly rise at all. With the medium length burst (fig. 5.5), the Eddy temperature rises 1.5 K and then cools down very slowly, still being about half a Kelvin from its starting temperature at the end of the plot. The difference between voice coil temperature and Eddy temperature becomes most clear in the longest noise burst (fig. 5.2), where the voice coil temperature rises 20 K, but the Eddy temperature only rises 7 K. The voice coil temperature quickly cools down to the level of the Eddy temperature after about 12 s, but then only slowly cools down together with the Eddy temperature. This supports the hypothesis that the Eddy temperature actually measures the temperature at the surface of the pole plates.

5.4.2 DC Temperature

When a high-frequency signal is played, the DC temperature is free from unexpected artifacts (except for the clipping in fig. 5.5). When a lower frequency noise is played (fig. 5.4), the DC method shows increased noise and spikes when the signal starts and ends. The spikes at the start and end can be expected to be due to the signal not being faded in and out slowly enough (half-Hann window, 2 ms) and would likely disappear if the thermal excitation signal were filtered with a steeper highpass after padding. The out-of-band noise from low-frequency signals could be improved by applying a steeper lowpass to the voltage and current signals (currently 70 ms Hann window).

When judging effects compared to the DC method, it should be kept in mind that the possible error due to calibration offset drift is $\pm 1.6\%$ (95 % confidence, see page 47) or about ± 4 K.

5.4.3 HF Temperature

The HF temperature is mostly free from unexpected artifacts, again with the exception of the clipping event in fig. 5.5. With the sweep (fig. 5.3), a strange sudden rise in temperature is seen around 5.5 s that is not mirrored by the DC temperature. It might be related to strong voice coil movement around resonance or the strange broadband high-frequency noise that suddenly disappears right around the same time. Also, some small spikes (< 0.3 K) can be seen in the HF temperature when the first and second overtone of the main sweep cross the HF frequency.

5.4.4 Comparison of HF and DC Temperature

When looking at the residuals between HF and DC temperature, the agreement is generally good and within the margin of error for the DC temperature of ± 4 K. However, when looking at fig. 5.5 and fig. 5.2, the residual tends to go down about 0.5 K when voice coil temperature increases. This effect is not seen in fig. 5.4, where the residual seems to actually rise a bit, but it is hard to tell with the increased noise in the DC temperature. The sweep (fig. 5.3) gives further insight as lower frequencies with high excursion seem to make the residual rise by up to 1 K and higher frequencies with only heat and no excursion seem to lower the residual by about 0.5 K.

On page 58 it was predicted that high excursion, low frequency audio signals could lower the HF temperature by up to 1 K. This is not seen in the measurements, instead the HF temperature goes up when a high excursion, low frequency audio signal is played. This might mean the method to estimate the excursion error is insufficient, considering it does not consider how much time the voice coil spends at each position. Another explanation for the excursion-associated error is that transducers tend to show some offset in the voice coil position when driven to their limits due to asymmetry [69].

The noise of the HF temperature is about 15 dB to 20 dB below that of the DC temperature (fig. 5.7) with the same lowpass applied for both. However, the DC voltage was 51 mV and the RMS voltage of the HF tone was 82 mV or 4 dB above the DC voltage.

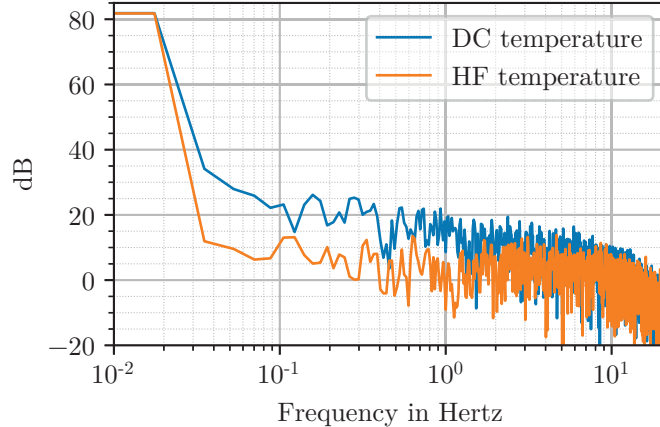


Figure 5.7: Spectra of DC and HF temperature vs. frequency. Test run without thermal excitation.

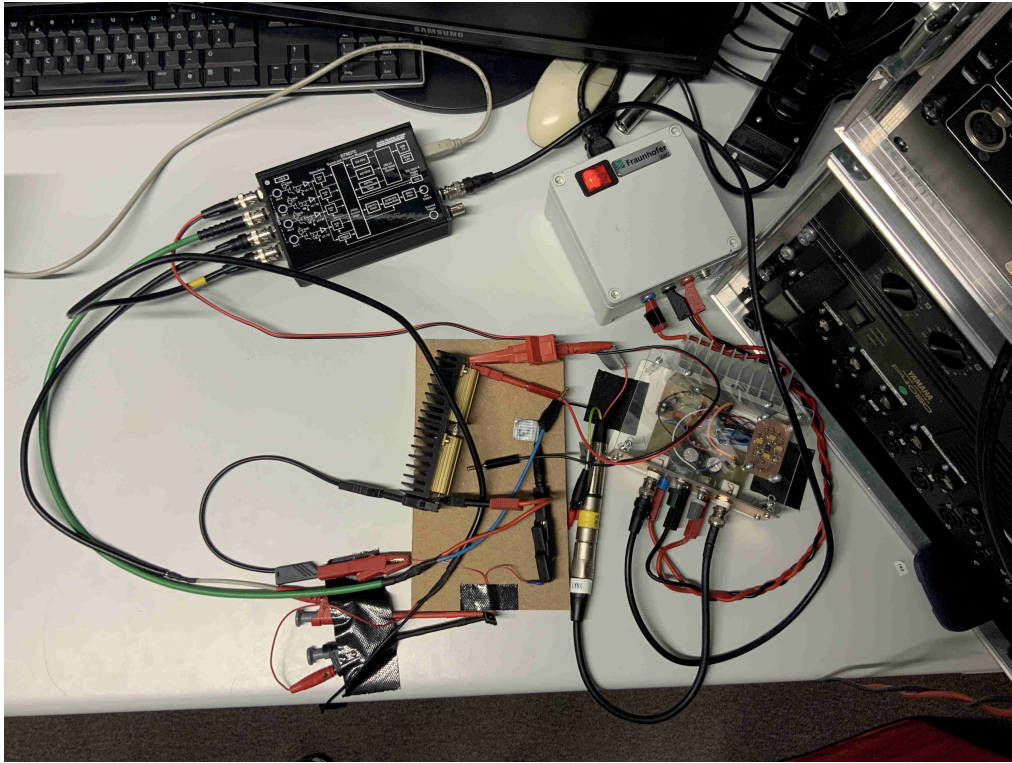


Figure 5.8: Strong crosstalk setup. Note voltage sensing wires over current-carrying wires.

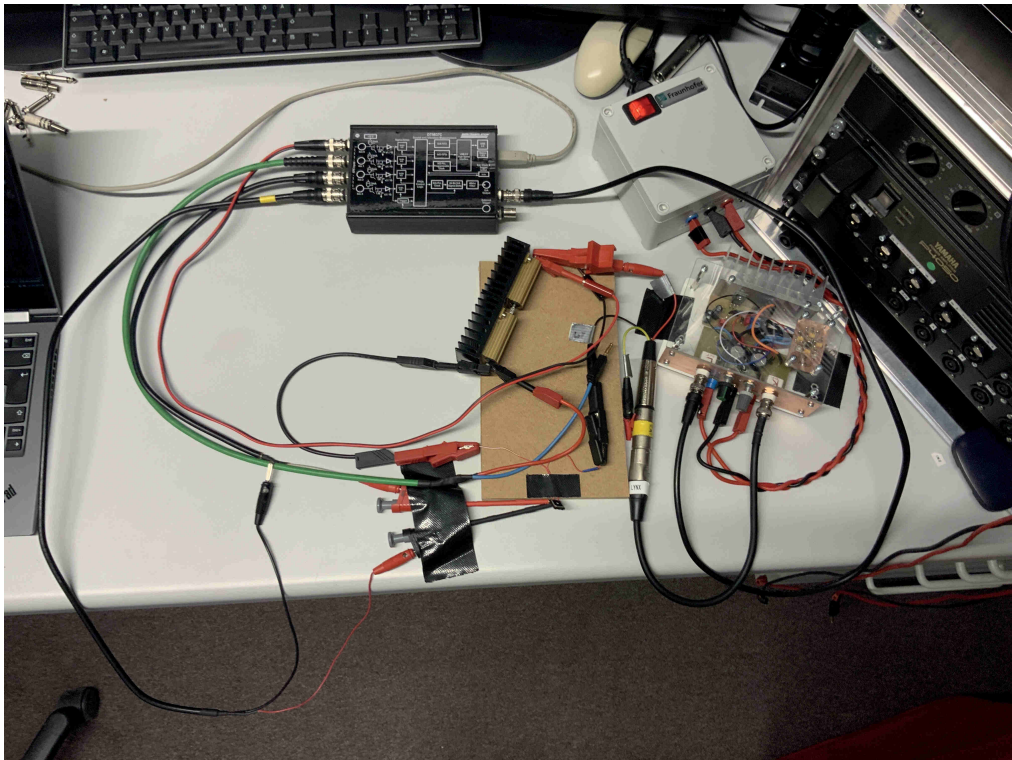


Figure 5.9: Weak crosstalk setup. Note green and black/red wire not twisted and separated current-carrying wires.

5.4.5 Crosstalk Error

The lower spectrum, 2s pink noise excitation was repeated three times. Once, with the standard setup (fig. 5.1) where care was taken to ensure minimal crosstalk with the given equipment, then with a strong crosstalk setup (fig. 5.8) and a setup with weaker crosstalk compared to the strong setup (fig. 5.9).

The temperatures measured during the different crosstalk-setups can be seen in fig. 5.10. The DC temperature is slightly different between runs which could be due to different lab temperatures or offset calibration drift. This makes the difference between the standard setup and the weak crosstalk setup hard to judge, but the Eddy temperature is seen to a bit higher with the higher crosstalk. In the strong crosstalk setup, the HF temperature sinks about 4.5 K and the Eddy temperature rises about 20 K. It can only be concluded that crosstalk has a significant influence on the HF method that however is hard to quantify. Ideally, the temperature calibration would be performed with the fixed final setup to exclude crosstalk as error source.

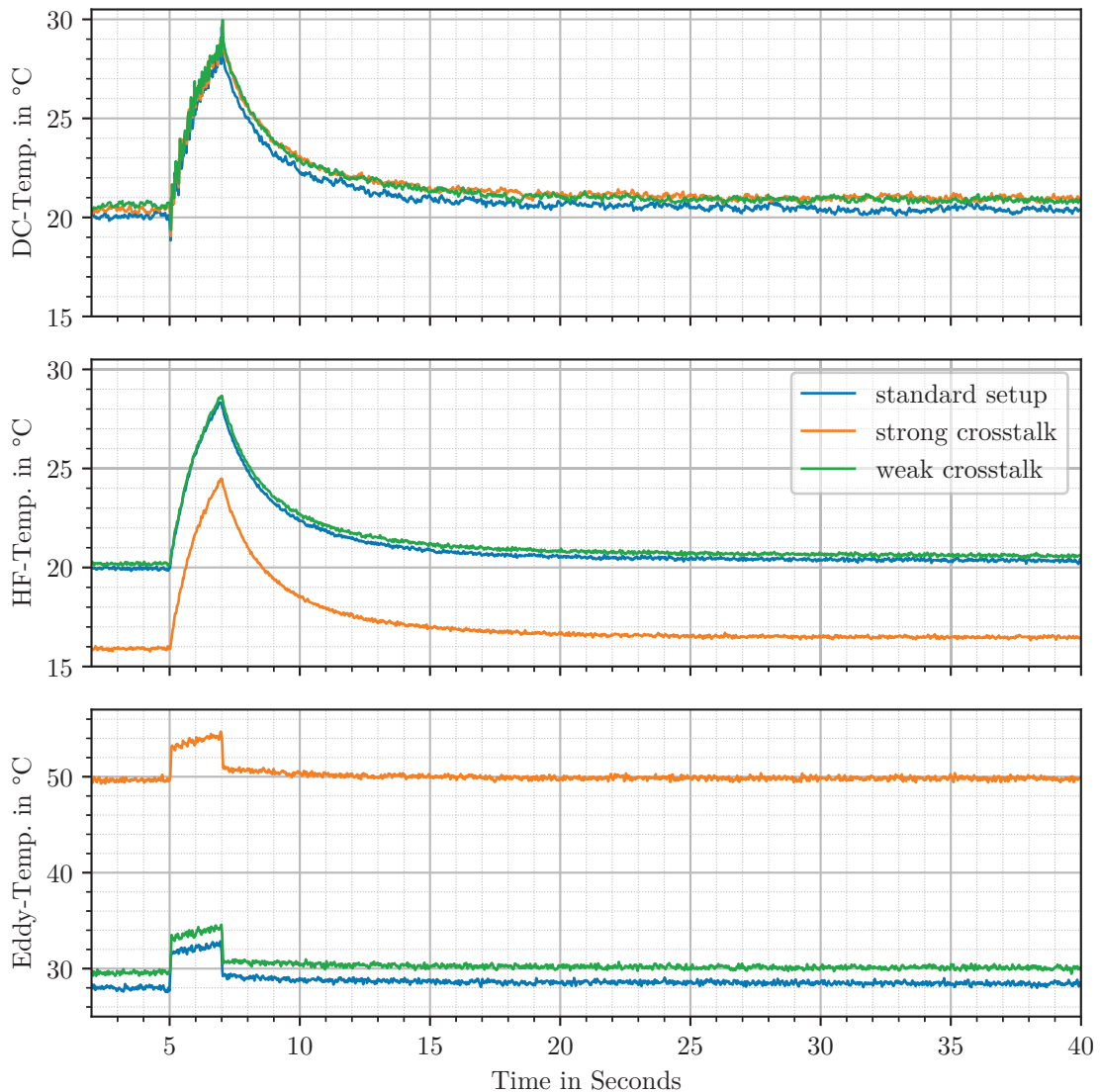


Figure 5.10: Temperature measurement with different crosstalk setups. The test signal is a pink noise, low spectrum, medium length. The measurements are manually time-aligned.

5.4.6 Influence of DC Offset

Figure 5.11 shows the lower spectrum, 2 s pink noise with and without the DC offset of (51 ± 1) mV required for the DC method. If the calibration with DC offset is used but the offset is not applied, the HF temperature is about 1 K too high and the Eddy temperature about 1 K too low. Once the correct calibration without DC-offset is applied, the agreement between both measurement runs is good and is easily attributable to other error sources. As expected, the HF method is sensitive to offsets in excursion.

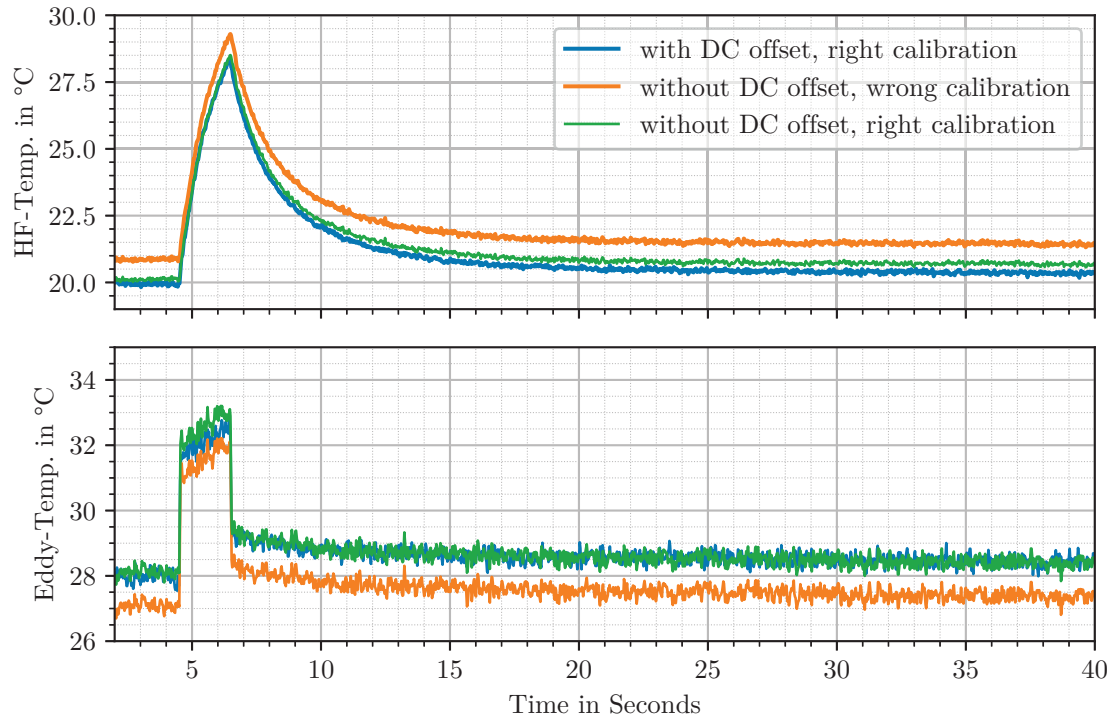


Figure 5.11: Comparison of temperature measurement with and without DC offset from the DC method. The test signals is a pink noise, low spectrum, medium length. The orange curve is recorded without DC offset but uses the calibration with DC offset, resulting a visible deviation. The measurements are manually time-aligned.

5.5 Discussion

The HF method was shown to agree with the established DC method to within ± 1 K, which is four times smaller than the DC method uncertainty. These minor errors are introduced by noise, an unexplained effect correlated to voice coil temperature and excursion offsets, which may be created by strong low frequency signals. Major errors can be introduced in the HF impedance through varying amounts of crosstalk between calibration and measurement.

As expected, the Eddy temperature changed slower and less than the voice coil temperature, supporting the hypothesis that the Eddy temperature is an indication of pole plate temperature. Applying high frequency signals heats the thin layer where the Eddy temperature is measured through induction heating. This creates an effect of multiple Kelvin that directly tracks the amount of applied high frequency power and increases with rising frequency. Unfortunately, the Eddy temperature was 8 K too high in all measurements - an error which could not be explained.

As expected, the DC method could be shown to be more sensitive to out-of-band error from low frequency audio signals than the HF method.

6 Conclusion

In the first section of the conclusion, all previous results are used to compare the DC and HF method to the requirements and judge their suitability for voice coil temperature measurement. In the second section, all previous findings are summarized. Finally, suggestions for future research are given.

6.1 Evaluation against Requirements

In section 3.1, requirements for voice coil temperature measurement were established. First, a temperature range of up to $-55\text{ }^{\circ}\text{C}$ to $350\text{ }^{\circ}\text{C}$ was shown to be needed. Both DC and HF method can fulfil this requirement, though a quadratic expansion for the DC resistance should be used with larger temperature ranges (section 3.2).

The required temperature tolerance was determined to be $\pm 7\text{ K}$ (section 3.1.2). The calibration offset error of the DC method was $\pm 4\text{ K}$ and the temperature during calibration was accurate to within $\pm 2.5\text{ K}$, resulting in a combined error of $\pm 6.5\text{ K}$. The HF temperature did not deviate more than 1 K from the DC temperature, so its combined error is $\pm 7.5\text{ K}$. However if a strong change in cable crosstalk occurs or a metal object is brought close to the speaker, significant errors in HF temperature may be induced. Assuming these factors are handled, both methods can provide the required accuracy.

The required bandwidth of 0.2 Hz to 26 Hz (section 3.1.3) can theoretically be reached by both methods when an appropriate lowpass is used. However, this lowpass must achieve a compromise between smoothing error and out-of-band error. In experiment 2, the DC method showed significantly more noise than the HF method when the same lowpass was used for both methods. Therefore, as expected in section 3.3.3, the HF method can deliver higher bandwidth at the same out-of-band error compared to the DC method.

When looking at economic, practical and other requirements, the DC method should have lower development cost as it is simpler than the HF method. The HF method requires a high frequency impedance measuring device (which can be implemented in hardware which means high sampling rates are not a necessary requirement), choosing an HF frequency that is free of temperature-dependent resonances and considering lots of error factors due to the radio-like behavior of high frequencies.

Both methods can be applied during audio playback with small impacts on sound quality: The DC method creates a DC offset in the position of the voice coil, which

may create stronger non-linearities during audio playback. The HF method causes intermodulation distortion. The HF method might also cause issues for animals or people with a hearing threshold above the HF method frequency.

Considering the calibration effort, the DC method requires lower effort for calibration. In the simplest case, the DC resistance is measured at a known temperature and a table value is used for the resistance thermal coefficient. However not all wires have the same thermal coefficient so an error of around $\pm 3\%$ (section 3.2) must be accepted. If higher accuracy calibration is required, the DC resistance can be measured at multiple known temperatures. Whether this calibration needs to be repeated for different speaker samples depends on the amount of variation in DC resistance and thermal coefficient between samples. A sample can theoretically change its DC resistance over time, e.g. due to strong heating, but this effect is likely small and may be compensable [21].

The simplest form of calibration for the HF method consists of measuring the HF impedance and DC resistance at a known temperature. Then, a constant $\text{Re}(Z_e)$ can be assumed and the DC resistance is given by $R_{DC} \approx \text{Re}(Z) - \text{Re}(Z_e)$. The relationship between DC resistance and temperature needs to be calibrated the same as for the DC method. In our specific case, assuming a constant real part of Z_e would incur an error of $\pm 1\text{ K}$ that would shrink with rising HF frequency. To remove this error, the relationship $\text{Re}(Z_e) \sim \text{Im}(Z_e)$ can be calibrated which requires measuring Z_e and R_{DC} at different, but unknown temperatures. If the temperature is known, the relationship $\text{Im}(Z_e) \sim T_e$ for the Eddy temperature can also be calibrated. How much the HF calibration changes between samples or over time is a topic left for future research.

A final comparison of the DC and HF method based on the results of this thesis is provided in table 6.1. Overall, the DC method can fulfil all requirements for voice coil temperature measurement and is simpler than the HF method. However the HF method provides lower noise, higher bandwidth, lower power and better integration with active excursion offset stabilization. Additionally, measurement of the Eddy temperature when no audio signal is playing can be used for better initialization of a thermal model.

Table 6.1: Qualitative comparison of DC and HF method.

| DC Method | HF Method |
|---|---|
| simple | complex |
| | patented [25] |
| higher out-of-band noise | lower out-of-band noise → higher bandwidth → lower power measurement signal |
| causes excursion offset | causes intermodulation distortion, may affect HF-sensitive animals and people |
| | affected by excursion changes slower than impedance lowpass |
| active excursion stabilization may not provide a steady DC signal | active excursion offset stabilization may improve accuracy |
| requires audio highpass to reduce out-of-band error | requires less aggressive audio highpass to filter excursion-dependence |
| | requires audio lowpass, e.g. band-limited digital audio |
| | surface temperature of pole plates measurable (strongly affected by induction heating) |
| measurement sensitive to voltage offsets | measurement sensitive to crosstalk or close conducting objects |
| | class D amplifiers where speaker is part of output filter will increase out-of-band error |
| | how much calibration is required at which frequency for which speaker type is unknown |
| | requires resonance-free ultrasonic frequency band |

6.2 Summary

The first chapter motivated why voice coil temperature measurement is an important tool during loudspeaker development and is needed during audio playback to unlock the last decibels of thermal headroom.

In the second chapter, different approaches to voice coil temperature measurement from the literature were reviewed. Resistance-based methods were judged to be most interesting because they are simple, effective and do not require any modification to the speaker. The HF method was chosen as the topic of this thesis as it promises higher bandwidth and lower noise than other resistance-based methods but little existing research.

In the theory chapter, the required temperature range for voice coil temperature measurement was determined to be -55°C to 350°C . The temperature above ambient should be measured with an accuracy of $\pm 5.5\%$ to make the reduction in sound level inaudible. The temperature bandwidth should be 0.2 Hz to 26 Hz, depending on voice coil size.

The relationship between DC resistance and temperature can be assumed to be linear within typical temperature ranges of 150 K. If a high temperature voice coil is used, a quadratic expansion should be considered.

Two inherent kinds of errors were shown to exist in impedance measurement: Out-of-band error is caused by signals other than the measurement frequency and their interaction with varying impedance in the measurement passband. The smoothing error is caused by the lowpass required to filter out-of-band signals. In all impedance measurement, there is a tradeoff between out-of-band error and smoothing error. The HF method was shown to provide a better tradeoff than the DC method.

The blocked HF impedance model suggested by Anazawa [27], where $Z = R_{DC} + Z_e$, was reviewed for dependencies on various factors. No influence on DC resistance other than the voice coil temperature could be found. The Skin effect was shown to not be significant in microspeakers but possibly a strong influence with thick voice coil wire. The strongest influence on Z_e are the induced magnetic fields, causing a dependence on frequency, excursion and Eddy temperature. Eddy temperature is the temperature of all parts where Eddy currents flow. Its influence on the speaker impedance was reported for the first time. A lumped model for the dependence of Z_e on frequency, excursion and Eddy temperature was presented.

In experiment 1, all previously derived dependencies could be measured on a sample microspeaker. A new way to measure the excursion dependence of Z_e was developed that can compensate for changes in DC resistance during the test. The lumped Z_e model fit the measurement data with regard to frequency and temperature but required an empirical parameter to fit the excursion dependence. The HF method was shown to have a strong dependence on voice coil excursion. While this can be filtered

out for audio frequencies with little error, slow excursion drift may cause strong deviations. What Anazawa claimed to be a correction for the excursion error is more likely a correction for Eddy temperature that works reasonably well at 19 kHz, but not at 34 kHz. The correct Eddy temperature correction was measured and fit with a linear regression.

The second experiment demonstrated that the HF method can provide the same temperature readings as the established DC method. Only minor deviations, correlated with voice coil temperature and movement, were apparent. As predicted, offsets in the voice coil excursion can have a strong effect on the HF method. The Eddy temperature had a constant offset of 8 K throughout the whole second experiment which could not be explained. The Eddy temperature was shown to be strongly affected by induction heating while high frequency signals are playing.

In the final chapter, it was concluded that the DC method is simpler than the HF method and good enough considering the requirements. However, the HF method does promise lower noise, higher bandwidth, lower power, better integration with active excursion offset stabilization and the Eddy temperature can be used for better initialization of a thermal model.

6.3 Outlook

The HF method suffers from high complexity. Future research might try to reduce this complexity by answering the following questions:

- How big is the influence of conducting material in proximity to the speaker?
- What are the characteristics of the HF method with different types of moving coil or electrodynamic speakers?
- How big are the deviations between samples in the calibration of the HF method?
- At which frequencies and for which loudspeaker types can $\text{Re}(Z_e)$ be expected to be constant with Eddy temperature, allowing calibration at only one known temperature?
- Can the relationship between $\text{Im}(Z)$ and the Eddy temperature be predicted without calibration at different temperatures?
- How can the HF method effectively be integrated into active loudspeaker management?

Hopefully, this thesis can provide a starting point to answer these questions in the future and enable better measurement of loudspeaker temperature. This will help deal with thermal issues and enable louder better sounding small speakers, so we can take the music we love anywhere.

Bibliography

- [1] Robert J. Zatorre. “Why Do We Love Music?” In: *Cerebrum: the Dana Forum on Brain Science* 2018 (Nov. 1, 2018). ISSN: 1524-6205. pmid: 30746026. URL: <https://www.ncbi.nlm.nih.gov/pmc/articles/PMC6353111/> (cit. on p. 6).
- [2] Wolfgang Klippel. “Green Speaker Design (Part 1: Optimal Use of System Resources)”. In: Audio Engineering Society Convention 146. Mar. 10, 2019. URL: <http://www.aes.org/e-lib/browse.cfm?elib=20271> (cit. on pp. 6, 9, 12).
- [3] Gyeong-Tae Lee, Jong-Bae Kim, and Dong-Hyun Jung. “Physical Requirements of New Acoustic Transducers to Replace Existing Moving-Coil Loudspeakers”. In: Audio Engineering Society Convention 137. Oct. 8, 2014. URL: <http://www.aes.org/e-lib/browse.cfm?elib=17484> (cit. on p. 7).
- [4] Mike Klasco. *The Impact of MEMS Speakers in Audio* | *audioXpress*. Feb. 4, 2020. URL: <https://audioxpress.com/article/the-impact-of-mems-speakers-in-audio> (visited on 11/17/2020) (cit. on p. 7).
- [5] Martin Colloms and Paul Darlington. *High Performance Loudspeakers*. 7th ed. John Wiley & Sons Ltd., 2018. ISBN: 978-1-118-41353-1 (cit. on p. 7).
- [6] John Borwick, ed. *Loudspeaker and Headphone Handbook*. 3rd ed. Routledge, 2001. DOI: 10.4324/9780080496177 (cit. on p. 7).
- [7] Mike Klasco and Steve Tatarunis. *Loudspeaker Failures and Protections (Part 1)* | *audioXpress*. Feb. 19, 2020. URL: <https://audioxpress.com/article/loudspeaker-failures-and-protections-part-1> (visited on 12/10/2020) (cit. on pp. 7, 8).
- [8] Phil Allison and Rod Elliott. *Speaker Failure Analysis*. URL: <https://sound-au.com/articles/speaker-failure.html> (visited on 12/10/2020) (cit. on p. 7).
- [9] Wolfgang Klippel. “Nonlinear Modeling of the Heat Transfer in Loudspeakers”. In: *Journal of the Audio Engineering Society* 52.1/2 (2004), pp. 3–25. URL: <http://www.aes.org/e-lib/browse.cfm?elib=12980> (cit. on pp. 7, 9, 12, 18).
- [10] Anders Elowsson and Anders Friberg. “Long-Term Average Spectrum in Popular Music and Its Relation to the Level of the Percussion”. In: *Audio Engineering Society Convention 142*. May 11, 2017. URL: <http://www.aes.org/e-lib/browse.cfm?elib=18638> (cit. on p. 8).
- [11] Clifford A. Henricksen. “Heat Transfer Mechanisms in Loudspeakers; Analysis, Measurement and Design”. In: *Audio Engineering Society Convention 80*. Mar. 1986. URL: <http://www.aes.org/e-lib/browse.cfm?elib=5087> (cit. on pp. 9, 11, 42).

- [12] Carlo Zuccatti. “Thermal Parameters and Power Ratings of Loudspeakers”. In: *Journal of the Audio Engineering Society* 38.1/2 (1990), pp. 34–39. URL: <http://www.aes.org/e-lib/browse.cfm?elib=6052> (cit. on pp. 9, 16).
- [13] Peter John Chapman. “Thermal Simulation of Loudspeakers”. In: *Audio Engineering Society Convention 104*. May 1998. URL: <http://www.aes.org/e-lib/browse.cfm?elib=8513> (cit. on pp. 9, 11, 15, 16).
- [14] Fabio Blasizzo. “A New Thermal Model for Loudspeakers”. In: *Journal of the Audio Engineering Society* 52.1/2 (2004), pp. 43–56. URL: <http://www.aes.org/e-lib/browse.cfm?elib=12982> (cit. on pp. 9, 18).
- [15] Johan Toverland. “Thermal Modelling of Voice Coils in Microspeakers”. Master of Science Thesis in Electrical Engineering. Linköping University, May 2016. 64 pp. URL: <https://liu.diva-portal.org/smash/get/diva2:954210/FULLTEXT01.pdf> (cit. on p. 9).
- [16] Mike Klasco and Steve Tatarunis. *Microspeakers’ Anatomy - How to Design Audio Systems with Very Small Drivers* | *audioXpress*. July 16, 2019. URL: <https://audioxpress.com/article/microspeakers-anatomy-how-to-design-audio-systems-with-very-small-drivers> (visited on 12/10/2020) (cit. on p. 9).
- [17] Hugo Fastl and Eberhard Zwicker. *Psychoacoustics*. Berlin, Heidelberg: Springer Berlin Heidelberg, 2007. DOI: 10.1007/978-3-540-68888-4 (cit. on pp. 9, 16).
- [18] *VCi-1 Voicecoil Temperature Sensor (Version 3.5) – Dioguardo Engineering*. URL: <http://web.archive.org/web/20201116205339/https://dioguardoengineering.com/products/vci-1-voicecoil-temperature-sensor-revision-2-5?variant=11346764486> (cit. on p. 11).
- [19] Ronny Andersson. “Loudspeaker Voice-Coil Temperature Estimation”. Master’s Thesis - Electrical Engineering. Luleå University of Technology, Mar. 8, 2008. 25 pp. URL: <https://www.diva-portal.org/smash/get/diva2:1015303/FULLTEXT01.pdf> (cit. on pp. 11, 35).
- [20] Moo-Yeon Lee and Hyung-Jin Kim. “Heat Transfer Characteristics of a Speaker Using Nano-Sized Ferrofluid”. In: *Entropy* 16.11 (Nov. 10, 2014), pp. 5891–5900. ISSN: 1099-4300. DOI: 10.3390/e16115891 (cit. on p. 11).
- [21] John Howard Dellinger. “The Temperature Coefficient of Resistance of Copper”. In: *Bulletin of the Bureau of Standards* (Nov. 29, 1910), p. 31. URL: https://nvlpubs.nist.gov/nistpubs/bulletin/07/nbsbulletinv7n1p71_A2b.pdf (cit. on pp. 12, 20, 77).
- [22] Paul Pickering. *Make Your Audio System Sound Better with Smart Amp Technology* | *Electronic Design*. 2017. URL: <https://www.electronicdesign.com/technologies/analog/article/21805959/make-your-audio-system-sound-better-with-smart-amp-technology> (visited on 12/15/2020) (cit. on p. 12).

- [23] Finn Agerkvist, Knud Thorborg, and Carsten Tinggaard. “A Study of the Creep Effect in Loudspeaker Suspension”. In: Audio Engineering Society Convention 125. Oct. 2008. URL: <http://www.aes.org/e-lib/browse.cfm?elib=14713> (cit. on p. 12).
- [24] Gottfried Behler, U. Spätling, and T. Arimont. “Measuring the Loudspeaker’s Impedance During Operation for the Evaluation of the Voice Coil Temperature”. In: *Audio Engineering Society Convention 98*. Feb. 1995. URL: <http://www.aes.org/e-lib/browse.cfm?elib=7765> (cit. on p. 13).
- [25] Temujin Gautama. “Determining the Temperature of a Loudspeaker Voice Coil”. European pat. 2879401B1. NXP BV. Aug. 7, 2019. URL: <https://patents.google.com/patent/EP2879401B1/en?q=2015%2f0146875> (visited on 07/15/2020) (cit. on pp. 13, 25, 57, 78).
- [26] Isao G. Anazawa. “High Frequency—Ultra Audio Band Mode Voice Coil Temperature Measurement”. In: Audio Engineering Society Convention 142. May 11, 2017. URL: <http://www.aes.org/e-lib/browse.cfm?elib=18695> (cit. on pp. 13, 25, 58).
- [27] Isao Anazawa. “Voice Coil Temperature—Non Linearity Compensations for Ultra Audio Band Impedance Probing”. In: Audio Engineering Society Convention 143. Oct. 8, 2017. URL: <http://www.aes.org/e-lib/browse.cfm?elib=19235> (cit. on pp. 13, 57–60, 79).
- [28] Mark Dodd, Wolfgang Klippel, and Jack Oclew-Brown. “Voice Coil Impedance as a Function of Frequency and Displacement”. In: Audio Engineering Society Convention 117. Oct. 1, 2004. URL: <http://www.aes.org/e-lib/browse.cfm?elib=12835> (cit. on pp. 14, 26, 27).
- [29] *Military and Aerospace Semiconductors | Maxim Integrated*. URL: <http://web.archive.org/web/20200907062531/https://www.maximintegrated.com/en/markets/military-aerospace.html> (cit. on p. 15).
- [30] *High Temperature Epoxy Adhesive for Coils and Motors*. URL: <https://www.intertronics.co.uk/2006/08/rocking-your-world/> (visited on 11/10/2020) (cit. on p. 15).
- [31] Richard A. Matula. “Electrical Resistivity of Copper, Gold, Palladium, and Silver”. In: *Journal of Physical and Chemical Reference Data* 8.4 (1979), p. 152. URL: <https://srdata.nist.gov/JPCRD/jpcrd155.pdf> (cit. on pp. 18, 20, 56).
- [32] Yeram Sarkis Touloukian et al. *Thermal Expansion - Metallic Elements and Alloys*. Vol. 12. 13 vols. Thermophysical Properties of Matter - The TRPC Data Series. IFI/Plenum Data Company New York - Washington, 1975. ISBN: 0-306-67020-8. URL: <https://apps.dtic.mil/dtic/tr/fulltext/u2/a129115.pdf> (cit. on p. 18).
- [33] *Electrical Resistance and Conductance*. In: *Wikipedia*. Nov. 29, 2020. URL: https://en.wikipedia.org/w/index.php?title=Electrical_resistance_and_conductance&oldid=991357067#Dependence_of_resistance_on_other_conditions (cit. on p. 25).

- [34] Thomas C. Wilson. “Photoconductivity of Metal Films”. In: *Physical Review* 55.3 (Feb. 1, 1939), pp. 316–317. DOI: 10.1103/PhysRev.55.316.2 (cit. on p. 25).
- [35] Paolo Ravazzani et al. “Frequency-Related Effects in the Optimization of Coils for Magnetic Stimulation of the Nervous System”. In: *IEEE Transactions on Biomedical Engineering* 49 (June 1, 2002), pp. 463–71. DOI: 10.1109/10.995685 (cit. on p. 26).
- [36] Atin Audio. *SPEAKER VOICE COIL WIRE*. URL: <http://www.atin-audio.com/products/voicecoilmaterial/speaker-voice-coil-wire.html> (visited on 11/24/2020) (cit. on p. 26).
- [37] *Custom Voice Coils | Precision Econowind LLC*. URL: <https://precisioneconowind.com/custom-voice-coils/> (visited on 12/22/2020) (cit. on p. 26).
- [38] R. L. Sanford. “Temperature Coefficient of Magnetic Permeability within the Working Range”. In: *Bulletin of the Bureau of Standards* 12 (Dec. 2, 1914), p. 10. URL: https://nvlpubs.nist.gov/nistpubs/bulletin/12/nbsbulletin12n1p1_a2b.pdf (cit. on pp. 26, 56, 64).
- [39] Knud Thorborg and Claus Futtrup. “Electrodynamic Transducer Model Incorporating Semi-Inductance and Means for Shorting AC Magnetization”. In: *Journal of the Audio Engineering Society* 59.9 (Oct. 10, 2011), pp. 612–627. URL: <http://www.aes.org/e-lib/browse.cfm?elib=15978> (cit. on pp. 27, 28, 31).
- [40] Knud Thorborg and Andrew D. Unruh. “Electrical Equivalent Circuit Model for Dynamic Moving-Coil Transducers Incorporating a Semi-Inductor”. In: *Journal of the Audio Engineering Society* 56.9 (Oct. 10, 2008), pp. 696–709. URL: <http://www.aes.org/e-lib/browse.cfm?elib=14633> (cit. on pp. 27, 30).
- [41] David C. Hamill. “Lumped Equivalent Circuits of Magnetic Components: The Gyrator-Capacitor Approach”. In: *IEEE Transactions on Power Electronics* 8.2 (Apr. 1993), pp. 97–103. ISSN: 1941-0107. DOI: 10.1109/63.223957 (cit. on p. 28).
- [42] John Vanderkooy. “A Model of Loudspeaker Driver Impedance Incorporating Eddy Currents in the Pole Structure”. In: *Journal of the Audio Engineering Society* 37.3 (Mar. 1, 1989), pp. 119–128. URL: <http://www.aes.org/e-lib/browse.cfm?elib=6100> (cit. on pp. 29, 30, 56).
- [43] Jerome G. Hust. *Electrical Resistivity of Electrolytic Iron, SRM 797 and Austenitic Stainless Steel, SRM 798, from 5 to 280 K*. Feb. 1974. URL: <https://nvlpubs.nist.gov/nistpubs/Legacy/SP/nbsspecialpublication260-47.pdf> (visited on 12/23/2020) (cit. on p. 30).
- [44] *Permeability (Electromagnetism)*. In: *Wikipedia*. Dec. 11, 2020. URL: [https://en.wikipedia.org/w/index.php?title=Permeability_\(electromagnetism\)&oldid=993542829](https://en.wikipedia.org/w/index.php?title=Permeability_(electromagnetism)&oldid=993542829) (cit. on p. 30).

- [45] M.E. Eaton. “Adding Flux Paths to SPICE’s Analytical Capability Improves the Ease and Accuracy of Simulating Power Circuits”. In: *APEC ’98 Thirteenth Annual Applied Power Electronics Conference and Exposition*. Vol. 1. Anaheim, CA, USA: IEEE, 1998, pp. 386–392. DOI: 10.1109/APEC.1998.647719 (cit. on p. 31).
- [46] Angelo Farina. “Simultaneous Measurement of Impulse Response and Distortion with a Swept-Sine Technique”. In: Audio Engineering Society Convention 108. Feb. 1, 2000. URL: <https://www.aes.org/e-lib/browse.cfm?elib=10211> (cit. on pp. 33, 37, 61).
- [47] *DIN EN 60268-5 Sound System Equipment - Part 5: Loudspeakers (IEC 60268-5:2003 + A1:2007); German Version EN 60268-5:2003 + A1:2009*. DOI: 10.31030/1568928 (cit. on p. 34).
- [48] *Datasheet PUI AS01508AO-3-R*. Sept. 2016. URL: <https://www.puiaudio.com/media/SpecSheet/AS01508AO-3-R.PDF> (visited on 11/16/2020) (cit. on p. 34).
- [49] *Keysight Impedance Measurement Handbook*. 6th Edition. Keysight Application Notes. Keysight Technologies. 153 pp. URL: <https://www.keysight.com/zz/en/assets/7018-06840/application-notes/5950-3000.pdf> (cit. on p. 35).
- [50] *DT 9837 USB-Messbox - Mobile Schall- Und Schwingungsmessung - Data Translation*. URL: <https://www.datatranslation.de/de/schwingung/schwingungsmessung-usb/dt9837/usb-messgeraete-iepe-sensoren,1063.html> (visited on 11/25/2020) (cit. on pp. 37, 50).
- [51] *Mccdaq/Uldaq: MCC Universal Library for Linux*. URL: <https://github.com/mccdaq/uldaq> (cit. on p. 37).
- [52] *6.5 Digit Multimeter | Desktop DMM | Fluke 8845A & 8846A*. URL: https://eu.flukecal.com/products/data-acquisition-and-test-equipment/bench-multimeters/8845a8846a-65-digit-precision-multime?quicktabs_product_details=4 (visited on 12/04/2020) (cit. on pp. 37, 47).
- [53] *Dynamic Climate Chamber with Humidity Control, MKF 60-Liter Capacity*. URL: <https://www.binder-world.com/en/products/dynamic-climate-chambers/series-mkf/mkf-56> (visited on 12/01/2020) (cit. on pp. 38, 45).
- [54] *Julia*. Version 1.5.0. The Julia Programming Language. URL: <https://github.com/JuliaLang/julia> (cit. on p. 41).
- [55] *PyPlot*. Version 2.9.0. JuliaPy. URL: <https://github.com/JuliaPy/PyPlot.jl> (cit. on p. 41).
- [56] *GLM*. Version 1.3.11. Julia Statistics. URL: <https://github.com/JuliaStats/GLM.jl> (cit. on p. 41).
- [57] *LsqFit*. Version 0.11.0. JuliaNLSolvers. URL: <https://github.com/JuliaNLSolvers/LsqFit.jl> (cit. on p. 41).
- [58] *FFTW*. Version 1.2.4. Julia Math. URL: <https://github.com/JuliaMath/FFTW.jl> (cit. on p. 41).

- [59] *DSP*. Julia DSP. URL: <https://github.com/JuliaDSP/DSP.jl> (cit. on p. 41).
- [60] Robert Feldt. *BlackBoxOptim*. Version 0.5.0. URL: <https://github.com/robertfeldt/BlackBoxOptim.jl> (cit. on pp. 41, 44).
- [61] Fredrik Bagge Carlson. *ControlSystemIdentification*. Version 1.0.0. URL: <https://github.com/baggepinnen/ControlSystemIdentification.jl> (cit. on p. 41).
- [62] *JupyterLab*. Version 2.2.4. JupyterLab. URL: <https://github.com/jupyterlab/jupyterlab> (cit. on p. 41).
- [63] Edward B. Rosa. “The Self and Mutual-Inductance of Linear Conductors”. In: *Bulletin of the Bureau of Standards* 4 (Sept. 15, 1907). URL: <http://archive.org/details/selfmu430134419088080unse> (cit. on p. 49).
- [64] *The Complete Guide to Electrical Insulation Testing*. 2006. URL: <https://www.instrumart.com/assets/Megger-Guide-to-Insulation-Testing.pdf> (visited on 06/12/2020) (cit. on p. 49).
- [65] John David Jackson. *Classical Electrodynamics*. 3rd ed. New York: Wiley, 1999. 808 pp. ISBN: 978-0-471-30932-1. URL: http://www.fisica.unlp.edu.ar/materias/electrolicfismed/electromagnetismo-material-adicional/Jackson%20-%20Classical%20Electrodynamics%203rd%20edition.pdf/at_download/file (cit. on p. 50).
- [66] Wolfgang Klippel. “Adaptive Stabilization of Electrodynamic Transducers”. In: *Journal of the Audio Engineering Society* 63.3 (Mar. 16, 2015), pp. 154–160. URL: <https://www.aes.org/e-lib/browse.cfm?elib=17574> (cit. on p. 60).
- [67] Guy Williams. “Eddy-Current Technique for Sub-Surface Temperature Measurement in a Cast Steel Strand”. In: *Review of Progress in Quantitative Nondestructive Evaluation* (1991). Ed. by Donald O. Thompson and Dale E. Chimenti, pp. 2193–2200. DOI: 10.1007/978-1-4615-3742-7_139 (cit. on p. 60).
- [68] *IC A2030H Datasheet*. URL: <https://www.web-bcs.com/oem/rf/A2030H.php?lan=en&c1=1> (visited on 12/14/2020) (cit. on p. 62).
- [69] Wolfgang Klippel. “Prediction of Speaker Performance at High Amplitudes”. In: Audio Engineering Society Convention 111. Nov. 1, 2001. URL: <https://www.aes.org/e-lib/browse.cfm?elib=9834> (cit. on p. 71).

List of Figures

| | | |
|------|---|----|
| 1.1 | Schematic cross-section of a typical moving coil microspeaker. | 7 |
| 1.2 | Thermal failure of a speaker with 1-inch voice coil. | 8 |
| 3.1 | Magnitude response of the Zucatti thermal model vs. frequency. | 17 |
| 3.2 | Linear fit of copper resistivity vs. temperature. | 19 |
| 3.3 | Relative residuals of linear fit of copper resistivity vs. a smaller temperature range. | 19 |
| 3.4 | Relative resistance increase due to Skin effect vs. frequency. | 27 |
| 3.5 | Visualization of B-Field induced by current through the voice coil. | 28 |
| 3.6 | Equivalent circuit for Z_e in the Gyrator-Capacitor Approach. | 29 |
| 3.7 | Equivalent circuit for Z_e , transformed from the magnetic to the electrical domain. | 29 |
| 4.1 | The pulse signal. | 33 |
| 4.2 | PUI speaker used in this thesis. | 34 |
| 4.3 | Measured impedance of shunt resistor with fit. | 36 |
| 4.4 | Speaker setup in the climate chamber. | 38 |
| 4.5 | Measurement setup on top of the climate chamber. | 39 |
| 4.6 | Monitored impedance during experiment 1. | 40 |
| 4.7 | Evolution of HF impedance Z and Z_e on the complex plane while playing the pulse test signal. | 42 |
| 4.8 | DC resistance during pulse-measurement at 20 °C with power and RC model. | 43 |
| 4.9 | Residual noise. | 46 |
| 4.10 | PDFs for residual noise with fit normal distributions. | 46 |
| 4.11 | Impedance magnitude as measured by the sweep in 5 K steps. | 52 |
| 4.12 | Impedance phase as measured by the sweep in 5 K steps. | 52 |
| 4.13 | DC resistance vs. temperature. | 53 |
| 4.14 | Imaginary part of Z_e at zero excursion vs. temperature. | 54 |
| 4.15 | Real part of Z_e vs. frequency at different temperatures with Z_e model. | 55 |
| 4.16 | Imaginary part of Z_e vs. frequency at different temperatures with Z_e model. | 55 |
| 4.17 | Z_e at 34 kHz on the complex plane at different excursions and temperatures. | 57 |
| 4.18 | Z_e at 34 kHz on the complex plane at zero excursion with Eddy temperature correction. | 59 |
| 4.19 | Z_e at 19 kHz on the complex plane with Anazawa's excursion assumption. | 59 |
| 5.1 | Experiment 2 setup. | 62 |

| | | |
|------|--|----|
| 5.2 | Temperature measurement with pink noise, high spectrum, long length. | 65 |
| 5.3 | Temperature measurement with logarithmic sweep. | 66 |
| 5.4 | Temperature measurement with pink noise, low spectrum, medium length. | 67 |
| 5.5 | Temperature measurement with pink noise, high spectrum, medium length. | 68 |
| 5.6 | Temperature measurement with pink noise, high spectrum, short length. | 69 |
| 5.7 | Spectra of DC and HF temperature vs. frequency. Test run without thermal excitation. | 71 |
| 5.8 | Strong crosstalk setup. | 72 |
| 5.9 | Weak crosstalk setup. | 72 |
| 5.10 | Temperature measurement with different crosstalk setups. | 73 |
| 5.11 | Comparison of temperature measurement with and without DC offset. | 74 |

List of Tables

| | | |
|-----|--|----|
| 4.1 | Standard deviations of normal distributions fit to the residual noise of the monitored impedances. | 45 |
| 4.2 | Calibration offset error. | 47 |
| 4.3 | Calibration gain error. | 48 |
| 4.4 | Calibration gain error propagation for DC. | 48 |
| 4.5 | Calibration gain error propagation for HF. | 49 |
| 4.6 | Z_e model fit parameters. | 56 |
| 5.1 | Thermal excitation signals. | 63 |
| 6.1 | Qualitative comparison of DC and HF method. | 78 |